

AN ANALYSIS OF THE HEAT AND MASS TRANSPORT DURING THE  
FREEZING OF BIOMATERIALS

by

Michael Gregory O'Callaghan

B.S., Rensselaer Polytechnic Institute  
(1973)

S.M.M.E., Massachusetts Institute of Technology  
(1975)

SUBMITTED IN PARTIAL FULFILLMENT  
OF THE REQUIREMENTS FOR THE  
DEGREE OF

DOCTOR OF PHILOSOPHY

at the

MASSACHUSETTS INSTITUTE OF TECHNOLOGY

October, 1978

*Michael Gregory O'Callaghan*

Signature of Author.....  
Department of Mechanical Engineering, October 6, 1978

Certified by.....  
Thesis Supervisor

Accepted by.....  
Chairman, Department Committee on Graduate Students  
Archives

MASSACHUSETTS INSTITUTE  
OF TECHNOLOGY

MAR 21 1979

LIBRARIES

AN ANALYSIS OF THE HEAT AND MASS TRANSPORT DURING THE  
FREEZING OF BIOMATERIALS

by

Michael Gregory O'Callaghan

Submitted to the Department of Mechanical Engineering on  
October 6, 1978 in partial fulfillment of the requirements  
for the Degree of Doctor of Philosophy.

ABSTRACT

A model describing the heat transfer, solute redistribution and kinetics of cellular water transport during the freezing of tissues has been developed. The temperature and concentration profiles and the interface motion were determined for the planar freezing of a sodium chloride-water solution, which represents a thermal approximation to the freezing of tissue. Application of the Mullins-Sekerka stability criterion indicated that the planar interface becomes unstable very soon after freezing begins. The interface will experience a transition to the dendritic freezing geometry.

A simple two-zone model of the steady dendritic solidification of saline is proposed. Families of temperature, concentration, and dendrite shape profiles were determined for each of the two zones using numerical methods. The appropriate geometric and thermodynamic optimization criteria were applied to find the particular profiles in each region that are compatible and satisfy the overall boundary conditions. The resulting temperature and concentration profiles were used in the Levin cellular dehydration model to determine the kinetics of water transport.

The results indicate that the heat flux required to produce a given freezing rate increases with free-field temperature and concentration. Substantial intracellular supercooling is predicted in unprotected organs for any practical freezing condition. The supercooling decreases markedly with saline concentration, indicating that high concentrations of cryoprotective agent are needed for tissue survival. A method of designing optimum thermal protocols is presented based on critical values of the maximum difference in the activity of water between the intracellular and the extracellular medium.

Thesis Supervisor: Ernest G. Cravalho

Title: Matsushita Professor of Mechanical Engineering  
in Medicine, Associate Director for Medical  
Engineering and Medical Physics, Harvard-MIT  
Division of Health Sciences and Technology

Acknowledgements

I would like to thank the members of my thesis committee Profs. Cravalho and Mikić and Drs. Bowman and Huggins. I would especially like to express my thanks to Ernie for all of his support through the years and to Bora for getting me a job.

The actual preparation of this thesis was through the capable typing of Mary Toscano and the drafting of Virginia McCauley.

I would also like to thank my colleagues from around Building 3, including Mark Snyder, Bob Nisonger (in memory), Ted Fisher, Bill Murray, Bill Westcott, Tiny and many others. Without your support, I would have finished much sooner.

Et finalement, à ma meilleure amie Kathy, que notre amour s'accroît chaque jour, et que nos vies soient assez enrichies et pleines qu'elles sont ces jours.

TABLE OF CONTENTS

	<u>Page</u>
ABSTRACT.....	2
ACKNOWLEDGMENTS.....	3
TABLE OF CONTENTS.....	4
LIST OF FIGURES.....	8
NOMENCLATURE.....	11
CHAPTER I Introduction.....	17
I.A Water-Transport Kinetics.....	21
I.B Present Considerations.....	22
CHAPTER II Fundamentals of Solidification.....	27
II.A Introduction.....	27
II.B Two-Phase Equilibrium.....	27
II.C Kinetics of Crystal Growth.....	32
II.D Redistribution of Solute During Freezing....	35
II.D.1 Constitutional Supercooling and Interface Stability.....	36
II.D.2 Higher Interface Structures.....	40
CHAPTER III Stability of the Planar Freeze Front in the Binary System NaCl-H <sub>2</sub> O.....	44
III.A Introduction.....	44

TABLE OF CONTENTS (CONTINUED )

	<u>Page</u>
III.B Transport Equations and Boundary Conditions.....	46
III.B.1 Heat Transfer Equations.....	46
III.B.2 Mass Transfer Equation.....	47
III.B.3 Boundary Conditions.....	50
III.B.4 Initial Conditions.....	55
III.C Method of Solution.....	58
III.C.1 Temperature Profiles.....	58
III.C.2 Heat Balance Integral.....	59
III.C.3 Mass Transfer Solution.....	64
III.C.4 Initial Conditions for the Integral Method.....	68
III.D Results and Discussion.....	69
III.E Stability of the Planar Interface.....	78
CHAPTER IV Heat and Mass Transport During Dendritic Solidification.....	86
IV.A Introduction.....	86
IV.A.1 Formation of Dendrites.....	86
IV.A.2 Problem Statement.....	87
IV.A.3 Optimization Condition.....	92
IV.A.4 Previous Research.....	94
IV.A.5 Two-zone Freezing Model.....	95

TABLE OF CONTENTS (CONTINUED)

	<u>Page</u>
IV.B The Equilibrium Zone.....	97
IV.B.1 Transport Equations.....	99
IV.B.1a Energy Transport.....	99
IV.B.1b Mass Transport.....	103
IV.B.2 Non-Dimensional Equations.....	106
IV.B.3 Boundary Conditions.....	108
IV.B.4 Equilibrium Region Results.....	111
IV.C Heat and Mass Transport Near the Dendrite Tips..	117
IV.C.1 Introduction.....	117
IV.C.2 Spheroidal Coordinate System.....	117
IV.C.3 Transport Equation.....	123
IV.C.4 Boundary Conditions.....	127
IV.C.5 Results.....	130
IV.D Optimization Condition.....	140
IV.E Spheroidal-Equilibrium Matching Procedure.....	150
IV.E.1 Geometric Compatibility.....	152
IV.E.2 Tip Stability.....	153
IV.E.3 Thermal Matching Conditions.....	153
IV.E.4 Method of Solution.....	157
IV.F Results.....	160
CHAPTER V Kinetics of Cellular Dehydration.....	181
V.A Transport Equation.....	181

TABLE OF CONTENTS (CONTINUED)

	<u>Page</u>
V.B Results.....	186
Chapter VI Summary and Suggestions for Further Research.....	198
Appendix I Numerical Methods.....	201
Appendix II Dendrite Spacing.....	205
References.....	209
Biographical Sketch.....	213

LIST OF FIGURES

	<u>Page</u>
I-1 Survival as a Function of Cooling Velocity for Various Cell Types.....	19
I-2 Idealized Biological Tissue.....	24
II-1 Equilibrium Diagram for the Fictitious Alloy X-Y.....	29
II-2 Equilibrium Diagram for NaCl-H <sub>2</sub> O.....	31
II-3 Schematic Representation of Constitutional Supercooling.....	37
II-4 Transition from Planar to Dendritic Interface Morphology.....	41
II-5 Schematic Representation of Steady Dendritic Freezing.....	42
III-1 Planar Freezing Geometry.....	45
III-2 Energy Balance at the Moving Interface.....	53
III-3 Typical Temperature Profiles and their Variation with C <sub>1</sub> and C <sub>2</sub> .....	61
III-4 Solid Phase Curvature Parameter.....	71
III-5 Interface Temperature Versus Time.....	72
III-6 Liquid Phase Curvature Parameter.....	76
III-7 Interface Position Versus Time.....	77
III-8 Typical Temperature and Concentration Profiles When $\sigma = 0.5$ , $H = - 3000 \text{ watts/m}^2$ .....	79
III-9 Mullins-Sekerka Stability Function Versus Interface Position.....	84
IV-1 Diagram of the Normal Vector to the Dendrite Surface.....	90



LIST OF FIGURES (CONTINUED)

	<u>Page</u>
IV-2 Summary of Exact Differential Equations and Boundary Conditions for Dendritic Solidification.....	93
IV-3 Approximate Isotherms During Dendritic Solidification.....	96
IV-4 Dendritic Freezing Geometry.....	100
IV-5 Control Volume for Overall Mass Conservation....	109
IV-6 Equilibrium Region Temperature Profiles.....	112
IV-7 Equilibrium Region Temperature Gradient Profiles.....	113
IV-8 Equilibrium Region Dendrite Shape Profiles.....	114
IV-9 Oblate and Prolate Spheroidal Coordinate Systems.....	119
IV-10 Spheroidal Coordinate Region Concentration Profiles for Various Peclet Numbers.....	131
IV-11 Spheroidal Coordinate Region Temperature Profiles for Various Peclet Numbers.....	135
IV-12 Relative Concentration Profiles for Constant Dendrite Width.....	141
IV-13 Relative Temperature Profiles for Constant Dendrite Width.....	144
IV-14 Dendrite Tip Region Isotherms.....	155
IV-15 Block Diagram of Overall Solution Scheme.....	158
IV-16 Relative Tip Concentration Versus Free-Field Superheat.....	161
IV-17 Dendrite Tip Temperature Versus Free-Field Superheat.....	162

LIST OF FIGURES (CONTINUED)

	<u>Page</u>
IV-18 Basal Temperature Gradient Versus Free-Field Superheat.....	163
IV-19 Relative Dendrite Length Versus Free-Field Superheat.....	164
IV-20 Overall Dendrite Shape Profiles for Several Free-Field Conditions.....	168
IV-21 Concentration Profiles Along Interdendritic Mid-Line.....	173
IV-22 Temperature Profiles Along Interdendritic Mid-Line.....	177
V-1 Loci of Intracellular Thermodynamic States $C_{\infty} = 145 \text{ moles/m}^3$ , $T_{\infty} = 273.2\text{K}$ .....	187
V-2 Water Volume Flux Versus Temperature $C_{\infty} = 145 \text{ moles/m}^3$ , $T_{\infty} = 273.2\text{K}$ .....	189
V-3 Loci of Intracellular Thermodynamic States $C_{\infty} = 1000 \text{ moles/m}^3$ , $T_{\infty} = 273.2\text{K}$ .....	190
V-4 Maximum Difference in the Activity of Water Versus Ratio of Water Permeability to (Interface Speed) <sup>2</sup> .....	192
AII-1 Experimental Results for Dendrite Spacing Versus KCl Concentration.....	207

NOMENCLATURE

a	=	characteristic dimension of oblate and prolate spheroids
a'	=	coefficient in equation (III-13) = 273.2 K
a''	=	coefficient in equation (III-66) = $2.679 \times 10^5$ moles/m <sup>3</sup>
a <sub>1,2</sub>	=	coefficient in the assumed temperature profiles (Chapter 3)
a <sub>w</sub>	=	activity of water
A	=	general cross-sectional area
A <sub>C</sub>	=	surface area of the cell
b <sub>1</sub>	=	major axis of spheroid (Chapter 4); linear coefficient in assumed temperature distribution (Chapter 3)
b'	=	coefficient in equation (III-13) = $3.371 \times 10^{-3}$ K <sup>-3</sup> /mole
b''	=	coefficient in equation (III-66) = $-3.634 \times 10^3$ mole/m <sup>3</sup> -K
B	=	cooling rate
c <sub>1</sub>	=	minor axis of spheroid
c'	=	coefficient in equation (III-13) = $2.854 \times 10^{-8}$ K-m <sup>6</sup> /mole <sup>2</sup>
c''	=	coefficient in equation (III-66) = $.1698$ moles/m <sup>3</sup> -K <sup>2</sup>
C <sub>L</sub>	=	liquid composition (Chapter 2)
C <sub>0</sub>	=	initial concentration
C <sub>S</sub>	=	concentration of solute
C	=	specific heat

NOMENCLATURE

$d'$	= coefficient in equation (III-13) = $4.574 \times 10^{-11}$ $\text{K-m}^9/\text{mole}^3$
$d''$	= coefficient in equation (III-66) = $- 2.660 \times 10^{-2}$ $\text{mole/m}^3\text{-K}^3$
$D$	= diffusivity
$e$	= thermal energy
$E_{1,2}$	= sensible heat interaction (Chapter 4)
$E_k$	= kinetic activation energy for water permeability
$f(\omega)$	= planar interface perturbation function
$f_{\text{end}}$	= solid fraction at $z^* = z^*_{\text{change}}$
$f_l$	= liquid fraction
$f_0(n, \text{Pec})$	= oblate spheroidal function (equation IV-58)
$f_p(n, \text{Pec})$	= prolate spheroidal function (equation IV-59)
$g_0(n, \text{Pec})$	= oblate spheroidal function (equation IV-60)
$g_p(n, \text{Pec})$	= prolate spheroidal function (equation IV-61)
$G_c$	= concentration gradient
$g$	= normalized temperature gradient
$h$	= perturbation expression for stability function, equation (III-57)
$h_{\text{spheroidal}}$	= spheroidal heat flux prediction at changeover
$H$	= heat flux applied at the boundary
$\hat{i}$	= unit vector in the radial direction

NOMENCLATURE (CONTINUED)

$\vec{j}$	= unit vector in the axial direction
$J_s$	= mass flux of solute
$k$	= membrane water permeability
$k_{tg}$	= membrane permeability at temperature $T_G$
$K$	= partition coefficient
$K_j^i$	= integration constant (equation (IV-57))
$K_{KR}$	= permeability to (interface speed) <sup>2</sup> ratio
$K_{s,\ell}$	= thermal conductivity
$\ell$	= half thickness of saline slab
$L^*$	= dendrite characteristic length
$L_D$	= dendrite spacing
$L_{HF}$	= latent heat of fusion
$L_{HF}^\circ$	= latent heat of fusion at $T = 273.15$ K
$m$	= $dT_E/dC_E$
MDA	= maximum difference in the activity of water
$\vec{n}$	= normal vector to the dendrite surface
$N_m^H$	= number of moles of hydrated equivalent solute in the cell
$N_w^I$	= number of moles of intracellular water
$P$	= temperature or concentration (Chapter 4)
Pec	= Peclet number
$q$	= general heat flux; co-partition parameter

NOMENCLATURE (CONTINUED)

$r_s(z)$	= dendrite radius function
$R$	= interface speed
$R_{GC}$	= universal gas constant.
$s$	= interface position
$t$	= time
$t_f$	= characteristic freezing time
$T$	= temperature
$T_G$	= reference temperature in membrane permeability expression
$T_m$	= melting temperature
$\tilde{T}$	= non-dimensional interface temperature
$U$	= convective velocity (Chapter 4)
$V_p$	= particle velocity
$v_w$	= partial molal volume of water
$w$	= solid region curvature parameter
$x$	= spatial variable, planar freezing case
$x'$	= spatial variable, moving coordinate system
$x_w^I$	= intracellular mole fraction of water
$z$	= axial coordinate, dendritic freezing case
$z^*$	= $z/L^*$
$\Delta z$	= axial coordinate measured from spheroidal origin
$\Delta z^*$	= $\Delta z/L^*$

NOMENCLATURE (CONTINUED)

$z_{\text{change}}$  = point where equilibrium and spheroidal solution regions changeover

GREEK NOMENCLATURE

$\Gamma$  = capillarity  
 $\delta$  = coordinate displacement, spheroidal region  
 $\delta$  = incremental change  
 $\epsilon_{1,2,3}$  = scaling factors (equations (IV-87) - (IV-89)).  
 $\epsilon$  = normalized density difference  
 $\eta$  = spatial variable, spheroidal coordinate system  
 $\theta$  = meridional coordinate, spheroidal coordinate system  
 $\nu$  = non-dimensional curvature parameter  
 $\rho$  = density  
 $\sigma$  = non-dimensional interface position (planar case)  
 $\tau$  = non-dimensional time  
 $\psi$  = longitudinal angle, spheroidal coordinate system  
 $\omega$  = frequency of interface perturbation  
 $\omega^*$  = non-dimensional frequency of perturbation

SUBSCRIPT

E equilibrium  
eut eutectic condition

NOMENCLATURE (CONTINUED)

$l$	liquid region
$m$	mass
$o$	oblate spheroidal system
$p$	prolate spheroidal system
$s$	solid, solute
tip	conditions at the dendrite tip
$\infty$	free-field condition

SUPERSCRIPT

$I$	intracellular
$O$	extracellular
$\sim$	normalized
'	spatial differentiation ( $d/dz$ or $d/dx$ )



CHAPTER 1 INTRODUCTION

Whole organ transplantation is an exciting new medical technique for the treatment of major disease. Under this course of treatment, patients will have diseased organs completely replaced by fully functional organs obtained from cadavers of volunteer donors. The surgical techniques for transplanting several major organs have been developed recently [1], and the transplantation of kidneys has become a relatively common clinical practice.

Organs rapidly lose viability ex vivo. As a result, donated organs must be re-implanted very soon after they become available, and this is the critical factor in the overall procedure. The time factor imposes a difficult logistic problem of finding a donor organ of the proper antigenicity at the time and place needed. The "rush" to reimplant the rapidly decaying organ also precludes careful histo-compatibility testing. Good donor-recipient "matches" are rare, so, of the transplantations actually performed, most fail because of immune rejection.

A solution to all of these problems is to form organ banks. These banks are large stores of organs of different immunological properties that are readily available. When an

organ is needed, the recipient could be carefully tissue typed, and an organ with matching antigenicity could be "withdrawn" from the bank. Unless a successful organ preservation scheme is discovered, however, organ banking will not become a reality. To date, no such procedure has been found.

Widespread interest in organ banking has recently stimulated organ preservation research. There are a few potentially useful preservation schemes including hyperbaric oxygenation [2], room temperature perfusion [3], freeze-drying [4], and simple freezing [5, 6, 7]. The most promising of these methods is preservation by simple freezing.

The fundamental damage mechanisms associated with freeze-preservation have been elucidated from experimentation with isolated cells in suspension. The viability of the frozen cell has been found to rely heavily on two factors: the cooling rate and the presence of a cryoprotective agent (CPA). The effect of cooling rate is shown in Fig. 1-1. Cooling velocity affects many physio-chemical processes in cells and so the large variation in viability is not surprising. The effect of cooling rate is important in all cell types and the relation between survival and cooling velocity is similar in that maximum survival occurs at an optimum rate. This optimum occurs over a wide range, from about 2 K/min for marrow stem cells to about 3000 K/min for the human erythrocyte.

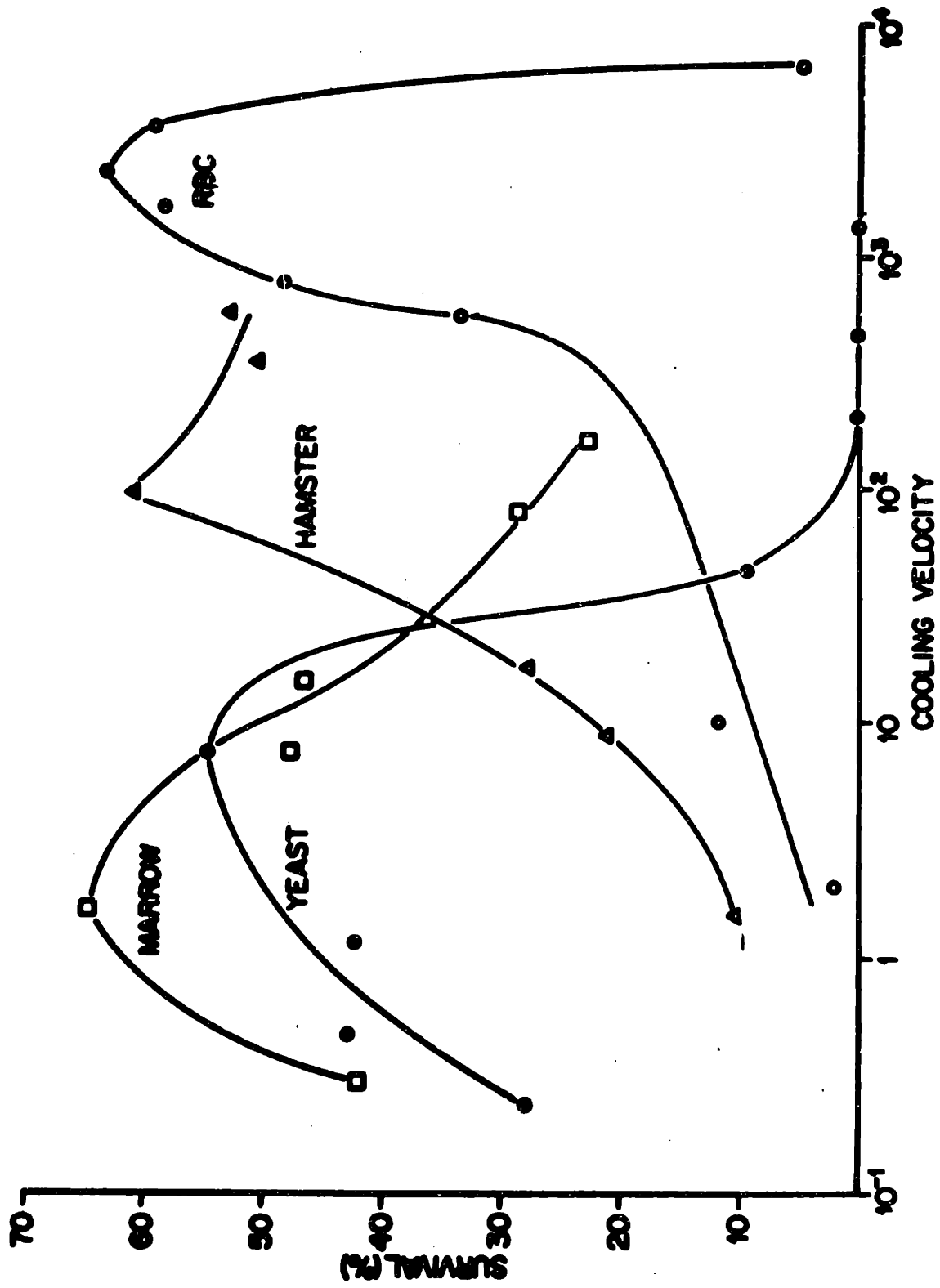


Figure (I-1) Survival as a Function of Cooling Velocity for Various Cell Types.

The generally accepted explanation for the bell-shaped survival curve is due to Mazur [8]. He suggests that survival depends on two factors: the concentration of solutes due to the formation of extracellular ice and the formation of intracellular ice. According to this theory, solution effects are responsible for injury when cooling is slower than optimal, and intracellular freezing is responsible for injury when cooling is faster than optimal. The optimum rate is slow enough to prevent production of intracellular ice and yet rapid enough to minimize solution effects.

Certain cells (e.g. erythrocytes, some microorganisms, and HeLa cells) can survive freezing in their natural media if they are cooled at optimum rates. For other types of cells, a cooling rate low enough to prevent intracellular freezing is also low enough to produce the lethal effects of concentrated solute and all cooling rates are uniformly lethal. For the case of organs which may be composed of several different cell types, only some of which may have optimum rates, the situation is further complicated by the structure and geometry of the organ. Heat transfer in a large volume of tissue will result in internal temperature gradients and a distribution of cooling rates throughout the organ. Thus, even if there was a single optimum cooling rate for all the cells of the tissue, only a very small fraction of the cells may experience that cooling rate.

The solution to this dilemma was discovered by Polge, Parkes and Smith [9] in 1949. They found that the addition of glycerol moderated the injury to cells during freezing. In principle, the survival signature of cells can be "engineered" by adding to the tissue a CPA in the appropriate concentration. The precise mechanisms of protection of CPA's is unknown, but the effect is usually a "smearing" of the survival signature so that the cell is less sensitive to cooling rate. That is, the peak of the survival signature is broadened so that good viability prevails over a range of cooling rates that may cover a few orders of magnitude.

#### I.A WATER-TRANSPORT KINETICS

The formation of extracellular ice upsets the thermodynamic equilibrium across the cell membranes by increasing the extracellular concentration of solutes. Cells respond to the phenomenon by expressing water, which increases the intracellular concentration of solutes and tends to re-establish equilibrium. Because of the resistance to water transport exhibited by all membranes, cells tend to become "supercooled", with the actual cell temperature below the equilibrium freezing temperature. If the cooling is sufficiently slow, cells can lose water rapidly enough to avoid extensive supercooling. In this case, the solutions on either side of the membrane will become progressively more concentrated, but the concentrations will remain

approximately equal. At these lower cooling rates, the cells will be exposed to concentrated solutions for longer periods of time, and "solution effects" will be responsible for cell injury. If the cooling is rapid, the cells will supercool severely, and intracellular ice will probably form. The combination of these two factors produce the "bell-shaped" curves shown in Fig. 1-1. From a kinetics point of view, the optimum cooling rate is simply the fastest rate that does not produce significant intracellular supercooling.

Several quantitative models of the kinetics of water transport [10] have been developed in recent years. These models relate thermodynamic events to certain parameters such as membrane water permeability, cellular surface area to volume ratio, and imposed thermal conditions. With these models, it is now possible to successfully predict the transport of cell water during freezing.

## I.B PRESENT CONSIDERATIONS

The purpose of this analytical investigation is to determine the cellular water transport kinetics during the freezing of large samples of biomaterial, both with and without the addition of CPA. The potential applications of this work are: (1) to identify and analyze any "anomolous" or "non-classical" damage mechanisms, and (2) to optimize the thermal pro-

tocol as a function of CPA concentration to obtain maximum organ viability.

Real tissues are immensely complicated in structure and function. To make the problem solution possible, then, the essential features of real tissue will be compiled to form an idealized model tissue illustrated in Fig. 1-2. It consists of approximately cubic cells stacked in rows and columns in a "building-block" style. These cells are assumed to be suspended in a structural protein network with saline solution filling the extracellular space.

The characteristics of the membranes and intracellular solution of real tissues have not been studied and some further modeling assumptions are necessary. The intracellular solution in the present work will be described by the pseudo-binary theory due to Levin [10]. This theory was developed to describe the hydrated protein-electrolyte-water solution of the human erythrocyte and is used here to represent a typical biological solution. Stein [11] has indicated that the human erythrocyte has the highest permeability found in mammals and that the lowest permeability is about one-tenth that of the red cell. The "idealized" membrane permeability is assumed to be a fraction of the red cell permeability (between 0.1 and 1.0) and to have same temperature dependence.

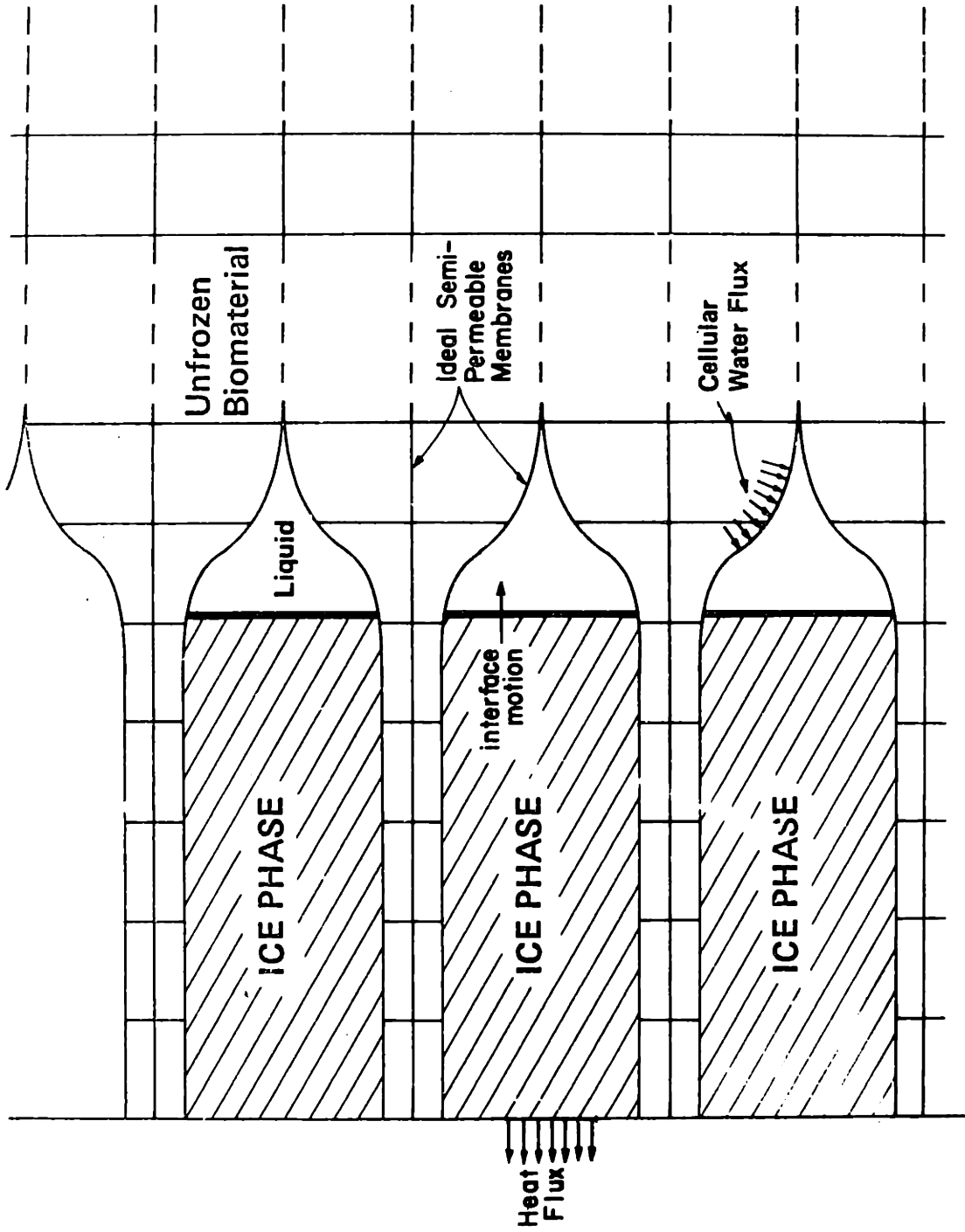


Figure (I-2) Idealized Biological Tissue



The transport properties of commonly used cryophylactic agents have not been well characterized. The data necessary for the present work includes:

- (1) thermal and mass diffusivities as a function of CPA concentration in water
- (2) the CPA-H<sub>2</sub>O equilibrium diagram and
- (3) the dendrite spacing during freezing of CPA-H<sub>2</sub>O solutions under various conditions.

From a thermal modeling point of view, the most important property of a CPA is freezing temperature depression. As a first approximation to a cryophylactic agent, the extracellular saline solution in the idealized tissue will be considered present at concentrations higher than isotonic. The NaCl-H<sub>2</sub>O solution system exhibits an equilibrium diagram typical of CPA's and has been well studied. The dendrite spacing of NaCl solutions is discussed in Appendix II.

The freezing protocol starts with a constant heat flux being imposed on the outer boundary of the tissue as shown in Fig. I-2. When the freezing temperature is reached at this boundary, ice appears and begins to propagate through the tissue\*.

---

\* the nucleation problem is not considered in this work.

As the cells express water in response to the upset in thermodynamic equilibrium, they shrink and are engulfed by the advancing solid phase. When viewed through a light microscope, the structure of the frozen biomaterial resembles "cord-like" strands of dehydrated cells immersed in a field of ice [12].

The overall solution of the problem will be a two step process. First, the temperature and concentration will be determined for the entire freezing process. These fields will be determined for the freezing of NaCl-H<sub>2</sub>O solutions at various concentrations without a biomaterial present. This represents a thermal approximation to the freezing of tissue. The temperature and concentration will depend heavily on the shape of the solid-liquid interface. An analysis of the stability of the planar interface is given in Chapter III and the transport fields are ultimately determined during dendritic freezing in Chapter IV.

The final step is to determine the thermodynamic states corresponding to these temperature and concentration fields. The departure of these states from equilibrium will determine the kinetics of cellular water transport by use of the Levin [10] model.

## CHAPTER II FUNDAMENTALS OF SOLIDIFICATION

### II.A. INTRODUCTION

The behavior of matter is almost always expressed to scientists by the observation of samples that are very large with respect to the size of a single atom; only the average or macroscopic behavior is of interest for engineering purposes. Many of the properties of materials, such as temperature, latent heat, composition and free energy, are controlled by the statistical average, although some important aspects depend on the exceptional particle. The most convenient approach to solidification theory is to consider these average or statistical properties, which can ultimately be accounted for by behavior of individual atoms.

### II.B. TWO-PHASE EQUILIBRIUM

Solidification is a process by which a solid grows by "consuming" a liquid. The condition under which the solid and liquid can coexist without any change in their relative quantities is called equilibrium; a condition in which solidification does not occur. However, if the equilibrium is perturbed only slightly, it is sufficient to cause solidification (or melting) at a substantial rate. For a pure substance at a given pressure, there is only one temperature at which equilibrium can exist, the equilibrium temperature  $T_E$ . Above this temperature, the liquid is the stable

form of the substance and below  $T_E$ , the solid is stable.

Solidification may, of course, take place in multi-component mixtures. For single-phase alloys\*, the liquid and the solid are almost always of different compositions and the temperature of equilibrium depends upon the compositions. For each composition of the liquid, there is a temperature, the liquidus temperature, at which it is in equilibrium with the appropriate solid, and conversely, each composition of solid has a solidus temperature at which it is in equilibrium with the appropriate liquid.

A plot of the liquidus and solidus temperatures as a function of composition is called an equilibrium diagram. An example for the fictitious alloy X-Y is shown in Figure II-1. Two liquidus-solidus pairs are shown in the diagram marked  $S_1, L_1$  and  $S_2, L_2$ .

There are combinations of composition and temperature that lie between the liquidus and solidus curves. The materials to which this type of diagram apply cannot exist in equilibrium in any state between that of a liquid and that of a solid; that is, there is no stable arrangement of atoms that allow the substance to

---

\* A single phase alloy is one in which equilibrium may exist between the liquid and only a single type of crystal.



exist between the solid and liquid state. If a crystalline material has a temperature and composition of this type, it will consist of part liquid and part solid. For example, if the temperature and composition is at point C in Figure II-1, it will consist of liquid at composition  $C_L$  and of solid at composition  $C_S$ .

An additional feature of equilibrium diagrams is the eutectic point. A eutectic point occurs at the intersection of two liquidus curves that slope in different directions ( $L_1$  and  $L_2$  of Figure II-1). At this point (marked "A" in Figure II-1), which is at fixed temperature and composition, the liquid is in equilibrium with the different solid phases,  $\alpha$  and  $\beta$ , at each side of the diagram. For example, if we start with a composition  $C_D$  and reduce the temperature to  $T_A + \delta$  (just above the eutectic temperature) we have a mixture of solid  $\alpha$  at composition  $C_E$  and liquid at composition  $C_A$ . If we then reduce the temperature to  $T_A - \delta$ , the mixture is a solid solution of  $\alpha$  at  $C_E$  and  $\beta$  at  $C_B$ .

The particular solution of interest in the present work is NaCl-H<sub>2</sub>O system. The equilibrium diagram for NaCl concentrations less than the eutectic is shown in Figure II-2.\* Aqueous solutions are anomalous in that they do not form solid solutions at

---

\*The NaCl-rich portion of the diagram is very complicated and is not of interest in this work.

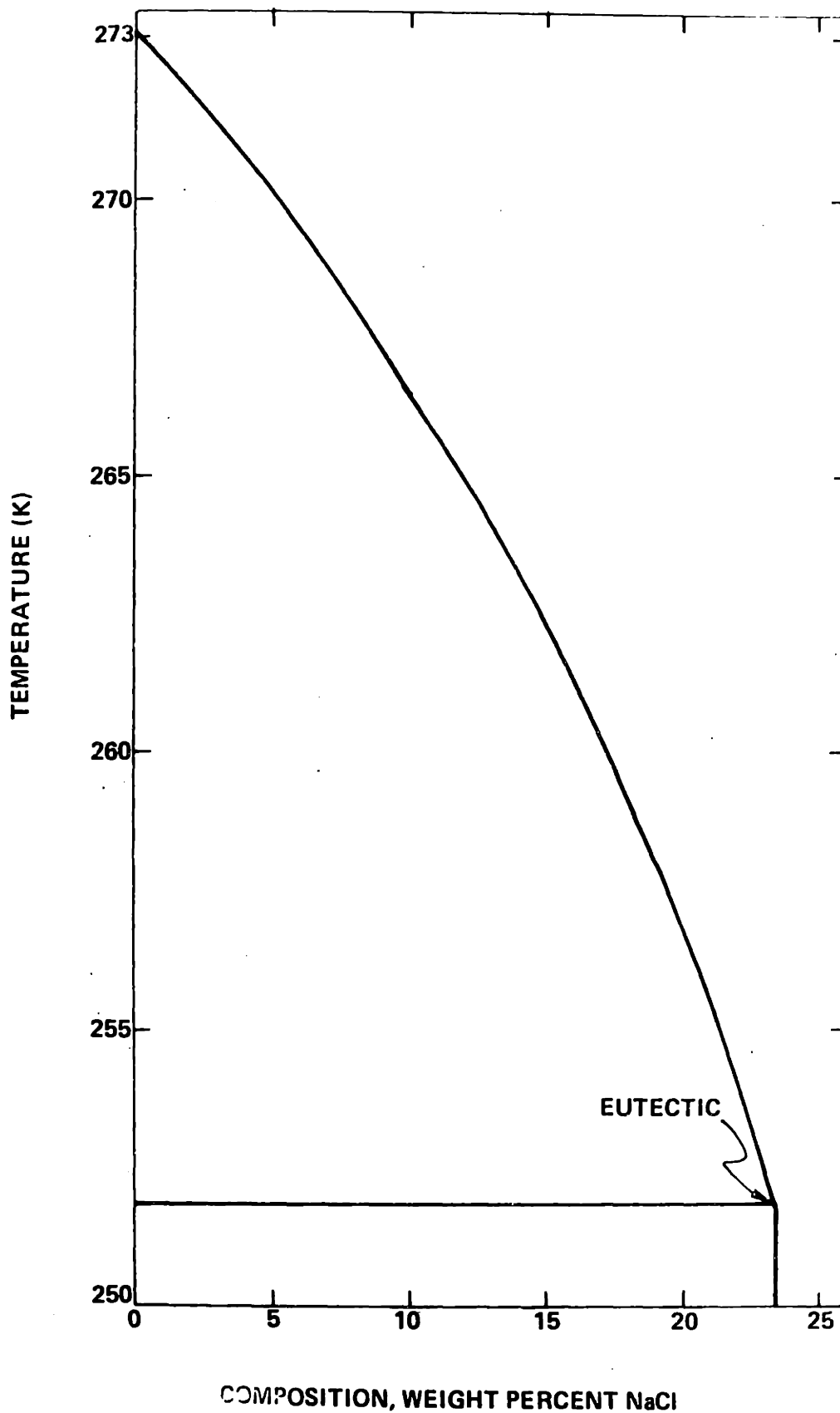


Figure (II-2) Equilibrium Diagram for NaCl-H<sub>2</sub>O

temperatures above the eutectic. The solidus corresponding to  $S_1$  in Figure II-1 is thus a vertical line at 0%  $H_2O$ . There is also a vertical "phase boundary" intersecting the eutectic point. Solid NaCl mixtures are thus composed of pure solid water and solid solution at the eutectic composition.

### II.C. KINETICS OF CRYSTAL GROWTH

The processes of freezing and melting may be analyzed by assuming that a continuous and rapid interchange of atoms between solid and liquid always takes place at a solid-liquid interface. It is convenient to consider two distinct processes, that of melting, in which atoms leave the surface and become part of the liquid, and the converse process, in which atoms from the liquid join onto the solid. The observed rate of freezing or melting is the difference between the rates of the two competing processes. If the two rates are equal, the solid and liquid are at equilibrium and the interface is at the equilibrium temperature.

While it is clear that interface motion occurs by the addition or removal of single atoms, the details of the process depend upon whether all sites on the surface are equally available for the addition of atoms and, similarly, whether all atoms are equally free to leave.

This problem may be described in terms of the relationship



between the rate of freezing or melting and the departure from the equilibrium temperature at the interface given by

$$(\Delta T)_{\text{interface}} = T_E - T_{\text{interface}} \quad \cdot \quad (\text{II-1})$$

If  $(\Delta T)_{\text{interface}}$  is zero, then the solid and liquid at the interface are in thermodynamic equilibrium and, by definition, no net change of phase may occur. However, if  $(\Delta T)_{\text{interface}}$  is positive, it becomes thermodynamically favorable for atoms to leave the liquid and join the solid, much more so than for the reverse process.

From an atomic viewpoint, there are three distinct types of solidification processes, and each leads to a different type of relationship between interface supercooling  $(\Delta T)_{\text{interface}}$  and the rate of freezing,  $R$ . Using non-equilibrium statistical mechanics, Flemings [13] explored these relationships with the following results:

- (1) If all sites for addition (or removal) of atoms to the solid-liquid interface are equivalent, then

$$R = K(\Delta T)_{\text{interface}} \quad (\text{II-2})$$

where  $K$  is an experimentally determined constant.

- (2) If the interface is atomically smooth, and new layers may form only by a nucleation process, then the rate of growth should be exponentially related to the departure from equilibrium so that

$$R = a \exp \left[ \frac{-b}{(\Delta T)_{\text{interface}}} \right] \quad (\text{II-3})$$

where a and b are experimental constants.

The energy of an atom at the surface varies sharply with the number of nearest neighbors, so that much more interface supercooling is required for a given interface speed, relative to the other growth processes.

- (3) If the atoms can arrive or leave the interface only at "steps" or local changes in surface topography, then

$$R = K(\Delta T)_{\text{interface}}^2 \quad (\text{II-4})$$

Most materials, including aqueous solutions and metallic alloys, follow the linear growth law, Equation II-2. There is great difficulty in verifying this equation for aqueous solutions which have very high diffusivity of solute in the liquid. For a typical solution, the kinetic coefficient in Equation II-2 is on the

order of 100 cm/s-K. Thus for a convenient growth rate obtained in the laboratory, such as 0.01 cm/s, the interface supercooling is on the order of  $10^{-4}$  K, a very difficult quantity to measure. Many laboratory attempts have been made to measure the relation between  $R$  and  $(\Delta T)_{\text{interface}}$  [ 14, 15 ], but the very great experimental difficulties make the numerical results open to question. The one unambiguous result of these and other experiments is that for aqueous solutions, the kinetic supercooling  $(\Delta T)_{\text{interface}}$  is very small.

When an interface is below the equilibrium temperature, and solidification takes place, the latent heat evolved tends to decrease  $(\Delta T)_{\text{interface}}$ . If the latent heat is not removed,  $(\Delta T)_{\text{interface}}$  very quickly goes to zero and no further solidification takes place. The rate of removal of the latent heat, therefore, determines the rate at which solidification will take place, and the interface supercooling will adjust itself to match the interface speed imposed by the thermal boundary conditions. From a heat transfer viewpoint, then, the interface supercooling is negligible.

#### II.D. REDISTRIBUTION OF SOLUTE DURING FREEZING

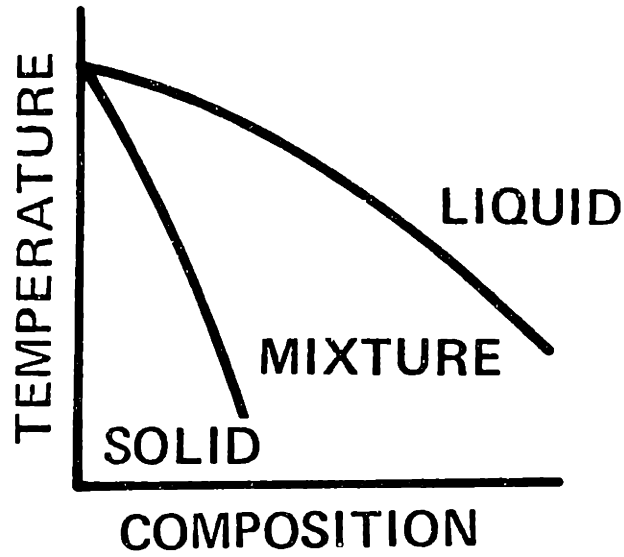
Consider an alloy of X-Y at composition  $C_0$  (see Figure II-1) which is cooled from a high temperature. When it

reaches  $T_D$ , freezing begins and the solid that forms has composition  $C_D'$ . Since the solid formed contains less solute than the initial liquid, the liquid adjacent to the interface receives the extra solute. As more energy is removed from the system, the solid phase continues to grow and reject solute to the adjacent liquid. The extra solute tends to diffuse away from the advancing front, but is partially swept back by the liquid needed to "feed" the solidification process. The build-up of solute at the interface moves the interface concentration to the right in Figure II-1, depressing the equilibrium interface temperature. The magnitude of the interface concentration is determined partly by the mixing that occurs between the liquid near the interface and the bulk liquid. In the present work, the entire system is motionless, and convective mixing is unimportant. The resulting composition of the liquid in front of the interface is very similar to that shown in Figure II-3b. A quantitative analysis of solute redistribution will be presented in a later chapter.

#### II.D.1 Constitutional Supercooling and Interface Stability

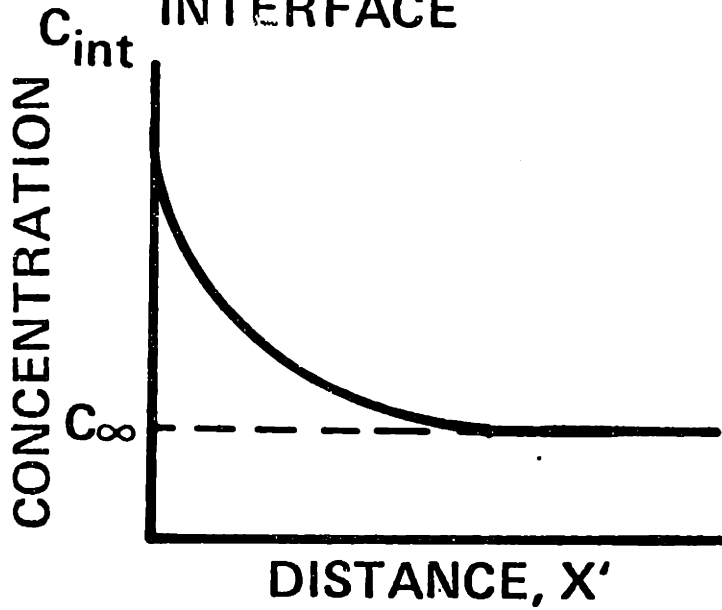
Figure II-3 shows qualitatively how the driving force for instability of the plane interface develops. A solute-rich layer is present in front of the growing interface, in which liquid composition is a maximum  $C_{int}$  at the interface and decreases with increasing distance from the interface. With the aid of the

### EQUILIBRIUM FREEZING DIAGRAM



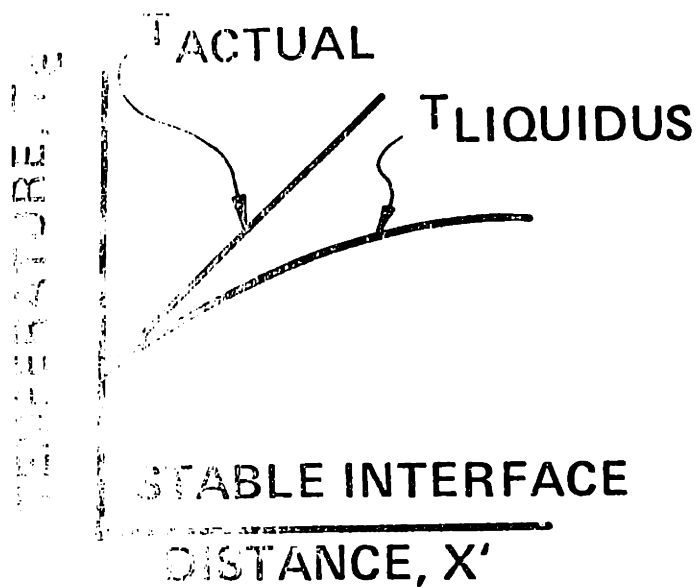
(a)

### SOLUTE ENRICHED LAYER IN FRONT OF SOLID-LIQUID INTERFACE

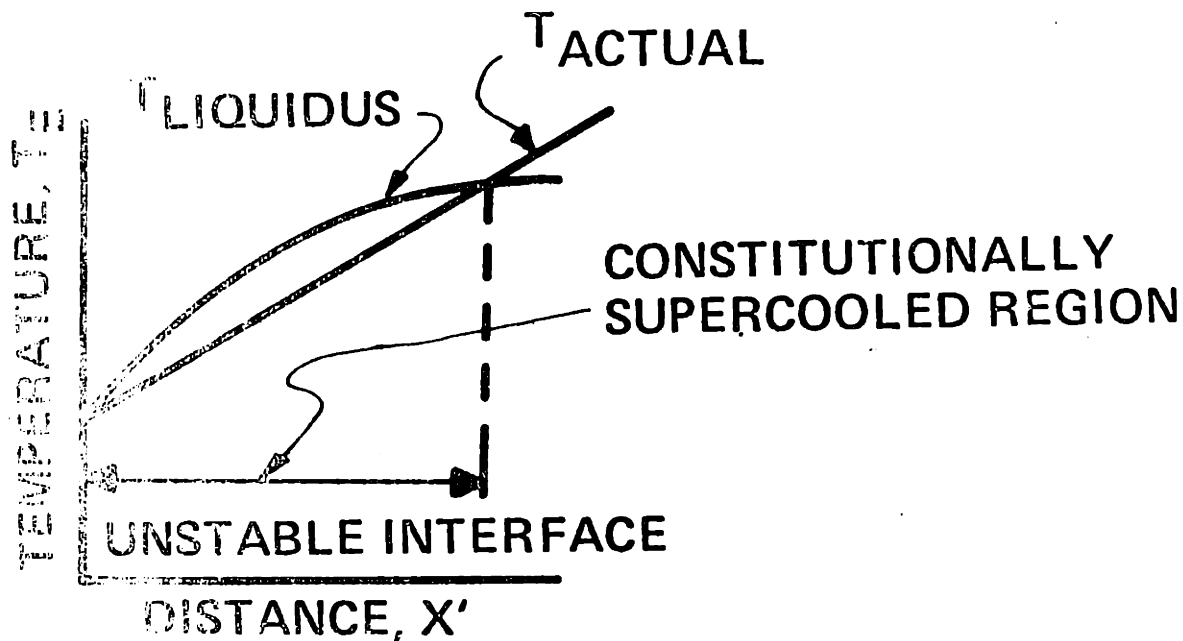


(b)

Figure (II-3a,b) Schematic Representation of Constitutional Supercooling.



(c)



(d)

Figure (II-3c,d) Schematic Representation of Constitutional Supercooling (cont.).

phase diagram, we may plot the equilibrium liquidus temperature of the liquid as a function of distance from the interface, shown in Figures II-3c and II-3d. The equilibrium liquidus temperature increases with distance from the interface, because the lower the solute content, the higher the liquidus temperature. The actual temperature ahead of the growing solid is superimposed on the same graph. Since (near) equilibrium is assumed at the interface, this curve must pass through  $T_E$  at  $X'=0$ , but otherwise is dictated by heat flow.

The curves in Figure II-3c show a condition where the interface is exactly at the equilibrium liquidus temperature and where every point in front of the interface is at a temperature above the liquidus. This represents the condition necessary for stable plane front solidification. If an instability causes a protuberance to form on the flat interface, it will find itself in a superheated environment and will melt back. Figure II-3d, however, represents an unstable case. The liquid immediately in front of the interface is at an actual temperature that is below its equilibrium liquidus temperature, and is, therefore, supercooled. Chalmers [16] termed this constitutional supercooling; constitutional indicates that the supercooling arises from a change in composition, not temperature. According to the constitutional supercooling theory, this supercooling results in instability of the plane front since

any protuberance forming on the interface would find itself in supercooled liquid and would not disappear.

### II.D.2 Higher Interface Structures

Experiments on transparent organic liquids show that as a planar interface becomes unstable, it first becomes gently undulatory, with protrusions later developing into the fully formed cellular dendrites shown in Fig.-II-4. These observations are in qualitative agreement with predictions of the time dependent interface stability theory.

A schematic representation of cellular dendritic solidification is shown in Figure II-5. Cells protrude into the liquid, and the intercellular liquid becomes increasingly enriched with distance back from the tips. Assuming the phase diagram is represented by Figure II-1, the maximum concentration of solute that can be attained by the intercellular liquid is  $C_{eut}$ . The liquid does, in fact, reach this composition even when the initial composition is a very small fraction of  $C_{eut}$ . The average liquid composition at any distance along the growth axis decreases to the average value  $C_{tip}$  at the dendrite tips and finally, to the bulk composition at a distance far from the cell tips.

The solution that is in the free field undergoes one of



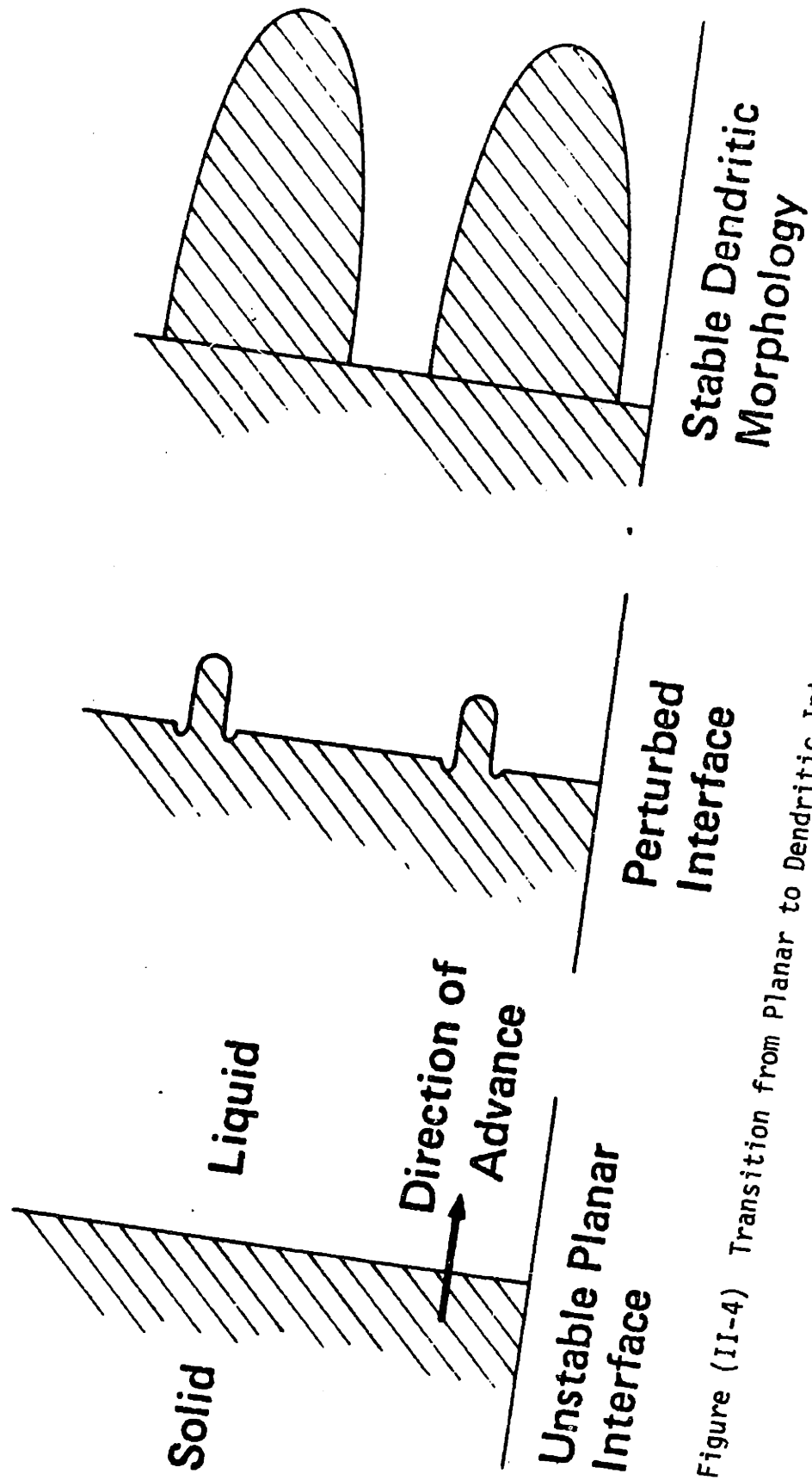


Figure (II-4) Transition from Planar to Dendritic Interface Morphology

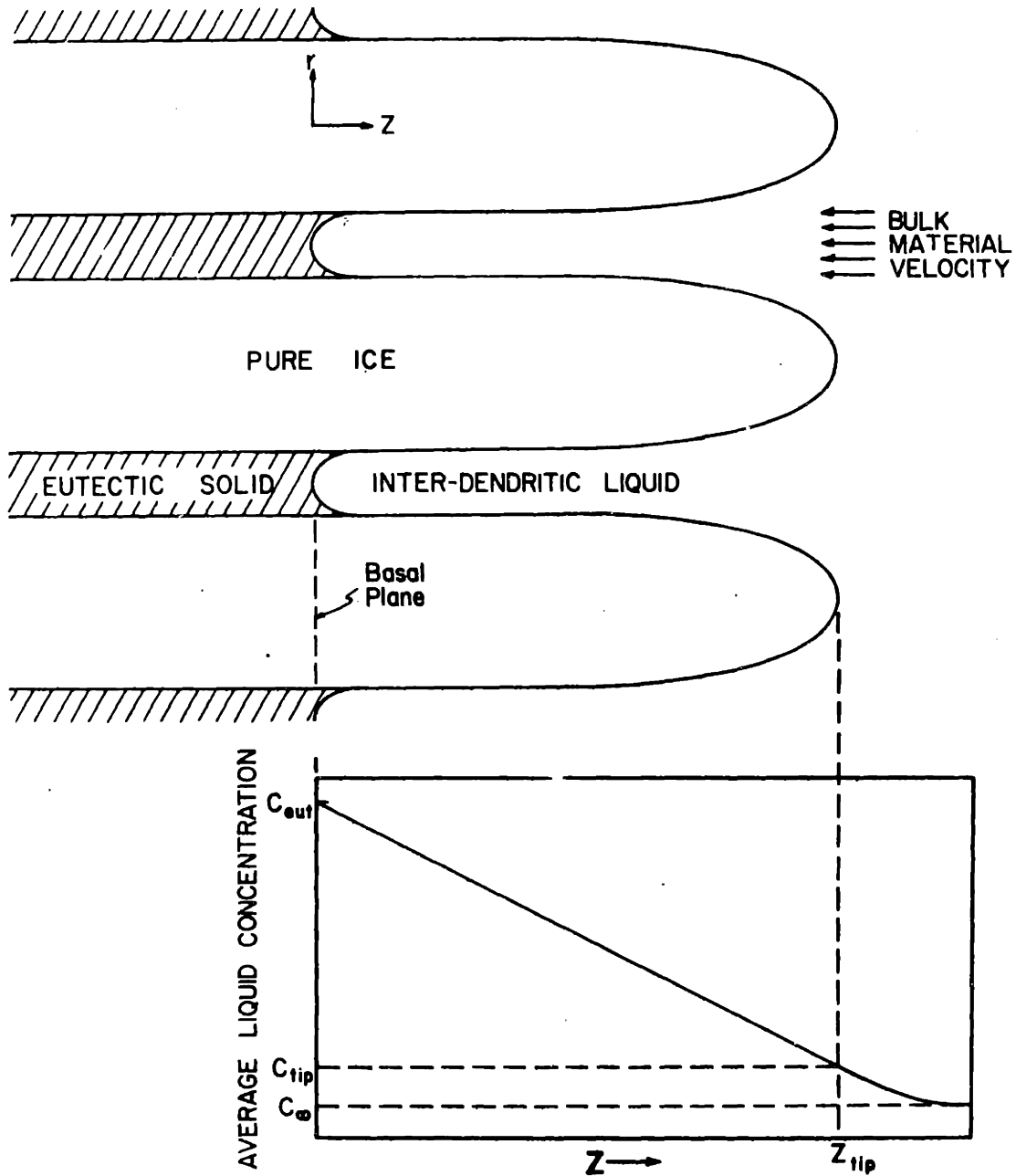


Figure (II-5) Schematic Representation of Steady Dendritic Freezing.

two types of changes as it approaches the phase boundary. Some of the solution will be intercepted by the extended portion of the interface (the dendrites). Since solute is completely rejected by the pure ice, this first phase change is from liquid solution to pure ice. The solute that is rejected from the dendrite surface enters the interdendritic volume, which provides solute enrichment as described above. The solution that enters the interdendritic space undergoes the second type of transition and becomes more and more enriched until the eutectic condition is reached at the basal plane and eutectic solid is formed. The resulting solidified matrix is thus striated with alternate bands of pure ice and eutectic solid (see Figure II-5).

CHAPTER III STABILITY OF THE PLANAR FREEZE FRONT  
IN THE BINARY SYSTEM NaCl-H<sub>2</sub>O

III.A. INTRODUCTION

In this chapter, the thermodynamic stability of a planar solid-liquid interface will be evaluated during the freezing of a slab of saline solution. If the analysis indicates that the interface is unstable, then the interface will experience a transition to the dendritic or cellular dendritic type. Analysis of the heat and mass transfer during dendritic solidification is accomplished in Chapter 4.

The Mullins-Sekerka stability criterion [17] will be used in this analysis, which provides quantitative stability information as a function of the thermal and diffusional conditions imposed on the interface. Application of the criterion requires the complete temperature and concentration profiles as a function of time. These profiles are obtained by applying conservation of mass and energy to the solidification field and solving the resulting equations.

The planar freezing geometry is shown schematically in Figure III-1. Heat is extracted at constant flux rate from the plane at  $x = 0$ . The region  $0 \leq x \leq s$  is occupied by solid water (ice) and the region  $s < x \leq \ell$  is occupied by a NaCl-H<sub>2</sub>O

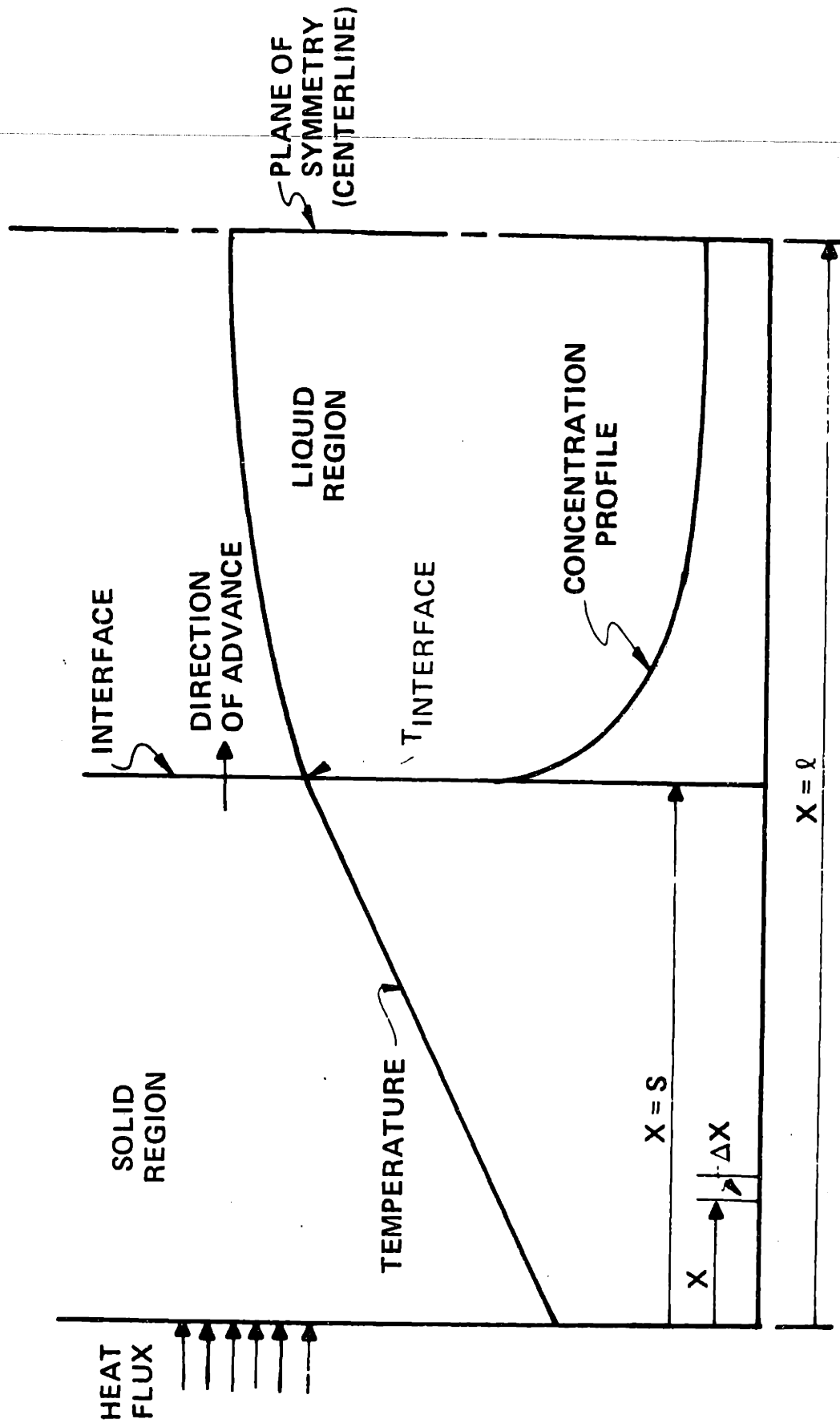


Figure (III-1) Planar Freezing Geometry.

solution. The solid-liquid interface is located at  $x = s(t)$  and the plane  $x = \ell$  is a plane of symmetry, representing the center of a planar slab of thickness  $2\ell$ . The field is infinite in extent in the vertical direction and in the direction normal to the paper.

### III.B TRANSPORT EQUATIONS AND BOUNDARY CONDITIONS

#### III.B.1 Heat Transfer Equations

In the space between  $x=0$  and  $x=\ell$ , there exists two separate homogeneous bodies, pure solid water and liquid saline solution, experiencing a transient in temperature distribution. At any instant of time, the net heat flux into the element  $\Delta x$  (see Figure III-1) is:

$$q(x) - q(x+\Delta x) = - \left( \frac{\partial q(x)}{\partial x} \right) \Delta x \quad (\text{III-1})$$

From the first law of thermodynamics, this net heat flux must be equal to the rate of increase of internal energy  $\partial(A\Delta x\rho e)/\partial t$ . Equating these, and cancelling  $\Delta x$ , this energy conservation equation becomes:

$$- \frac{\partial}{\partial x} \left( \frac{q}{A} \right) = \rho \frac{\partial e}{\partial t} . \quad (\text{III-2})$$

For solids and for incompressible liquids,  $\partial e$  may be expressed as  $C\partial T$ . Utilizing Fourier's equation of heat conduction,

$$\left(\frac{q}{A}\right) = - K \frac{\partial T}{\partial x} \quad (\text{III-3})$$

equation (III-2) becomes

$$\frac{\partial}{\partial x} \left( K \frac{\partial T}{\partial x} \right) = \rho C \frac{\partial T}{\partial t} \quad (\text{III-4})$$

Assuming that the thermal conductivity does not vary with temperature, we have

$$D_i \frac{\partial^2 T_i}{\partial x^2} = \frac{\partial T_i}{\partial t} \quad (\text{III-5})$$

where  $i = s, l$  refers to the solid and liquid regions, respectively.

### III.B.2 Mass Transfer Equation

In order to treat the mass transfer problem quantitatively, it is necessary to employ specific assumptions. The problem which will be considered is that of the end-to-end segregation which accompanies the solidification of an impure binary melt of uniform cross-section. The following assumptions will be used:

- (1) During the initial phase of the freezing process, solute is completely rejected from the solid-liquid interface, i.e., the solute concentration in the solid is everywhere zero. After the concentration at the interface increases to the eutectic value, solute is incorporated in the solid phase and the concentration at the interface remains constant.
- (2) The volume change on freezing is about 8% (varies slightly with concentration) and may be ignored without appreciable error (See Section IV-A.2).
- (3) The entire freezing field is assumed motionless with respect to a laboratory reference frame. Since it is assumed that there is no volume change on freezing, there is no bulk motion of material in the liquid phase and convective mixing may be ignored.
- (4) The rate of advance of the solid-liquid interface is essentially constant.
- (5) The diffusion coefficient of the solute in water is constant.

The conservation equation for mass transfer follows a development similar to that for energy conservation. If the space between  $x = s$  and  $x = \ell$  is occupied by water with a single



solute diffusing ahead of the interface, the net rate of solute diffusing into the element  $\Delta x$  is

$$J_s(x) - J_s(x+\Delta x) = - \frac{\partial J_s(x)}{\partial x} \Delta x \quad . \quad (\text{III-6})$$

Then, by conservation of mass this should equal the rate of accumulation of solute in the element or  $\partial(A\Delta x C_s)/\partial t$ . Then

$$- \frac{\partial}{\partial x} \left( \frac{J_s}{A} \right) = \frac{\partial C_s}{\partial t} \quad . \quad (\text{III-7})$$

Using Fick's second law of diffusion,

$$\frac{J_s}{A} = - D_m \frac{\partial C_s}{\partial x} \quad (\text{III-8})$$

we have,

$$\frac{\partial}{\partial x} \left( D_m \frac{\partial C_s}{\partial x} \right) = \frac{\partial C_s}{\partial t} \quad . \quad (\text{III-9})$$

Equation (III-9) is written with respect to a "laboratory fixed" or inertial reference frame. It would be much more convenient to use a reference frame fixed with respect to the solid-liquid interface. Using the transformation

$$x' = x - Rt \quad (III-10)$$

equation (III-9) becomes

$$D_m \frac{\partial^2 C_s}{\partial x'^2} + R \frac{\partial C_s}{\partial x'} = \frac{\partial C_s}{\partial t} \quad (III-11)$$

where  $R$  is the interface velocity. The coordinate  $x'$  is measured away from the interface, so at  $x' = 0$ ,  $x = Rt = s(t)$ .

### III-B.3 Boundary Conditions

In addition to equations (III-5) and (III-11), several initial and boundary conditions must be specified to complete the problem statement.

- (1) The temperature profiles generated by equation (III-5) must match at the interface, i.e.,

$$T_s = T_l = T_{\text{interface}} \text{ at } x=s, \text{ all } t \quad (III-12)$$

Assuming that the solid phase and the liquid solution just adjacent to it are essentially in thermal equilibrium, then the interface solute concentration, specified by the mass conservation equation, will determine the interface temperature from the locus

of two-phase equilibrium states. For a sodium chloride solution, this locus may be approximated by

$$T_E = a' + b'C_E + c'C_E^2 + d'C_E^3 \quad (\text{III-13})$$

which results from a least-squares curve fit of freezing point data.

- (2) The imposed heat flux at the exterior boundary specifies the temperature gradient by use of the Fourier conduction law

$$\frac{\partial T_s}{\partial x} = -\frac{H}{K_s} \text{ at } x = 0 \text{ all } t \quad (\text{III-14})$$

where  $H$  is positive for heat added to the system (thermodynamic convention). Similarly,

$$\frac{\partial T_\ell}{\partial x} = 0 \text{ at } x = \ell \text{ all } t \quad (\text{III-15})$$

since  $x = \ell$  is a plane of symmetry, where the heat flux must vanish.

(3) Moving Boundary Condition. The final thermal boundary condition is simply the first law of thermodynamics applied to the interface (see Figure III-2). Considering a control volume of infinitesimal thickness  $dx$  centered on the interface, we have

$$K_s \left. \frac{\partial T_s}{\partial x} \right|_{x=s} - K_l \left. \frac{\partial T_l}{\partial x} \right|_{x=s} = \rho_s L_H \frac{ds}{dt} \quad (\text{III-16})$$

The left-hand side of equation (III-16) represents the net heat flux out of the control volume as calculated by the Fourier conduction law. The material moving through the control volume is changing its thermodynamic state from liquid to solid water. The right-hand side of equation (III-16) is the rate of liberation of the latent heat of fusion due to this change of state.

Equation (III-16) is called the "moving boundary condition" and is the major mathematical complication in this problem. It is a true boundary condition since the equation holds only at  $x = s$ , but it is also an ordinary differential equation relating interface position to time. Because of this fact,

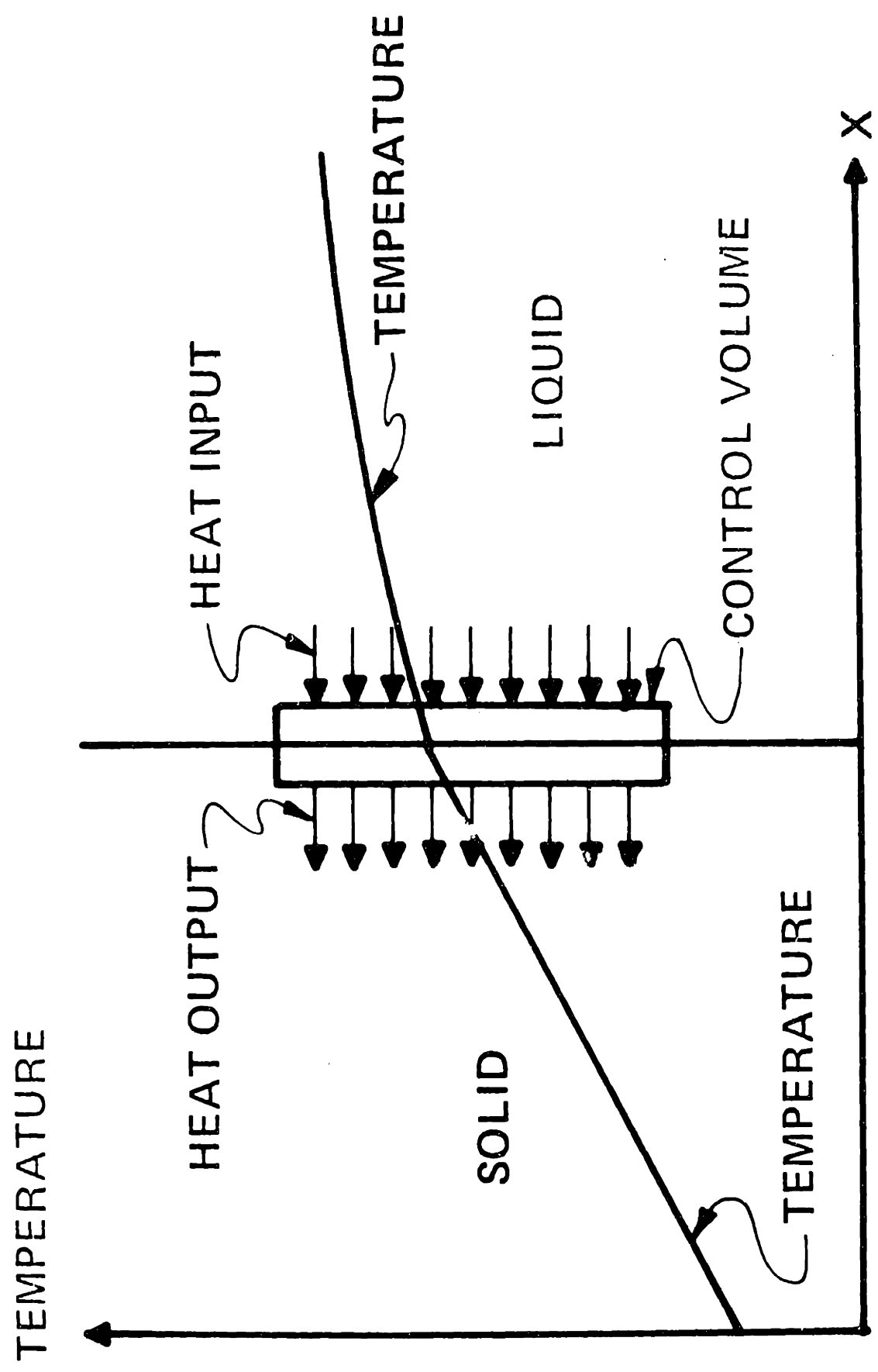


Figure (III-2) Energy Balance at the Moving Interface.

equation (III-16) increases the system order by one.

- (4) Complete rejection of solute from the ice phase is expressed by setting the absolute particle velocity to zero in the moving ( $x'$ ) coordinate system. Rohsenow and Choi [18] express this particle velocity as

$$V_p = \frac{D_m}{C_s} \frac{\partial C_s}{\partial x'} + R \quad (\text{III-17})$$

which is the sum of the diffusive (first term) and bulk convective solute flux. Setting this velocity to zero, we have for the present case

$$D_m \frac{\partial C_s}{\partial x'} + RC_s = 0 \quad \text{at} \quad x' = 0 \quad . \quad (\text{III-18})$$

Since  $R$ ,  $D_m$  and  $C_s$  are positive for all  $x'$ , the concentration gradient must be negative at the interface. After the eutectic concentration is reached at the interface, equation (III-18) is replaced by

$$C_s = C_{eut} \quad \text{at} \quad x' = 0 \quad (\text{III-19})$$

and the interface concentration and temperature

subsequently remain constant.

- (5) Similar to boundary condition (2), the diffusive flux must vanish at  $x = \ell$  or at  $x' = \ell - s(t)$ ,

$$\frac{\partial C_s}{\partial x'} = 0 \quad \text{at } x' = \ell - s(t) \quad (\text{III-20})$$

#### III-B.4 Initial Conditions

At time zero, the entire field is assumed in a state of uniform cooling, i.e.,

$$\frac{dT}{dt} = B = \text{constant, at } t = 0, \text{ all } x. \quad (\text{III-21})$$

We will start our consideration of the problem when solid phase has just started to form at  $x = 0$ . No solute redistribution has taken place at this time so the concentration is everywhere uniform at its initial value  $C_0$ . The interface temperature of the newly formed solid phase is given by equation (III-13) with  $C_E = C_0$ .

The initial temperature profile is found by solving the thermal diffusion equation (III-5) subject to the boundary conditions (III-14), (III-15) and (III-13) and the uniform cooling condition (III-21). Solving these equations we have

$$T_{\ell} = T_{\ell}(x=0) - \frac{H}{K_{\ell}} x + \frac{H}{2K_{\ell}\ell} x^2 \quad \text{at } t = 0 \quad \text{(III-22)}$$

$0 < x < \ell$

Equation (III-22) shows that an initially parabolic temperature distribution exists in the unfrozen tissue and is a function of the imposed heat flux and the freezing temperature. The temperature profile is exactly parabolic only for  $t \leq 0$  and will be perturbed when a substantial amount of ice has formed. The profiles may be approximated as parabolic, a concept which will be developed in the next section.

Table (III-1) summarizes the heat and mass transport equation with the associated initial and boundary conditions. The system consists of three coupled partial differential equations, and twelve initial and boundary conditions, two of which are applied at a moving boundary.



	Solid Region	Liquid Region
Heat Transfer Equations	$D_s \frac{\partial^2 T_s}{\partial x^2} = \frac{\partial T_s}{\partial t}$	$D_\ell \frac{\partial^2 T_\ell}{\partial x^2} = \frac{\partial T_\ell}{\partial t}$
Mass Transfer Equations	$C_s = 0$	$D_m \frac{\partial^2 C_s}{\partial x'^2} + R \frac{\partial C_s}{\partial x'} = \frac{\partial C_s}{\partial t}$
Boundary Conditions	$K_s \frac{\partial T_s}{\partial x} = -H$ at $x=0$ , all $t$	$\frac{\partial T_\ell}{\partial x} = 0$ at $x = \ell$ , all $t$
	$T_s = T_{\text{interface}}$ at $x=s$ , all $t$	$T_\ell = T_{\text{interface}}$ at $x=s$ , all $t$
	$K_s \frac{\partial T_s}{\partial x} - K_\ell \frac{\partial T_\ell}{\partial x} = \rho_\ell L_{HF} \frac{ds}{dt}$ at $x=s$ , all $t$	
	$C_{\text{interface}} = C_{\text{eutectic}}$ $t \geq t_{\text{eut}}, x' = 0$	$D_m \frac{\partial C_s}{\partial x'} + RC_s = 0$ at $x'=0$ $0 \leq t < t_{\text{eut}}$
	-----	$\frac{\partial C_s}{\partial x'} = 0$ at $x'=\ell-s(t)$ , all $t$
$T_{\text{interface}} = a + b'C_{\text{interface}} + c'C_{\text{interface}}^2 + d'C_{\text{interface}}^3$		
Initial Conditions	-----	$C_s = C_0$ at $t=0$ , all $x'$
	$T_s = f(C_0)$ at $t=0$ , $x=0$	$T_\ell = g(x)$ at $t=0$ , all $x$
	$s = 0$ at $t = 0$	

TABLE 1 Heat and Mass Transfer Equations, Boundary and Initial Conditions

### III-C METHOD OF SOLUTION

#### III-C.1 Temperature Profiles

The heat conduction problem involving the change of phase of a binary alloy is non-linear primarily because of the moving boundary condition and because of the interface temperature depression from the build-up of solute. Few exact solutions to this class of problems exist. The most important exact solution was found by Neumann [19] who determined the temperature distribution and rate of freezing of a semi-infinite body of pure substance. Evans, Isaacson and MacDonald [20] have presented some solutions for the location of the interface in the form of a Taylor series, the convergence of which is undetermined. Rubenstein [21] and Weiner [22] studied multiple phase change problems and obtained solutions similar to Neumann's. All of these exact solutions apply to problems which are much simpler than the present case.

Numerical solution of change-of-phase problems presents formidable mathematical difficulties. Landau [23] has presented a set of solutions to these problems using a finite-difference approximation to the heat conduction equation. The intricate calculations required for a finite difference solution with a change of phase are presented in detail by Forster [24]. The procedure is very tedious, and what is more, it must be repeated

each time a parameter is changed. It is expensive and time-consuming, and considered unwarranted for an analysis at this level of sophistication.

### III-C.2 Heat Balance Integral

One of the most useful techniques for solution of non-linear conduction problems is the heat balance integral technique developed originally by Pohlhausen [25] and Kármán [26] and modified by Goodman [27 - 29]. The method consists of assuming the spatial form of the temperature distribution (usually a power series) and solving an "averaged" form of the heat conduction equation, called the heat balance integral. The problem is reduced by this method to ordinary differential equations in time only.

Satisfying the heat conduction equation (III-5) on the average over  $0 \leq x \leq s$  for  $i = s$  and  $s \leq x \leq \ell$  for  $i = \ell$ , is exactly equivalent to applying the conservation of energy to each of these regions as a whole\*. We assume temperature profiles of

---

\*It may be demonstrated mathematically that the two approaches are equivalent. Multiplying equation (III-5) by  $dx$  and integrating from 0 to  $s$  for  $i = s$  and from  $s$  to  $\ell$  for  $i = \ell$  yields expressions equivalent to equations (III-27) and (III-30).

the form

$$T_s = a_1 + b_1x + c_1x^2 \quad (\text{III-23})$$

and

$$T_\ell = a_2 + b_2x + c_2x^2 \quad (\text{III-24})$$

Using conditions (III-12), (III-14) and (III-15), equations (III-23) and (III-24) become

$$T_s = T_{\text{interface}} + \frac{H(s-x)}{K_s} - c_1(s^2-x^2) \quad (\text{III-25})$$

and

$$T_\ell = T_{\text{interface}} + 2c_2\ell(s-x) - c_2(s^2-x^2) \quad (\text{III-26})$$

By using the boundary conditions in the assumed temperature profiles, we have reduced the heat transfer problem to one of determining  $c_1$ ,  $c_2$  and  $s$  as a function of time. The variables  $c_1$  and  $c_2$  are the quadratic coefficients in the temperature profiles and represent their curvature. They also indirectly reflect the importance of thermal mass, since the profiles would have no curvature if the thermal mass were zero. Figure (III-3) shows typical profiles and their variation with the curvature parameters. Because of the zero-slope boundary condition at  $x = \ell$ , low values of the curvature parameter

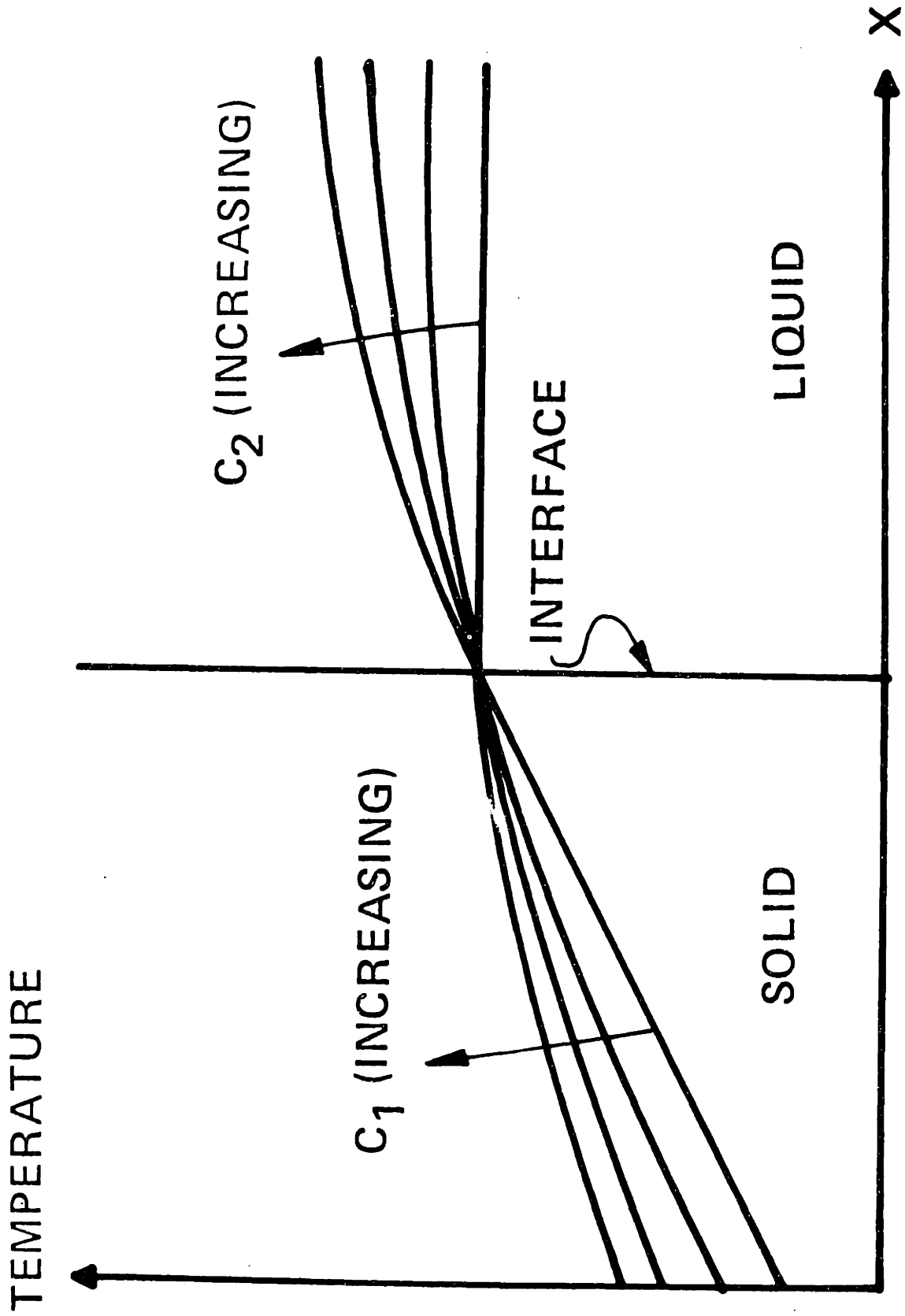


Figure (III-3) Typical Temperature Profiles and their Variation with  $C_1$  and  $C_2$ .

in the liquid region indicate a flat profile as well as a linear one.

Consider two control volumes, fixed with respect to the laboratory reference frame, one containing all of the solid, and the other containing the liquid. Each of these volumes contains a changing quantity of substance and is thus an open system.

Conservation of energy for the two region becomes:

$$\text{Solid Region} \quad H + K_s \left( \frac{\partial T}{\partial x} \right)_{x=s} = \frac{K_s}{D_s} \frac{\partial}{\partial t} \int_0^s T_s \, dx \quad (\text{III-27})$$

and

$$\text{Liquid Region} \quad -K_l \left( \frac{\partial T_l}{\partial x} \right)_{x=s} = \frac{K_l}{D_l} \frac{\partial}{\partial t} \int_s^l T_l \, dx \quad (\text{III-28})$$

Note that the integrals on the right-hand side of equations (III-27) and (III-28) account for the change of internal energy in the control volumes both by a change of temperature and by a change in the amount of mass in the system. Using equations (III-25) and (III-26) in equations (III-27) and (III-28), we obtain after manipulation

$$2D_s c_1 s = s \frac{d T_{\text{interface}}}{dt} + \left( \frac{Hs}{K_s} - 2c_1 s^2 \right) \frac{ds}{dt} - \frac{2s^3}{3} \frac{dc_1}{dt}$$

(III-29)

and

$$2D_{\ell}c_2(\ell-s) = -2/3(\ell-s)^3 \frac{dc_2}{dt} + 2c_2(\ell-s)^2 \frac{ds}{dt} + (\ell-s) \frac{dT_{\text{interface}}}{dt} \quad (\text{III-30})$$

Finally, equations (III-25) and (III-26) are used in the moving boundary condition, equation (III-16), to obtain

$$\rho_{\ell}L \frac{ds}{dt} = -H + 2K_S c_1 s + 2K_{\ell} c_2 (\ell-s) \quad (\text{III-31})$$

Using the non-dimensional variables

$$\sigma = s/\ell \quad (\text{III-32})$$

$$v = \frac{c_2 K_{\ell} \ell}{H} \quad (\text{III-33})$$

$$w = \frac{c_1 K_S \ell}{H} \quad (\text{III-34})$$

$$\tau = \frac{D_{\ell} t}{\ell^2} \quad (\text{III-35})$$

and

$$\tilde{T} = \frac{K_{\ell} T_{\text{interface}}}{H\ell} \quad (\text{III-36})$$

equations (III-29), (III-30) and (III-31) become after rearranging

$$\frac{d\sigma}{d\tau} = \frac{H\ell}{D_{\ell} \rho_{\ell} L_{HF}} \{2\sigma w + 2\nu(1-\sigma) - 1\} \quad (\text{III-37})$$

$$\frac{dw}{d\tau} = \frac{3}{2\sigma^2} \left\{ K_{s\ell} \frac{d\tilde{T}}{d\tau} - D_{s\ell} w + \frac{H\ell}{D_{\ell} \rho_{\ell} L_{HF}} (1-2w\sigma)(2w\sigma + 2\nu(1-\sigma) - 1) \right\} \quad (\text{III-38})$$

$$\frac{d\nu}{d\tau} = 3 \frac{H\ell}{D_{\ell} \rho_{\ell} L_{HF}} \left\{ \frac{2w\sigma - 1 + 2\nu(1-\sigma)}{(1-\sigma)} \right\} \nu + \frac{3}{2(1-\sigma)^2} \left\{ \frac{d\tilde{T}}{d\tau} - 2\nu \right\} \quad (\text{III-39})$$

These are three ordinary differential equations in the four unknowns  $\nu$ ,  $w$ ,  $\sigma$  and  $\tilde{T}$ . To complete the problem application, the variation of the interface temperature with time must be determined. Calculating the interface concentration as a function of time and applying the equilibrium freezing point equation (III-13) will provide the necessary information.

### III-C.3 Mass Transfer Solution

If we assume that the characteristic length of the concentration profile is much less than the length of the liquid region ( $\ell-s$ ), then the slope of the profile will decrease to zero far from the plane of symmetry ( $x=\ell$ ). In this case equation (III-18) is equivalent to

$$C_s = C_0 \text{ as } x' \rightarrow \infty \text{ for all } t. \quad (\text{III-40})$$



Equation (III-11) together with boundary conditions (III-17) and (III-40) has been solved by Smith, Tiller and Rutter [30] by the LaPlace Transform method, and is given by

$$\begin{aligned}
 C_s = C_0 + \frac{C_0}{2} \frac{q}{1-q} \exp\left[-\frac{Rx'}{D_m}\right] \operatorname{erfc}\left\{\frac{x'-Rt}{2\sqrt{D_m t}}\right\} - \frac{C_0}{2} \operatorname{erfc}\left\{\frac{(k'+Rt)}{2\sqrt{D_m t}}\right\} \\
 + \frac{C_0}{2} \exp\left\{-q\left(\frac{R}{D_m}\right)(x'+(1-q)Rt)\right\} \operatorname{erfc}\left\{\frac{x'+(2K-1)Rt}{2\sqrt{D_m t}}\right\} \\
 - \frac{C_0}{2} \frac{q}{1-q} \exp\left\{-\frac{qR}{D_m}(x'+KRt)\right\} \operatorname{erfc}\left\{\frac{(x'+(2K-1)Rt)}{2\sqrt{D_m t}}\right\} \quad \text{(III-41)}
 \end{aligned}$$

This result is for the general case where solute enters the solid phase according to the relationship.

$$C_s(\text{solid}) = K C_s(\text{liquid}) \text{ at } x' = 0 \quad \text{(III-42)}$$

where  $K$  is called the partition coefficient and  $q = 1 - K$ . The quantity  $R$  is the "pseudo-steady" interface speed at any instant of time. Equation (III-41) was obtained for the case of exactly constant interface speed and represents an approximation to the solution of the present problem. An analysis of the variation of the interface speed will be done to determine the validity of this approximation. The second and fifth terms in equation (III-41) has the form 0/0 in the limit as  $q \rightarrow 1$  and  $K \rightarrow 0$  (i.e., as  $C_s(\text{solid}) \rightarrow 0$ ).

We may, therefore, apply L'Hospitals rule to obtain after substantial manipulation,

$$\begin{aligned} \frac{C_s(x')-C_0}{C_0} &= [\operatorname{erfc} \left\{ \frac{x'-Rt}{2\sqrt{D_m t}} \right\}] \left[ \frac{1}{2} e^{-\frac{Rx'}{D_m}} - \frac{1}{2} \frac{R}{D_m} (x'-Rt) e^{-\frac{Rx'}{D_m}} \right] \\ &- \frac{1}{2} \operatorname{erfc} \left\{ \frac{(x'+Rt)}{2\sqrt{D_m t}} \right\} + \frac{1}{\sqrt{\pi}} \frac{Rt}{\sqrt{D_m t}} e^{-\frac{Rx'}{D_m}} e^{-\frac{(x'-Rt)^2}{2D_m t}} \end{aligned} \quad (\text{III-43})$$

The interface concentration is obtained by setting  $x' = 0$  in equation (III-43) which gives

$$\frac{C_s(x'=0)-C_0}{C_0} = \operatorname{erf} \psi + 2\psi^2(1+\operatorname{erf} \psi) + \frac{2\psi}{\sqrt{\pi}} e^{-\psi^2} \quad (\text{III-44})$$

where  $\psi = \frac{R}{2} \sqrt{\frac{t}{D}}$ .

When the eutectic concentration is reached at the interface, the concentration becomes constant and its spatial distribution approaches a steady shape. Under these conditions, the concentration profile becomes [30 ]:

$$\frac{C_s}{C_0} = 1 + \frac{1 - \frac{C_0}{C_{\text{eut}}}}{\frac{C_0}{C_{\text{eut}}}} \exp\left(-\frac{R}{D_m} x'\right) \quad (\text{III-45})$$

and is independent of time. Equation (III-45) represents a "limit"

of equation (III-41) and exhibits the most severe interface concentration gradient possible. Use of these limiting conditions will be made in a later section.

Since equilibrium has been assumed between solid and liquid at the interface, the interface temperature may be specified by the freezing point equation (III-13) using the interface concentration as expressed by equation (III-44) or (III-45). To obtain an expression for  $\frac{d\tilde{T}}{d\tau}$ , we use the chain rule to obtain

$$\frac{d\tilde{T}}{d\tau} = \frac{dC_{\text{interface}}}{d\tau} \frac{d\tilde{T}}{dC_{\text{interface}}} \quad (\text{III-46})$$

where

$$\frac{d\tilde{T}}{dC_{\text{interface}}} = \frac{K_{\ell}}{H_{\ell}} (b' + 2c' C_{\text{interface}} + 3d' C_{\text{interface}}^2) \quad (\text{III-47})$$

(using equation (III-13)) and  $C_{\text{interface}}$  and  $\frac{dC_{\text{interface}}}{d\tau}$  are obtained from equation (III-44) and its first derivative. These substitutions are most conveniently done numerically on a digital computer at the time of simulation. Note that after the eutectic concentration is reached at the interface, the concentration and temperature are constant and  $\frac{d\tilde{T}}{d\tau} = 0$ .

#### III-C.4 Initial Conditions for the Integral Method

Consideration of the problem will start with the system in a state of uniform cooling and solid phase just starting to appear. Therefore at  $\tau = 0$ ;  $\sigma = 0$ ,  $C_{\text{interface}} = C_0$ , and  $T_{\text{interface}}$  is given by equation (III-13). Since the solid phase at this time has infinitesimal thickness, its thermal mass is also infinitesimal and

$$w = 0 \quad \text{at } \tau = 0 \quad . \quad \text{(III-48)}$$

The condition of uniform initial cooling, however, imposes a non-zero value on the liquid phase curvature parameter. Comparison of equation (III-22) with equation (III-26) gives

$$C_2 = \frac{H}{2\ell K_\ell} \quad \text{at } \tau = 0 \quad , \quad \text{(III-49)}$$

or in terms of the non-dimensional parameter,

$$v = \frac{1}{2} \quad \text{at } \tau = 0 \quad . \quad \text{(III-50)}$$

Equations (III-37) - (III-39), (III-44) and (III-46)

form a complete set of ordinary differential equations and coupling conditions. These equations were integrated numerically on a digital computer using a fourth-order Runge-Kutta integration routine to obtain  $\sigma$ ,  $v$ ,  $w$  and  $\tilde{T}$  as functions of time. Details of the numerical method are given in Appendix I.

### III-D RESULTS AND DISCUSSION

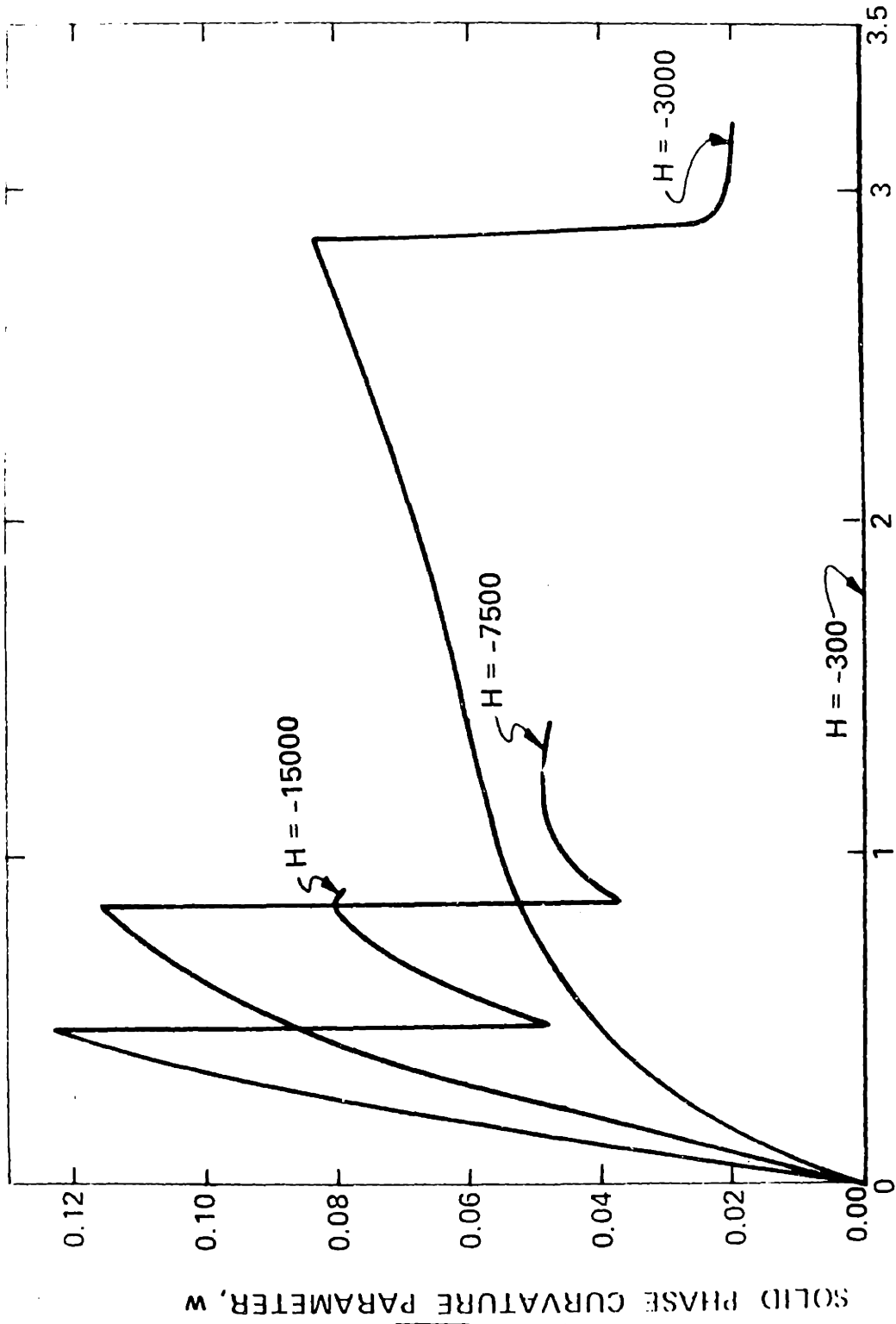
The physical properties used for the planar solidification of an aqueous NaCl solution are listed in Table (III-2). The parameters that may be specified are the initial concentration, and the heat flux  $H$ . The free field concentration was assumed to be 145 moles/m<sup>3</sup> (isotonic) while several values of heat flux were used ranging from -300 to -15,000 (watts/m<sup>2</sup>).

Variation of the solid phase curvature parameter is shown in Figure (III-4). When the solid phase has just started to form, the curvature should be small since there is little thermal mass. The liberation of the latent heat of fusion at  $x = s$ , requires a large heat flux in the solid and magnifies the importance of its growing thermal mass.

The rapid depression of the interface temperature with time is shown in Figure (III-5). Initially the interface temperature is relatively constant, reflecting its slow rate of

Density of Solid	$\rho_s$	57.0 lbm/ft <sup>3</sup>	911.8 K <sub>s</sub> /m <sup>3</sup>
Density of Liquid	$\rho_\ell$	62.4 lbm/ft <sup>3</sup>	998.2 k <sub>s</sub> /m <sup>3</sup>
Thermal Conductivity of Solid	$K_s$	1.28 $\frac{\text{BTU}}{\text{hr-ft-}^\circ\text{R}}$	2.21 $\frac{\text{N-m}}{\text{s-m-K}}$
Thermal Conductivity of Liquid	$K_\ell$	0.319 $\frac{\text{BTU}}{\text{hr-ft-}^\circ\text{R}}$	0.588 $\frac{\text{N-m}}{\text{s-m-k}}$
Thermal Diffusivity of Solid	$D_s$	0.048 ft <sup>2</sup> /hr	1.26 x 10 <sup>-6</sup> $\frac{\text{m}^2}{\text{s}}$
Thermal Diffusivity of Liquid	$D_\ell$	0.00507 ft <sup>2</sup> /hr	.133 x 10 <sup>-6</sup> $\frac{\text{m}^2}{\text{s}}$
Length of Freezing Field	$\ell$	0.0164 ft	5 x 10 <sup>-3</sup> m
Latent Heat of Fusion	$L_{\text{HF}}$	143.3 $\frac{\text{BTU}}{\text{lbm}}$	0.3339 $\frac{\text{MN-m}}{\text{kg}}$
Initial Concentration of NaCl	$C_0$	0.145 $\frac{\text{moles}}{\text{litre}}$	145 $\frac{\text{g-mol}}{\text{m}^3}$
Eutectic Concentration of NaCl	$C_{\text{eut}}$	4.763 $\frac{\text{moles}}{\text{litre}}$	4763 $\frac{\text{g-mol}}{\text{m}^3}$

TABLE (III-2) Constants for NaCl Simulation Routine



NON-DIMENSIONAL TIME,  $\tau$

Figure (III-4) Solid Phase Curvature Parameter.

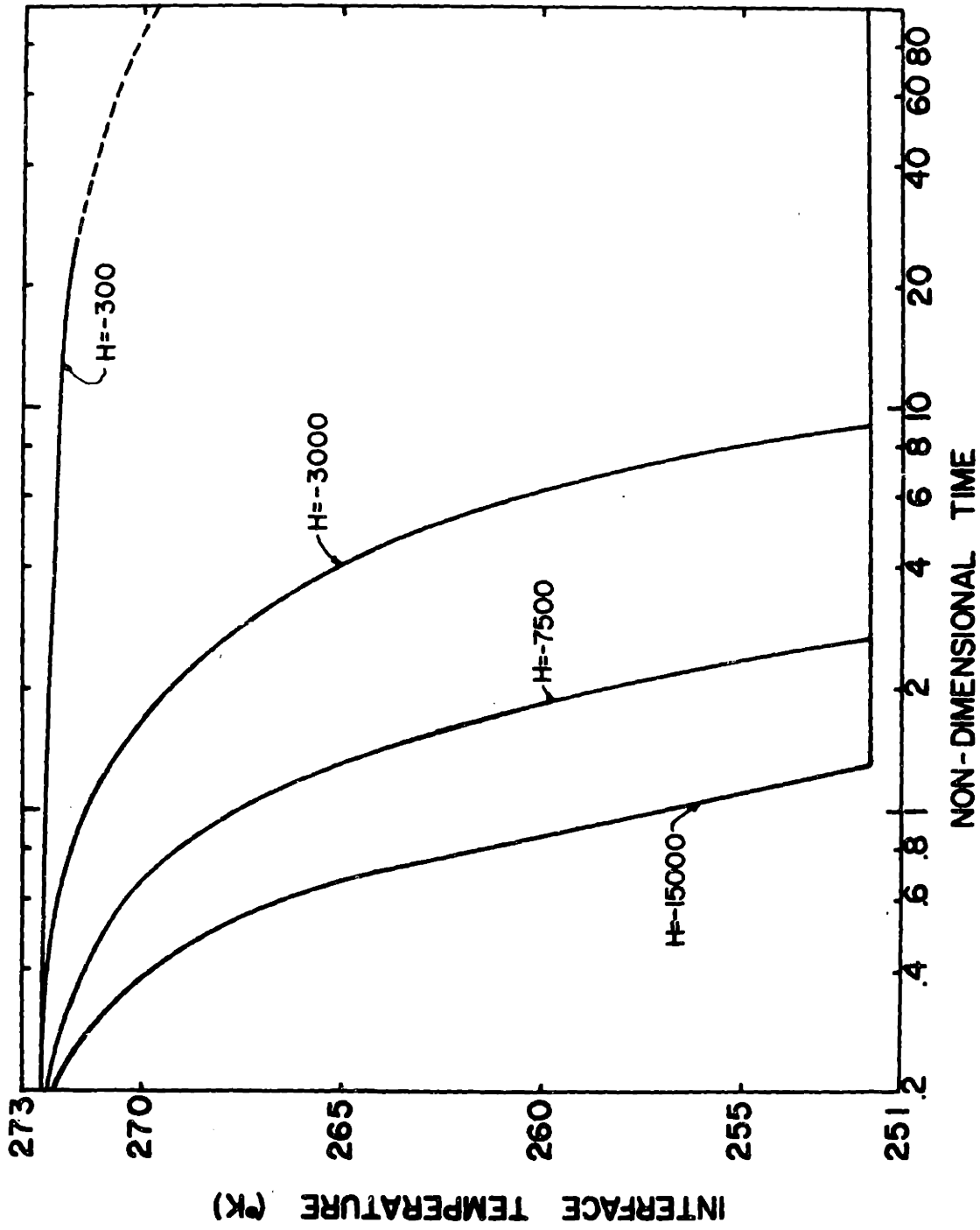


Figure (III-5) Interface Temperature Versus Time.



advance and the weak dependence of equilibrium temperature on concentration at low solute levels. As the interface speed increases, the rate of solute build-up follows, and the dependence of interface temperature on concentration becomes stronger. These effects together produce a very rapid depression of the interface temperature. The sharp rise in the curvature of the temperature profile is due to this depression of the interface temperature and to the growing importance of the thermal mass.

When the interface reaches the eutectic condition, the interface temperature and concentration remain subsequently constant at the eutectic values. This is shown by the horizontal line in Figure (III-5) at 251.86K. This produces a step change in  $\frac{dT}{d\tau}$  from the value corresponding to equation (III-46) to zero. Since the solid-phase curvature equation depends heavily on  $\frac{dT}{d\tau}$ , a discontinuity in one leads to a discontinuity in the other. This is clearly shown in Figure (III-4) for all curves except  $H = -300$  (watts/m<sup>2</sup>) which never reaches the eutectic point. After the sharp drop in the curvature, some "recovery" occurs indicating that the importance of the thermal mass again increases as the interface advances.

The maximum effect of the solid phase curvature parameter on the temperature profile may be calculated by comparing a linear temperature distribution with the parabolic distribution described

by equation (III-25). The maximum is described by

$$\Delta T_{\max} = \text{Max} |T_s(\text{linear}) - T_s(\text{parabolic})| \quad (\text{III-51})$$

where

$$T_s(\text{linear}) = T_{\text{interface}} + \frac{H}{K_s} (s-x) \quad (\text{III-52})$$

and  $T_s(\text{parabolic})$  is given by equation (III-25). Substituting these expressions into equation (III-51) we have,

$$\Delta T_{\max} = \text{Max} |-C_s(s^2-x^2)| \quad (\text{III-53})$$

This extremum occurs at  $x = 0$ , so

$$\Delta T_{\max} = C_s s^2 \quad (\text{III-54})$$

or, in terms of the non-dimensional coordinates  $w$  and  $\sigma$ ,

$$\Delta T_{\max} = \frac{H\ell}{K_s} w\sigma^2 \quad (\text{III-55})$$

The maximum of any case considered is for  $H = -15000$  watts/m<sup>2</sup>, when  $w = 0.1228$  and  $\sigma = 0.286$ . Using these values in equation (III-55) gives  $\Delta T_{\max} = 0.36\text{K}$ . For most purposes, the solid phase curvature may

be neglected.

The liquid phase curvature parameter is plotted against time in Figure (III-6). The initial decrease is due to the "flattening" of the temperature profile in the unfrozen liquid. During this phase, the interface temperature is relatively constant and the thermal energy remaining in the liquid is rapidly being removed. The slight increase in curvature is a result of the interface temperature depression, which changes the boundary condition at  $x = s$ . Since the temperature gradient at  $x = \ell$  must be zero, the curvature must increase.

The sharp discontinuity in all of the curves (except at  $H = - 300 \text{ watts/m}^2$ ) occurs when the eutectic composition is reached at the interface. The curvature prior to this time existed mainly because of the interface temperature depression. When  $\frac{dT}{dt} = 0$ , the temperature profile quickly approaches the constant value of  $T_{eut} = 251.86\text{K}$ . This fact will be important in assessing interface stability in section III-E.

Interface position as a function of time is shown in Figure III-7. Except for a brief transient, the interface speed is constant, validating the assumption made in solving the mass transfer problem. By far, the largest thermal load of the

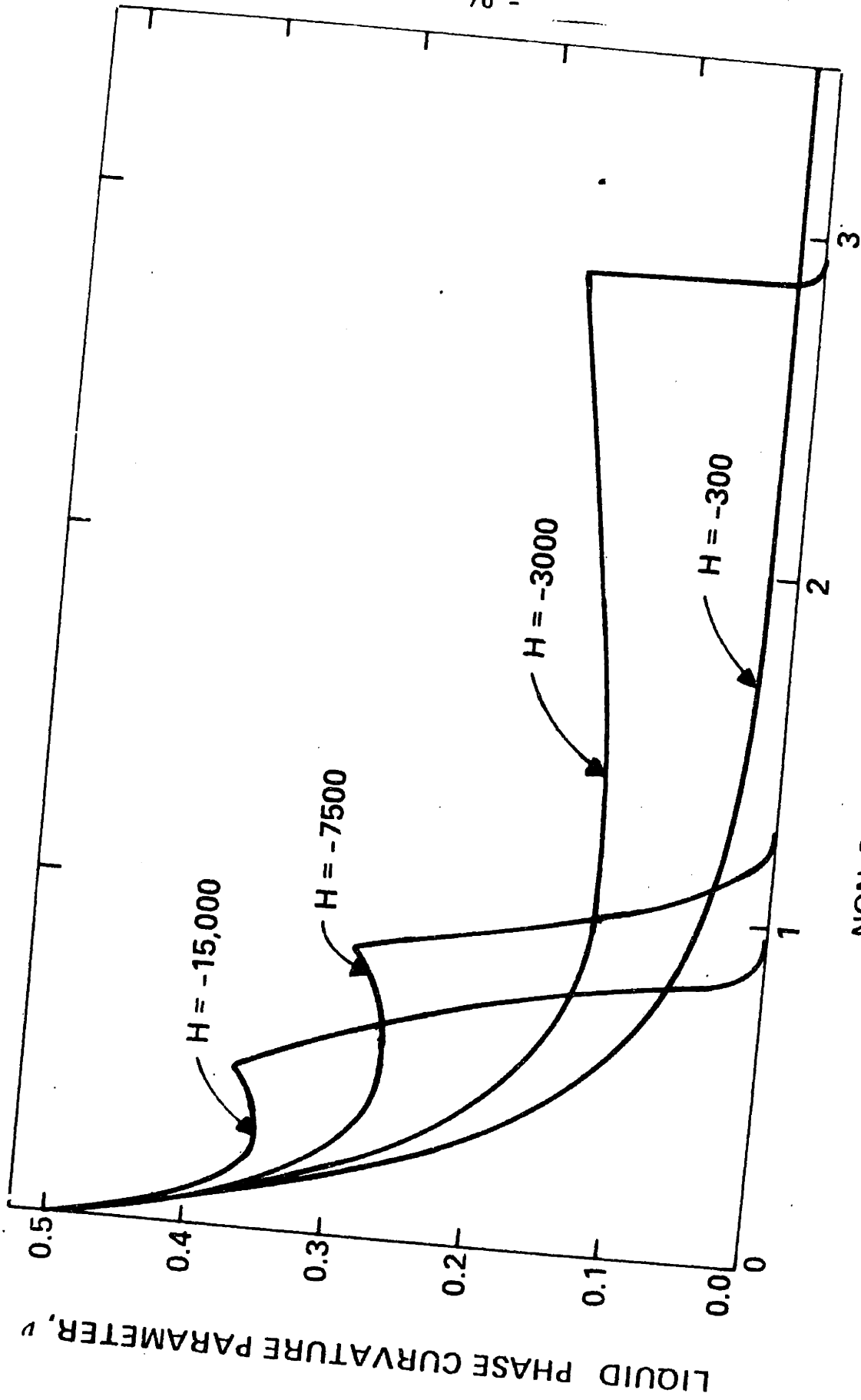


Figure (III-6) Liquid Phase Curvature Parameter.  
NON-DIMENSIONAL TIME  $\tau$

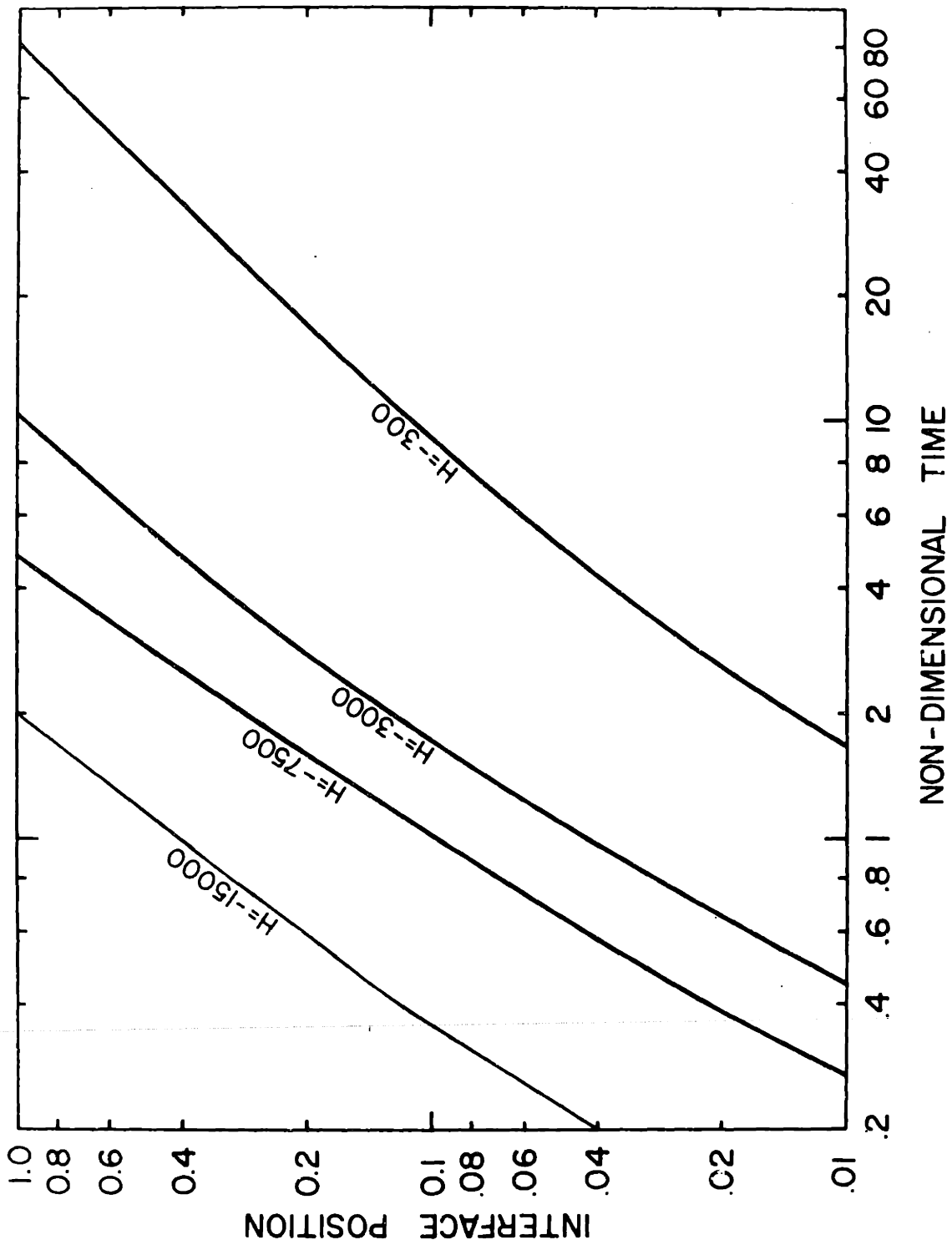


Figure (III-7) Interface Position Versus Time.

system is the liberation of the latent heat of fusion, so most of the heat flux imposed at  $x = 0$  goes to that purpose.

Typical temperature and concentration profiles are shown in Figure III-8 when the interface has just travelled half of the field thickness. The liquid temperature profile is almost completely flat with the centerline temperature only 1.1K higher than the interface temperature. The solid temperature curve is essentially linear. The very steep concentration profile has an interface value of  $3060 \text{ moles/m}^3$  and decreases to 20% of its interface value at a distance of  $.15 \times 10^{-3} \text{ m}$ .

### III-E STABILITY OF THE PLANAR INTERFACE

The original experimental study of the breakdown of a planar freeze front was done by Rutter and Chalmers [31], in which they proposed a criterion which predicted stability of the planar interface shape whenever growth conditions produced a layer of constitutionally supercooled liquid. This theory was subsequently quantified by Tiller, Rutter, Jackson and Chalmers [32]. By predicting the concentration profile in front of a steadily advancing interface, they were able to further predict the amount of constitutional supercooling in the liquid fraction. The theoretical basis for the constitutional supercooling criterion of interface stability is unfortunately rather uncertain.

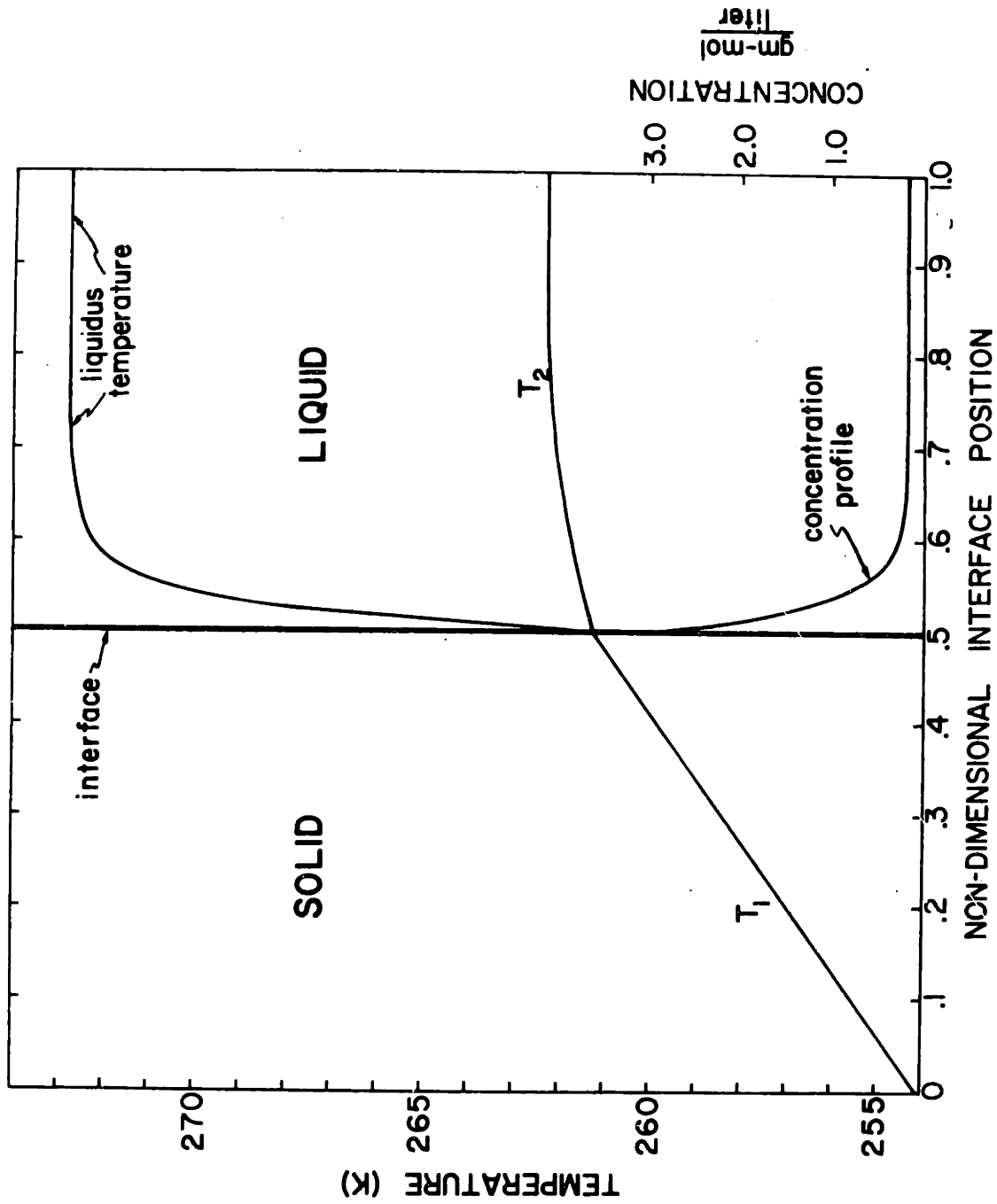


Figure (III-8) Typical Temperature and Concentration Profiles when  $\sigma = 0.5$ ,  $H = -3000$  watts/m<sup>2</sup>.

The most important work on the stability of a planar freeze front was published in a series of papers by Mullins and Sekerka [17, 33, 34]. Their approach was to calculate the time dependence of the amplitude of a sinusoidal perturbation of infinitesimal initial amplitude introduced into the shape of the plane. Since an arbitrary infinitesimal perturbation in the plane may be analyzed into infinitesimal sinusoidal Fourier components, and since all of the relevant equations are linear, the development of the perturbation is simply a superposition of the development of its components. Therefore, the interface is unstable if any sinusoidal wave grows and stable if none grows.

The Mullins-Sekerka stability criterion may be stated mathematically as

$$-\frac{1}{2}(g_{\ell} + g_s) + mG_c < h \quad (\text{III-56})$$

where

$$h = |\text{maximum of } f(\omega)| \quad (\text{III-57})$$

$$f(\omega) = -T_m \Gamma \omega^2 + mG_c \left[ \left\{ \frac{\omega^* - \frac{R}{D}}{\omega^* - \left(\frac{R}{D}\right)P} \right\} - 1 \right] \quad (\text{III-58})$$

$$\omega^* = \left[ \frac{R}{2D} \right] + \sqrt{\frac{R}{2D} + \omega^2} \quad (\text{III-59})$$

$$g_i = \frac{K_i}{K_s + K_{\ell}} \left[ \frac{dT}{dx} \right]_i$$



and  $P = 1 - K$ .

For the freezing of aqueous binary solutions, no solute will be incorporated into the solid phase. Therefore,  $K \rightarrow 0$ ,  $P \rightarrow 1$  and

$$f(w) = - T_m \Gamma w^2. \quad (\text{III-60})$$

The maximum of this function is zero so the criterion becomes

$$-\frac{1}{2} (g_\ell + g_s) + m G_c < 0 \quad (\text{III-61})$$

for stability. The term  $mG_c$  is the gradient in the liquidus temperature at the interface, so equation (III-61) is a modified constitutional supercooling criterion that takes the temperature gradient in the solid into account.

The M-S criterion consists of three terms: the first term arises from capillarity (negligible in this case), is always positive and, therefore, favors stability; the second term arises from thermal gradients, is positive since  $g_\ell, g_s > 0$  and thus also favors stability; the third term, representing the effect of solute on the equilibrium melting temperature is always negative since  $m$  and  $G_c$  always have the same sign, and, therefore, always favor instability. Overall instability of the interface occurs if there

are any conditions for which the magnitude of the third term exceeds that of the sum of the first two terms, otherwise stability prevails.

The results of the planar interface simulation may now be used to evaluate the stability criterion. The temperature gradients in the solid and liquid at the interface are given by equations (III-25) and (III-26) together with equations (III-29) through (III-31). Making these substitutions, we have

$$g_s = \frac{4H}{K_s + K_l} v(\sigma - 1) \quad (\text{III-62})$$

and

$$g_l = \frac{2H}{K_s + K_l} (2w\sigma - 1) \quad (\text{III-63})$$

The concentration gradient at the interface,  $G_c$ , is given by differentiating equation (III-41) with respect to  $x'$  and evaluating at  $x' = 0$ . However, for the purpose of this calculation, the steady concentration profile, equation (III-45) may be used as a lower bound for the concentration gradient (most stable).

Differentiating (III-45) with respect to  $x'$ , we have

$$\frac{dC}{dx'} (x'=0) = - (C_{eut} - C_0) \left( \frac{R}{D_m} \right) \quad (\text{III-64})$$

Using equations (30) and (33)

$$\frac{dC_s}{dx} = - \frac{D_\ell}{D_m \ell} (C_{eut} - C_0) \frac{d\sigma}{d\tau} \quad (III-65)$$

The inverse of equation (III-13) is the concentration as a cubic function of absolute temperature and is given by

$$C_E = a'' + b'' T_E + c'' T_E^2 + d'' T_E^3 \quad (III-66)$$

The local slope of the equilibrium curve,  $m$ , is given by differentiating equation III-66 which gives

$$m = b'' + 2c'' T_E + 3d'' T_E^2 \quad (III-67)$$

Substituting into equation (III-61), we have

$$- \frac{D_\ell (K_s + K_\ell) (C_{ent} - C_0)}{H D_m \ell} \frac{(b'' + 2c'' T_i + 3d'' T_i^2)}{(2v\sigma - 2v + 2w\sigma - 1)} \frac{d\sigma}{d\tau} < 1 \quad (III-68)$$

after some rearranging:

A plot of equation (III-68) is shown in Figure (III-9) for several values of  $H$ , using  $v$  and  $w$  from the simulation of equations (III-37) - (III-39). Since the interface initially has zero velocity, by equation (III-68), it is also stable. However,

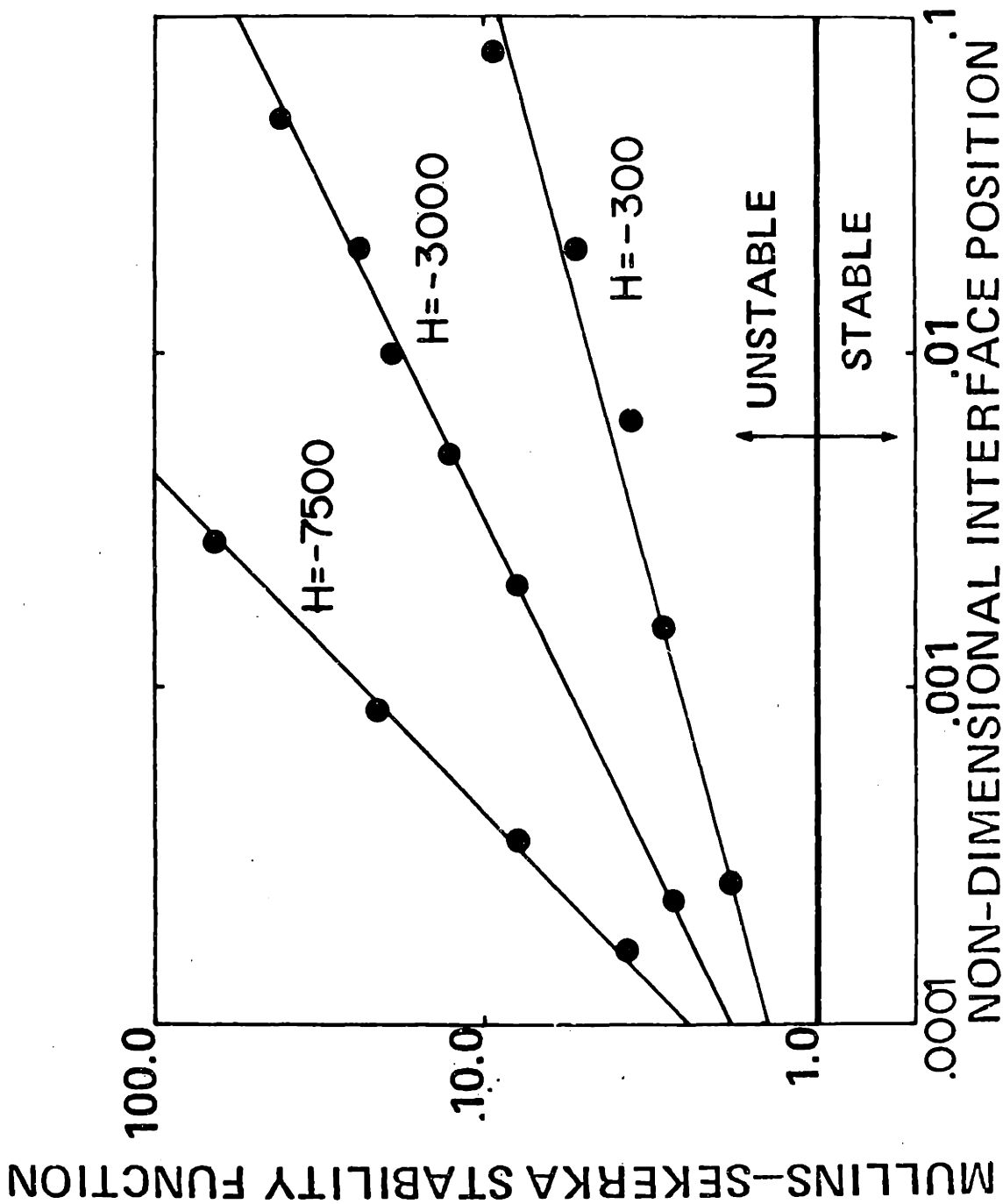


Figure (III-9) Mullins - Sekerka Stability Function Versus Interface Position.

when any appreciable interface displacement or velocity is attained, the stability function substantially exceeds 1.0, indicating the tendency towards transition to higher order interface configuration (e.g., dendritic) which is more stable.

CHAPTER IV HEAT AND MASS TRANSPORT DURING  
DENDRITIC SOLIDIFICATION

IV.A Introduction

IV.A.1 Formation of Dendrites

There is a tendency for dendritic growth whenever the M-S criterion is positive (Eq. (III-68) and increases with time. In a pure melt, the dendritic morphology can develop into the major growth morphology only if the gradient of temperature in the liquid is negative at the interface (decreasing into the melt). For alloy liquids, it is possible to develop the dendritic morphology with a positive temperature gradient provided the solute distribution is such that the gradient in concentration at the interface is greater than the "weighted" heat fluxes in the liquid and solid at the interface. The main characteristic of the solid that forms when the temperature gradient in the liquid at the interface is negative is that it possesses a tree-like growth form, having a trunk and branches of different order extending in unique directions relative to the crystallographic form of the material. In the case of the positive temperature gradient, one seldom observes branches on the dendrite trunk or any unique crystallographic direction for the dendrite axis.

It was shown in Chapter III that saline solutions tend to freeze dendritically. We will examine the thermal driving force that must be imposed for dendritic solidification at various rates and for several free-field conditions. The temperature and concentration fields will be determined for application to the cellular dehydration model developed in Chapter V.

#### IV.A.2 Problem Statement

A quantitative description of the characteristics of dendritic solidification may only be developed if several simplifications are made. Several additional assumptions are necessary in order to make the problem at all tractable. These simplifications must be relaxed in the application of this theory to real dendrites. However, in this treatment, the following restrictions will apply:

1. The growth of the dendrite, its shape and the entire temperature and concentration fields are assumed at steady state. This excludes periodic growth of highly anisotropic materials such as long-chain polymers.
2. The primary dendrite cores are assumed rotationally symmetric. This also excludes highly anisotropic materials, but all aqueous solutions experimentally exhibit symmetric dendrites.

3. The material properties and the interface speed are assumed constant. The planar freezing analysis showed a nearly constant interface speed during most of the freezing protocol. The assumption of constant material properties is commensurate with the level of sophistication of this analysis.
4. Natural convection is neglected. This factor is present in the liquid because of the different densities of the liquid and solid phases, which gives rise to a convective velocity  $U$  at the interface. The interface moves at constant velocity  $R$ ; hence, the mass solidified per unit surface area per unit time is  $\rho_s R$ . The net velocity at the interface is  $R-U$  and this causes a mass flow per unit area per unit time of  $\rho_l (R-U)$ . Equating mass flows gives

$$U = -\epsilon R$$

$$\text{where } \epsilon = \frac{\rho_l - \rho_s}{\rho_l}$$

Chambre [35] has shown that unless  $\epsilon$  is near unity, the temperature and concentration fields are unaffected. For the present case  $\epsilon=0.09$ .



5. Dendrites are evenly spaced in a hexagonal, close packed array.

Consider the rotationally symmetric primary dendrite cores shown in Fig. II-5. The exact differential equations for heat and solute transport to be solved for steady state growth are:

$$\nabla^2 T + \frac{R}{D_s} \frac{\partial T}{\partial z} = 0 \quad (\text{solid region}) \quad (\text{IV-1})$$

$$\nabla^2 T + \frac{R}{D_l} \frac{\partial T}{\partial z} = 0 \quad (\text{liquid region}) \quad (\text{IV-2})$$

$$\nabla^2 C_s + \frac{R}{D_m} \frac{\partial C_s}{\partial z} = 0 \quad (\text{liquid region}) \quad (\text{IV-3})$$

The coordinate system used for these equations is the circular cylinder coordinate system with its origin at the dendrite base and the  $z$  axis coincident with the dendrite axis.

The boundary conditions for energy and mass conservation are derived as follows. The mass transfer boundary condition states that solutes must be completely rejected from the solid phase. The absolute velocity of a solute particle in the direction normal to the dendrite surface ( $\vec{n}$  direction, see Fig. (IV-1)) is given by:

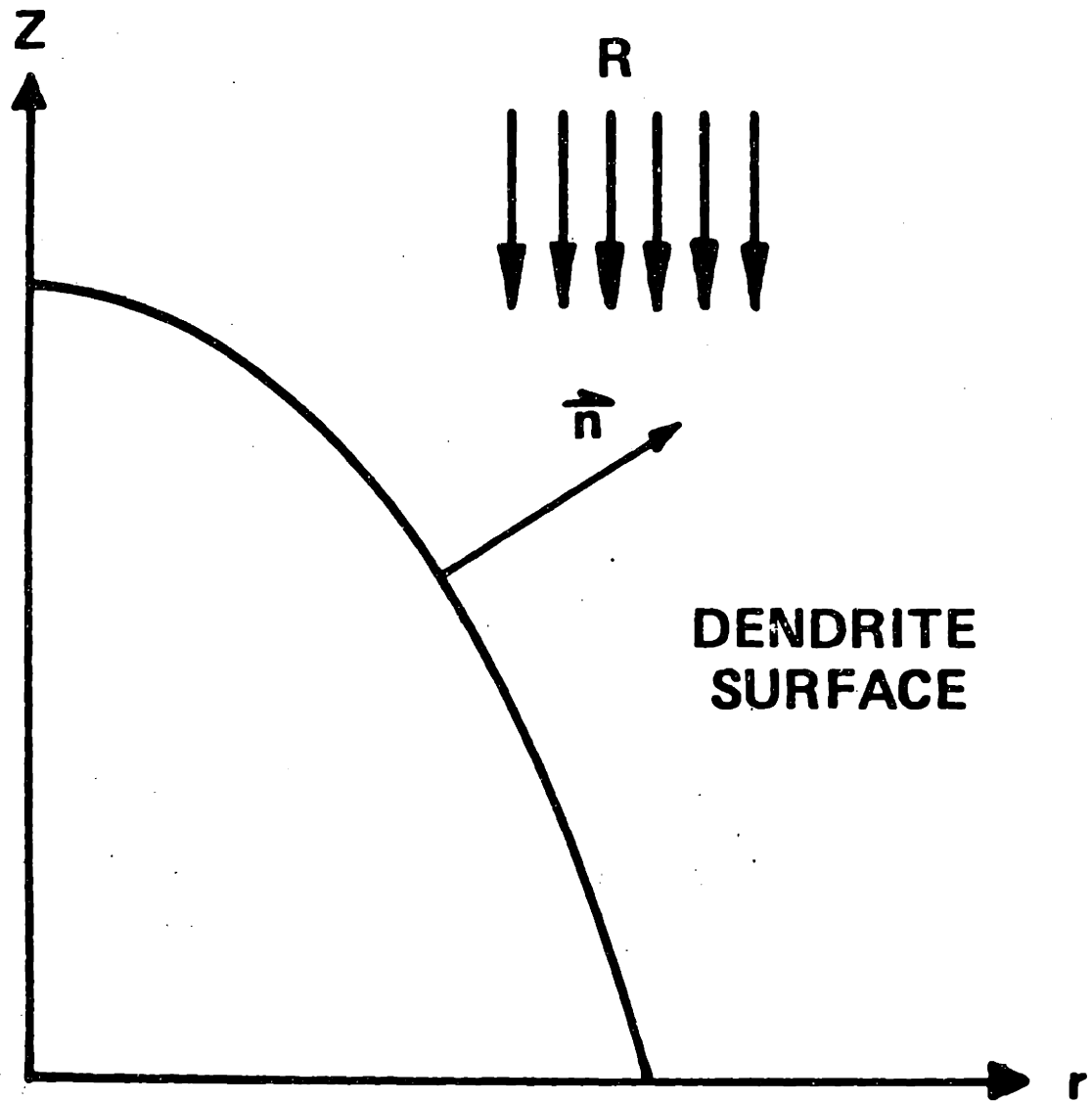


Figure (IV-1) Diagram of Normal Vector to the Dendrite Surface.

$$V_p = R C_s(\text{surface}) \vec{k} \cdot \vec{n} + D_m \frac{\partial C_s}{\partial n}$$

where  $\vec{k}$  is the unit vector in the z direction. By conservation of mass, this normal absolute velocity must vanish at the dendrite surface. Using  $\frac{dC_s}{dn} = \nabla C_s \cdot \vec{n}$ , we have

$$\left(\frac{R}{D_m} C_s(\text{surface}) \vec{k} + \nabla C_s\right) \cdot \vec{n} = 0 \quad . \quad (\text{IV-5})$$

Now

$$\vec{n} = \frac{\vec{i} - \left(\frac{\partial r_s}{\partial z}\right) \vec{k}}{\sqrt{1 + \left(\frac{\partial r_s}{\partial z}\right)^2}} \quad (\text{IV-6})$$

where  $\vec{i}$  = the unit vector in the radial direction and  $r_s = r_s(z)$  describes the surface of the dendrite. Substituting equation (IV-6) into equation (IV-5) and taking the dot products, we have

$$\frac{R}{D_m} C_s + \frac{\partial C_s}{\partial r} - \frac{\partial C_s}{\partial z} \frac{\partial r_s}{\partial z} = 0 \quad . \quad (\text{IV-7})$$

The thermal boundary condition results from an energy balance applied at the dendrite surface and is given by

$$[K_s (\nabla T)_s - K_l (\nabla T)_l] \cdot \vec{n} = \rho_s L_{HF} R \vec{k} \cdot \vec{n} \quad . \quad (\text{IV-8})$$

This equation states that the net rate of heat conduction from

the control volume removes the latent heat of fusion generated during solidification. It also implies that there is a discontinuity in the heat flux at the interface. Using equation (IV-6) in equation (IV-8) gives

$$K_s \left[ \frac{\partial T}{\partial r} \right]_s - K_l \left[ \frac{\partial T}{\partial r} \right]_l + \{ K_l \left[ \frac{\partial T}{\partial z} \right]_l - K_s \left[ \frac{\partial T}{\partial z} \right]_s + \rho_s R L_{HF} \} \frac{dr_s}{dz} = 0. \quad (IV-9)$$

The differential equations and boundary conditions together with the necessary symmetry conditions are shown in Figure IV-2.

#### IV.A.3 Optimization Condition

Bolling and Tiller [36] investigated the problem outlined above and concluded that it is not completely specified. Their claim is that the problem may be solved only to within one unknown, such as the basal heat flux or the tip curvature. This conclusion was also reached by two earlier investigators, Kirkaldy [37] and Zener [38].

To complete the problem statement an additional condition must be specified. The condition could be a thermodynamic optimization condition, similar to the minimization of the Gibbs free energy in an equilibrium situation. Some of the classically used criteria in this steady-state non-equilibrium problem are:

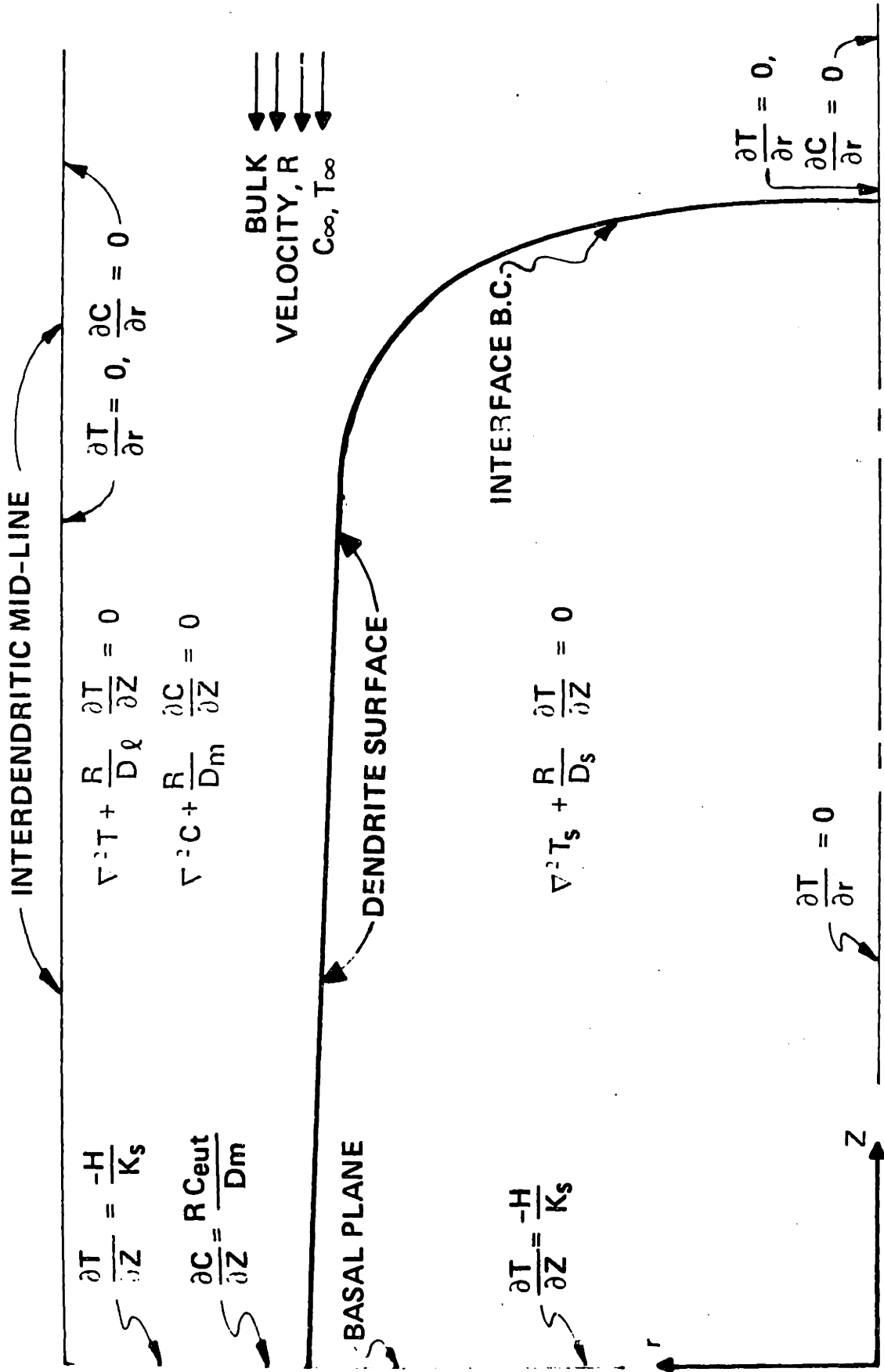


Figure (IV-2) Summary of Exact Differential Equations and Boundary Conditions for Dendritic Solidification.

- (1) minimum rate of entropy production. One would expect that this condition should derive from irreversible thermodynamics, but no one has been able to prove this condition for growth processes.
- (2) maximum linear velocity of phase transportation. This criterion was used without justification.
- (3) maximum volume of phase transition per unit time. Also used without justification.

The optimization criterion used in the present case is "thermodynamic stability of the dendrite tip". Its derivation and justification are given in section IV-D.

#### IV.A.4 Previous Research

Published solutions to dendritic solidification problems are restrictions of the general problem stated above. Temkin [39] did an elegant mathematical analysis of needle-shaped crystal growth. The analysis is parallel in reasoning to the non-isothermal dendrite case performed by Bolling and Tiller [36]. Billing [40] analyzed dendrite "extraction" at constant rate. In this process a seeded crystal is physically removed from the melt as it forms. The exposed crystal shank is cooled with water to remove the heat of

solidification. Finally, Ivantsov [41] assumed that the dendrite tip was described by a paraboloid of revolution and gave an exact solution for that case. That solution showed that a paraboloidal dendrite tip was both an isotherm and an isoconcentrate, and that all isotherms and isoconcentrates were mathematically similar in shape. This conclusion will be used extensively in section IV-C. In none of these investigations has the entire dendritic solidification problem been solved, even approximately.

#### IV.A.5 Two-zone Freezing Model

The loci of constant temperature in the vicinity of a growing dendrite are shown in Figure IV-3. Deep within the interdendritic space, the transport of heat will mostly be the axial direction, with nearly planar isotherms. This is largely due to the fact that the dendrite cross-sectional area is changing very little with axial distance, and very little solidification is taking place. The dendrite tip resembles a paraboloid of revolution as discussed by Ivantsov [41], and the adjacent isotherms have the same shape.

The two distinct characteristics of the isotherms suggest that the problem may be simplified by considering two separate zones. The first is the "planar isotherm" zone and extends from the basal plane forward to the boundary shown in Figure IV-3. The other zone ranges from the dendrite tip forward to infinity and is bounded

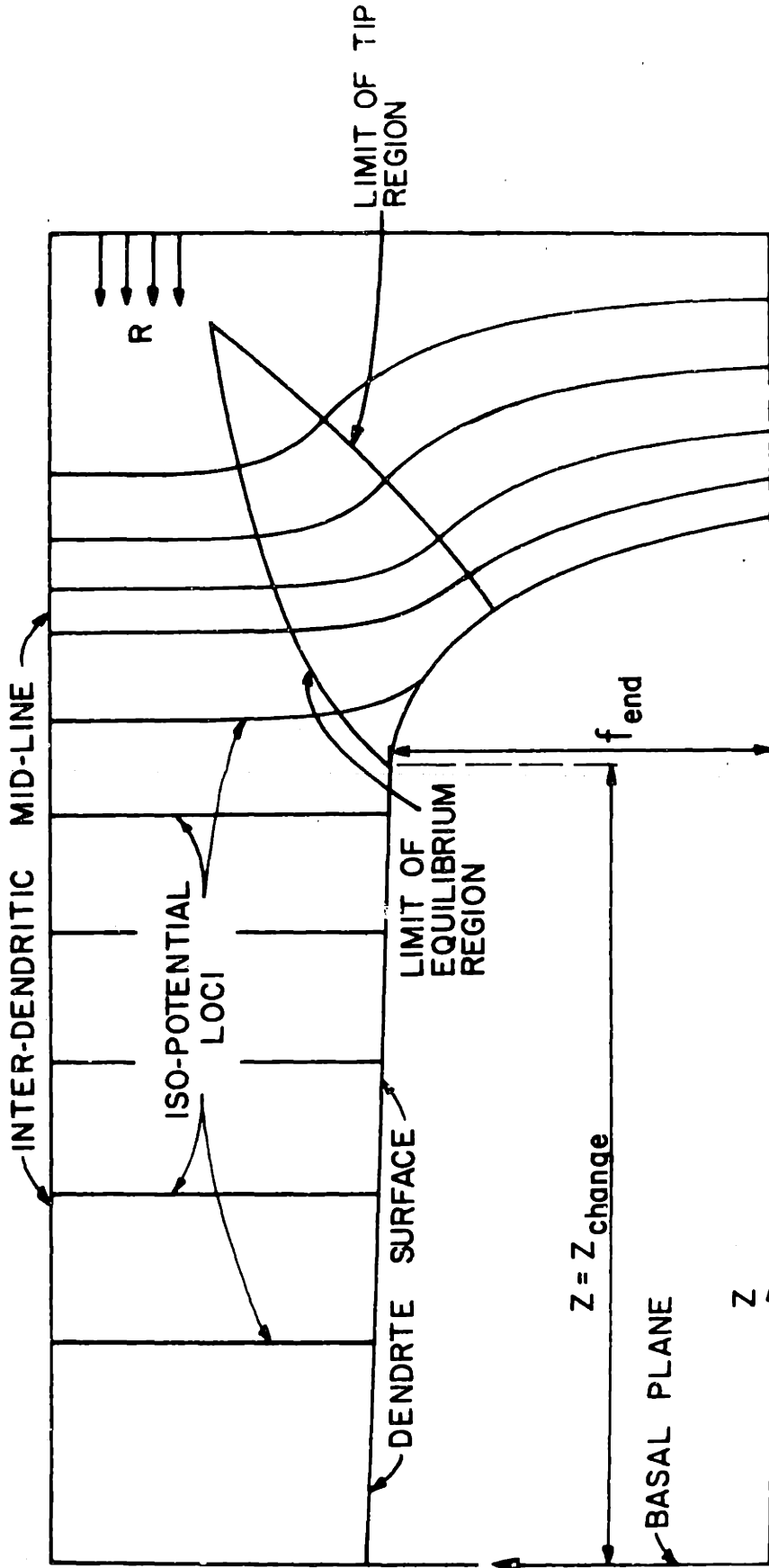


Figure (IV-3) Approximate Isotherms During Dendritic Solidification.



on either side as shown in the figure. The "no solution" zone will not be treated in this work, but its effect will be shown to be negligible.

The temperature and concentration fields in neither of the two zones may be solved for independently. Instead, families of solutions will be generated in each region and then matching and optimization conditions will be employed to choose a particular solution from each family that is compatible and satisfies the overall boundary conditions. These matching and optimization conditions include:

- (1) Thermodynamic stability of the dendrite tips (optimization condition),
- (2) Geometric "matching" of the dendrite shape profiles at the point of transition from one solution region to another, and
- (3) Thermal "matching" of the temperature and heat flux at the point of transition.

#### IV.B. THE EQUILIBRIUM ZONE

In addition to the assumptions listed in the previous section, three other restrictions apply:

- (1) As was discussed above, the isotherms and isoconcentrates are planar, perpendicular to the growth direction.
- (2) The dendrite spacing adjusts itself so that the interdendritic constitutional supercooling disappears. Since the thermal gradients in the direction normal to the dendrite surface are nearly zero, the stability criterion, equation (III-61), implies that the normal concentration gradient must also be nearly zero. Therefore, this restriction requires the isoconcentrates to be planar as well as the isotherms and the loci illustrated in Figure IV-3 are isoconcentrates as well as isotherms. This assumption also forms a criterion for predicting the dendrite spacing as a function of the free-field concentration and interface speed [50].
- (3) Dendrite size is sufficiently coarse so that the effect of radius of curvature on the melting point may be neglected.

Since the rate of growth of the dendrite is low in the basal region, the solid and the liquid just adjacent to it are at equilibrium. Together with assumption (1), this implies that the liquid in the

zone is everywhere in equilibrium with the solid at the same axial position. This is a result of the small amount of solidification occurring in this region.

#### IV-B.1 Transport Equations

##### IV-B.1a Energy Transport

Consider a planar differential volume element of thickness  $dz$  located at position  $z$ , which extends from the centerline of a dendrite to the midline of the interdendritic space (see Figure (IV-4)). At any position  $z$ , the fraction of the cross-sectional area occupied by solid phase is  $f_s(z)$ , and the remaining fraction occupied by liquid is  $f_l(z) = 1 - f_s(z)$ . This fraction is different at the positions  $z$  and at  $z + dz$  by the amount

$$df_s = f_s(z+dz) - f_s(z) . \quad (IV-10)$$

The first law of thermodynamics applied to this control volume has three contributions: heat transfer by conduction, heat transfer by mass motion (convection) and heat generation due to solidification. The net heat transfer by conduction is found by summing the input and output terms for the liquid and solid fraction as follows:

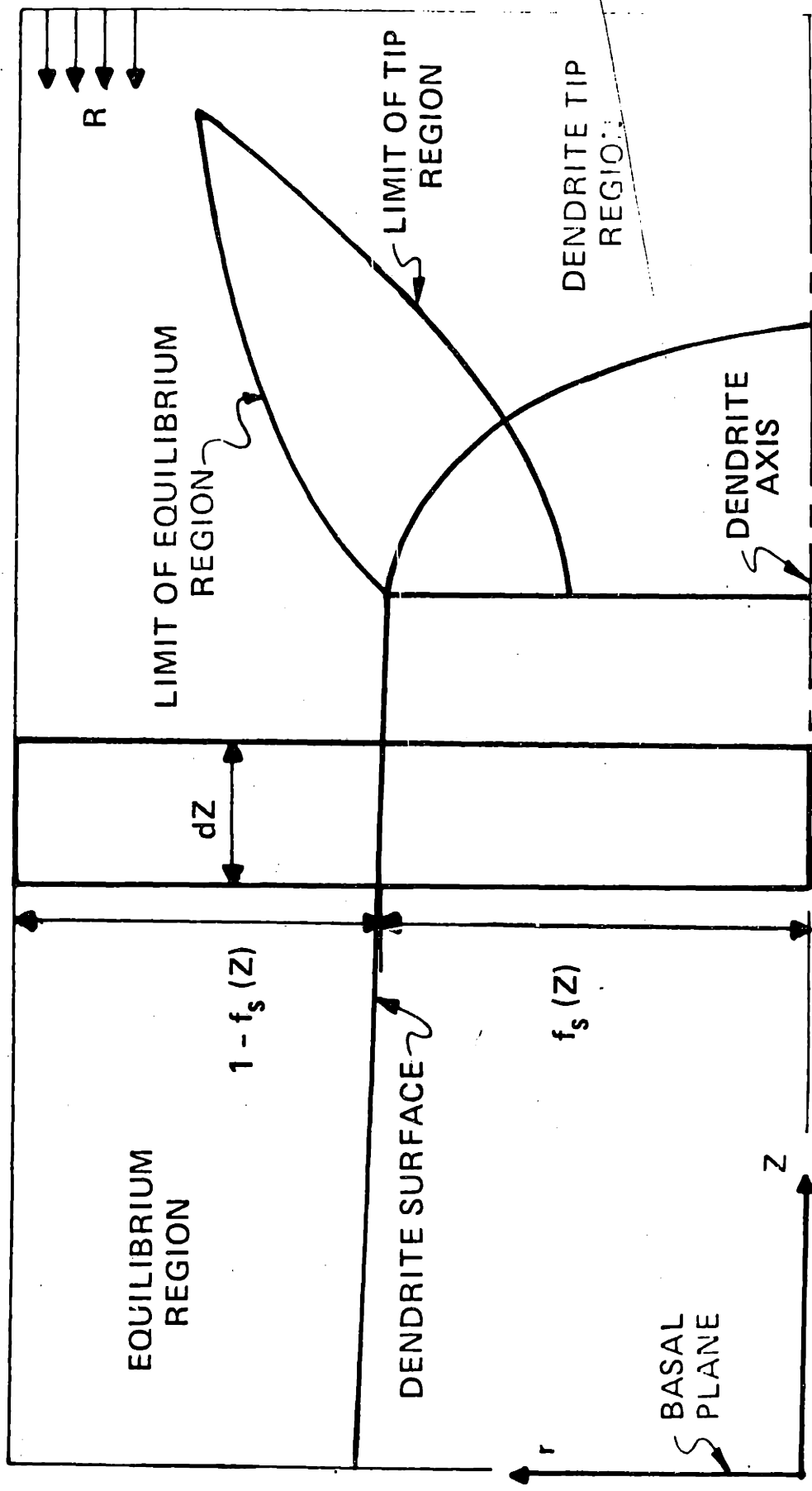


Figure (IV-4) Dendritic Freezing Geometry.

$$\begin{aligned} \dot{q}_{\text{conduction}} &= K_s f_s(z+dz) \frac{\partial T}{\partial z}(z+dz) + K_l f_l(z+dz) \frac{\partial T}{\partial z}(z+dz) \\ &- K_s f_s(z) \frac{\partial T}{\partial z}(z) - K_l f_l(z) \frac{\partial T}{\partial z}(z). \end{aligned} \quad (\text{IV-11})$$

The net convective heat flux is given by

$$\begin{aligned} \dot{q}_{\text{convection}} &= R \rho_s C_s f_s(z+dz) (T(z+dz) - T(z)) + R \rho_l C_l f_l(z) (T(z+dz) - T(z)) \\ &- R \rho_l C_l (T(z+dz) - \frac{T(z+dz) + T(z)}{2}) \\ &+ \rho_s C_s (\frac{T(z+dz) + T(z)}{2} - T(z)) df_s. \end{aligned} \quad (\text{IV-12})$$

The first two terms in equation (IV-12) are equivalent to:

$$\begin{aligned} &R \rho_s C_s \{ f_s(z+dz) T(z+dz) - f_s(z) T(z) \} \\ &+ R \rho_l C_l \{ T(z+dz) f_l(z+dz) - T(z) f_l(z) \} \\ &+ R \{ \rho_l C_l T(z+dz) - \rho_s C_s T(z) \} df_s. \end{aligned} \quad (\text{IV-13})$$

Substituting this expression into equation (IV-12), we obtain

$$\begin{aligned} \dot{q}_{\text{convection}} = & R\rho_S C_S \left\{ f_S(z+dz) T(z+dz) - f_S(z) T(z) \right\} \\ & + R\rho_L C_L \left\{ T(z+dz) f_L(z+dz) - T(z) f_L(z) \right\} \quad (\text{IV-14}) \\ & - R(\rho_S C_S - \rho_L C_L) \left\{ \frac{T(z+dz) + T(z)}{2} \right\} df_S . \end{aligned}$$

The rate of heat generation is the rate at which material is being solidified times the latent heat of fusion per unit volume, and is given by

$$\dot{q}_{\text{generation}} = R(f_S(z+dz) - f_S(z)) \rho_S L_{\text{HF}} \quad (\text{IV-15})$$

In the steady-state, the net rate of energy transfer into the control volume must be zero. Adding equations (IV-11), (IV-14) and (IV-15) we have

$$\begin{aligned} & K_S \left\{ f_S(z+dz) \frac{dT}{dz}(z+dz) - f_S(z) \frac{dT}{dz}(z) \right\} \\ & + K_L \left\{ f_L(z+dz) \frac{dT}{dz}(z+dz) - f_L(z) \frac{dT}{dz}(z) \right\} \\ & + R\rho_S C_S \left\{ f_S(z+dz) T(z+dz) - f_S(z) T(z) \right\} \quad (\text{IV-16}) \\ & + R\rho_L C_L \left\{ f_L(z+dz) T(z+dz) - f_L(z) T(z) \right\} \\ & - R(\rho_S C_S - \rho_L C_L) \frac{T(z+dz) + T(z)}{2} + \rho_S L_{\text{HF}} (f_S(z+dz) - f_S(z)) = 0. \end{aligned}$$

Dividing by  $dz$ , taking the limit at  $dz \rightarrow 0$ , and using the definition of the derivative, we obtain

$$K_s \frac{d}{dz} (f_s \frac{dT}{dz}) + K_\ell \frac{d}{dz} (f_\ell \frac{dT}{dz}) + R \rho_s C_s \frac{d}{dz} (f_s T) + R \rho_\ell C_\ell \frac{d}{dz} (f_\ell T) - R (\rho_s C_s - \rho_\ell C_\ell) T + \rho_s L_{HF} \frac{df_s}{dz} = 0 \quad . \quad (IV-17)$$

Taking the derivatives of the products and using  $f_\ell = 1 - f_s$ , we have

$$\left[ K_s f_s + K_\ell (1-f_s) \right] T'' + \left[ (K_s - K_\ell) f_s' + R \rho_s C_s f_s + R \rho_\ell C_\ell (1-f_s) \right] T' - R \rho_s L_{HF} f_s' = 0 \quad . \quad (IV-18)$$

This equation provides a relationship between the temperature field and the dendrite shape,  $f_s(z)$ .

#### IV-B.1b Mass Transport

Since solute is completely rejected from the solid phase, diffusion and convection of solute occur only in the liquid. The net diffusive mass flux is given by

$$w_{\text{diffusion}} = D_m f_\ell(z+dz) \frac{\partial C_S}{\partial z}(z+dz) - D_m f_\ell(z) \frac{\partial C_S}{\partial z}(z) \quad . \quad (\text{IV-19})$$

The net convective mass flux is given by an expression similar to equation (IV-12):

$$w_{\text{convection}} = R f_\ell(z+dz) C_S(z+dz) - R f_\ell(z) C_S(z) \quad . \quad (\text{IV-20})$$

In the steady-state the net accumulation of mass in the control volume must be zero. Summing equations (IV-19) and (IV-20), we have

$$D_m (f_\ell(z+dz) \frac{\partial C_S}{\partial z}(z+dz) - f_\ell(z) \frac{\partial C_S}{\partial z}(z)) \quad (\text{IV-21})$$

$$+ R (f_\ell(z+dz) C_S(z+dz) - f_\ell(z) C_S(z)) = 0 \quad .$$

Dividing by  $dz$  and the taking the limit as  $dz \rightarrow 0$  gives

$$D_m f_\ell C_S'' + (D_m f_\ell' + R f_\ell) C_S' + (R f_\ell') C_S = 0 \quad . \quad (\text{IV-22})$$

Using  $f_\ell = 1 - f_s$ , equation (IV-22) becomes

$$D_m (1-f_s) C_S'' + (R(1-f_s) - D_m f_s') C_S' - (R f_s') C_S = 0. \quad (\text{IV-23})$$

Since the liquid and solid at any axial position are at



thermodynamic equilibrium, the temperature-concentration relationship is given by equation (II-13),

$$T_E = a' + b'C_E + c'C_E^2 + d'C_E^3 \quad . \quad (II-13)$$

Equations (II-13), (IV-18) and (IV-23) form a nonlinear system of three equations in  $T(z)$ ,  $C_s(z)$  and  $f_s(z)$ . The system may be solved by transforming either (IV-18) or (IV-23) into an equation in concentration or temperature respectively, using equation (III-13). Since the temperature field is of primary interest, equation (IV-23) is transformed to an equation in temperature. Using the chain rule we have

$$\frac{dC_s}{dz} = C'_s = \left[ \frac{\partial C_s}{\partial T} \right]_E \frac{\partial T}{\partial z} \quad (IV-24)$$

and

$$\frac{d^2C_s}{dz^2} = C''_s = \left[ \frac{\partial^2 C_s}{\partial T^2} \right]_E (T')^2 + \left[ \frac{\partial C_s}{\partial T} \right]_E T'' \quad . \quad (IV-25)$$

The derivatives  $\left[ \frac{\partial C}{\partial T} \right]_E$  and  $\left[ \frac{\partial^2 C}{\partial T^2} \right]_E$  may be evaluated using equation (III-66) as follows:

$$\left[ \frac{\partial C}{\partial T} \right]_E = b'' + 2c''T + 3d''T^2 \quad (IV-26)$$

and

$$\left[ \frac{\partial^2 C_s}{\partial T^2} \right]_E = 2c'' + 6d''T \quad (IV-27)$$

Finally, substituting equations (IV-24) and (IV-27) into equation (IV-23), we have

$$\begin{aligned} & (1-f_s) \{ 2c'' + 6d''(T)(T')^2 + (b'' + 2c''T + 3d''T^2)T'' \} \\ & - (R(1-f_s) - D_m f'_s) (b'' + 2c''T + 3d''T^2) T' \\ & - R f'_s (a'' + b''T + c''T^2 + d''T^3) = 0 \quad (IV-28) \end{aligned}$$

#### IV-B.2 Non-Dimensional Equations

Equations (IV-18) and (IV-28) may be made axially non-dimensional by using the transformation:

$$z^* = \frac{z}{L^*} \quad (IV-29)$$

where

$$L^* = \frac{K_S - K_L}{R(\rho_L C_L - \rho_S C_S)} \quad (IV-30)$$

Transforming equation (IV-18) to the  $z^*$  coordinate system we have,

$$\left[ (f_S + \frac{k_L}{k_S - k_L}) \frac{d^2 T}{dz^{*2}} + \left[ \frac{df_S}{dz^*} - f_S - \frac{\rho_L C_L}{(\rho_S C_S - \rho_L C_L)} \right] \frac{dT}{dz^*} + \left[ \frac{\rho_S L_f}{(\rho_S C_S - \rho_L C_L)} \right] \frac{df_S}{dz^*} \right] = 0. \quad (IV-31)$$

Similarly transforming the mass transfer equation yields

$$\frac{d^2 T}{dz^{*2}} + \frac{\frac{\partial^2 C_S}{\partial T^2}}{\frac{\partial C_S}{\partial T}} \left( \frac{dT}{dz^*} \right)^2 + \frac{(K_S - K_L)}{D_m (\rho_L C_L - \rho_S C_S)} \frac{dT}{dz^*} - \frac{1}{(1 - f_S)} \left\{ \frac{dT}{dz^*} + \frac{(K_S - K_L)}{D_m (\rho_L C_L - \rho_S C_S)} \frac{C_S}{\left( \frac{\partial C_S}{\partial T} \right)} \right\} \frac{df_S}{dz^*} = 0 \quad (IV-32)$$

where  $C_S$ ,  $\frac{\partial C_S}{\partial T}$ , and  $\frac{\partial^2 C_S}{\partial T^2}$  are given by equations (III-13), (IV-26) and (IV-27).

The reader should note that the interface speed  $R$  does not appear in either of equations (IV-31) or (IV-32). This parameter is "absorbed" in the non-dimensional independent variable  $z^*$ . Thus, for given free-field conditions,  $(C_\infty, T_\infty)$  the transport fields and dendrite shape are identical for all interface speeds, when described by the axial coordinate  $z^*$ . These fields are said

to be geometrically similar and the variable  $z^*$  is defined as the similarity variable, implying that different interface speeds give results that are geometrically similar. The characteristic length  $L^*$  acts simply as a scaling factor for the length of the dendrite and is inversely proportional to the interface speed.

#### IV.B.3 Boundary Conditions

Simultaneous solution of equations (IV-31) and (IV-32) require three independent boundary conditions,  $T$ ,  $dT/dz^*$  and  $f_s$ , specified at the basal plane. By definition, the basal plane is at the eutectic condition, so

$$T = 251.86K \text{ at } z^* = 0 \quad . \quad (IV-33)$$

Consider a control volume around the entire freezing field as shown in Figure IV-5. Material enters the control volume from the free field at  $T_\infty$  and  $C_\infty$ , and leaves the control volume from the basal plane at conditions  $T_{eut}$  and  $C_{eut}$ . By conservation of mass,

$$RC_\infty = R(1-f_s(z^*=0))C_{eut} \quad (IV-34)$$

since at steady state there can be no accumulation of mass in the control volume. Solving for  $f_s$ , we have

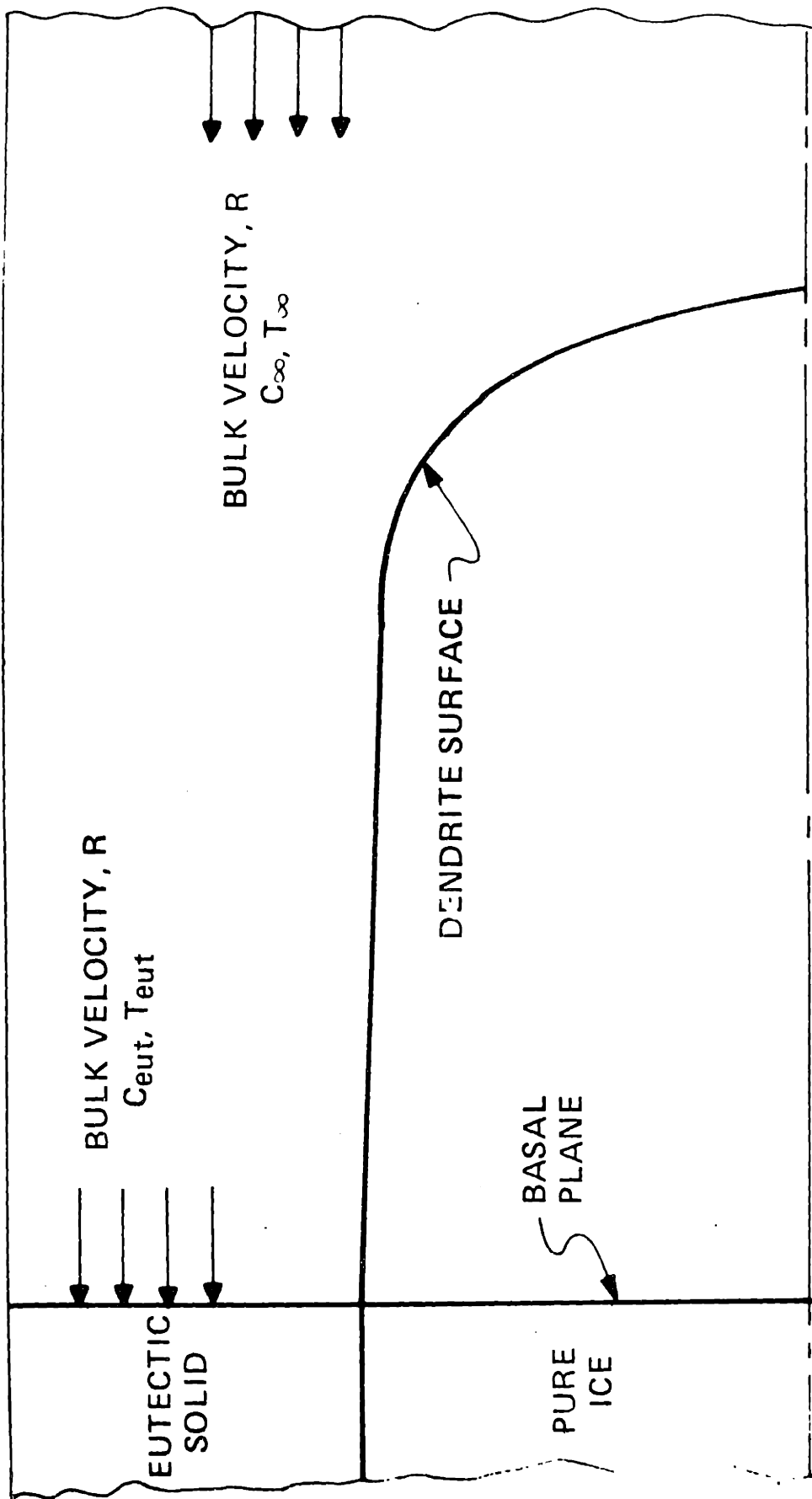


Figure (IV-5) Control Volume for Overall Mass Conservation.

$$f_s = 1 - \frac{C_\infty}{C_{eut}} \quad \text{at } z^* = 0 \quad . \quad (\text{IV-35})$$

The heat flux at the basal plane consists of two components: the heat flux required for solidification and the sensible heat flux needed to change the liquid to the freezing temperature and sub-cool the solid to the eutectic. It is impossible to calculate the sensible flux a priori. Its maximum value may be estimated by assuming that the liquid is supercooled to the eutectic temperature before freezing takes place. This maximum is given by

$$H_{\text{sensible}}^{(\text{maximum})} = R\rho_l C_l (T_\infty - T_{eut}) \quad . \quad (\text{IV-36})$$

The heat flux necessary for solidification is given by

$$H^* = R\rho_s L_{HF} f_s(z^*=0) \quad (\text{IV-37})$$

and is the rate of liberation of latent heat in solidifying the fraction  $f_s$  of the freezing field. Comparing equations (IV-36) and (IV-37) and using the numerical data in Table III-2 shows that the sensible heat flux is at most 25% of the solidification heat flux. A good initial estimate of the basal heat flux is therefore  $H^*$ . Using the Fourier conduction law and equation (IV-29), equation (IV-37) becomes

$$\left(\frac{dT}{dz^*}\right)^* = \frac{\rho_s L_{HF} f_s (K_s - K_l)}{(\rho_l C_l - \rho_s C_s)(k_s f_s + k_l (1 - f_s))} \text{ at } z^* = 0. \quad (\text{IV-38})$$

#### IV-B.4 Equilibrium Region Results

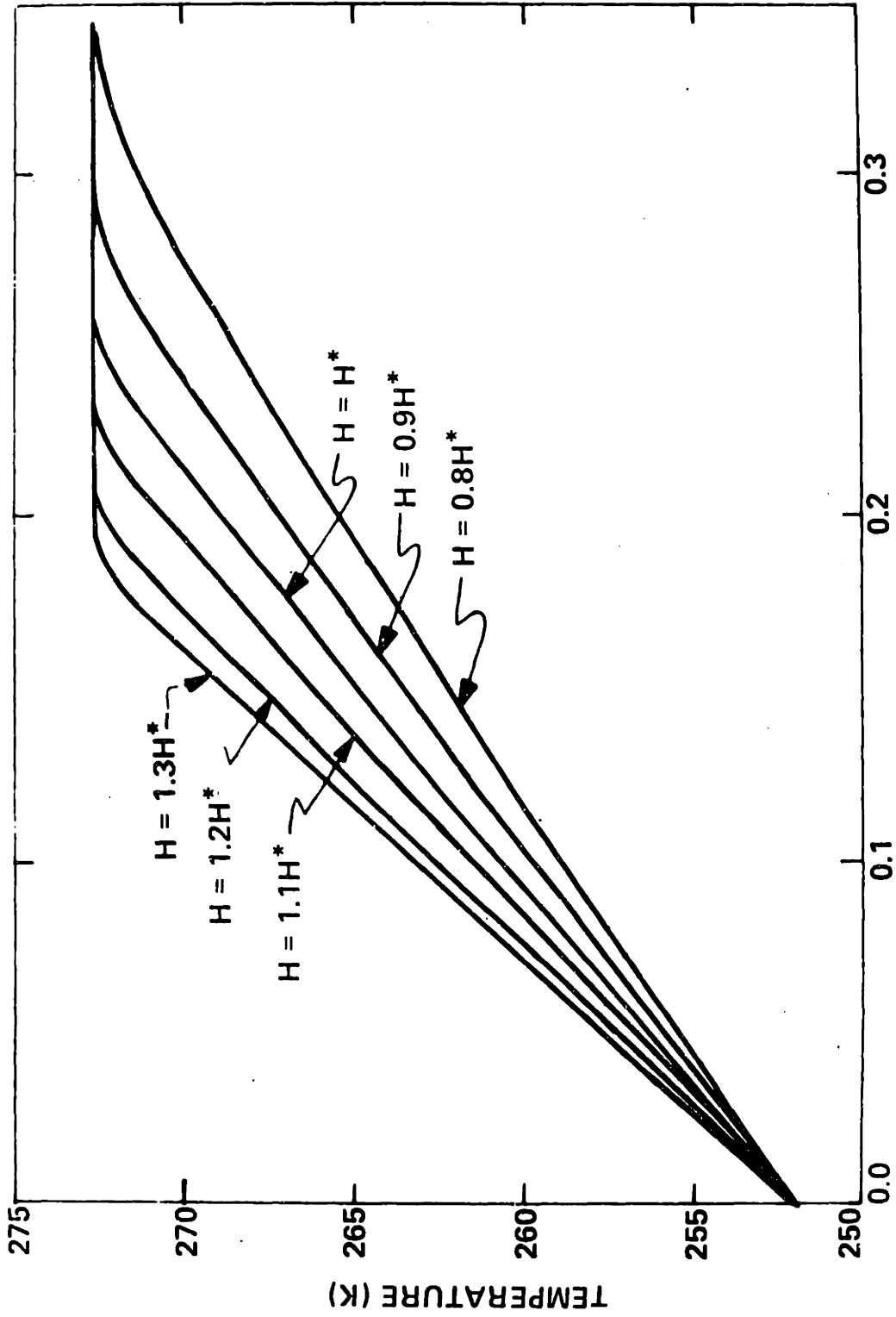
The families of curves describing the solution to the equilibrium solidification equations are shown in Figures (IV-6)-(IV-8) for  $C_\infty = 145 \text{ moles/m}^3$ . As discussed above, the heat flux at any axial position has two components: the solidification heat-flux and the sensible heat flux. These components are given by

$$H_{\text{solidification}} = R \rho_s L_{HF} f_s(z^*) \quad (\text{IV-39})$$

and

$$H_{\text{sensible}} = R \rho_l C_l \{ (T_\infty - T(z^*)) (1 - f_s(z^*)) + \int_0^{f_s} (T_\infty - T(f_s)) df_s \} \\ + R \rho_s C_s \int_0^{f_s} (T(f_s) - T(z^*)) df_s \quad (\text{IV-40})$$

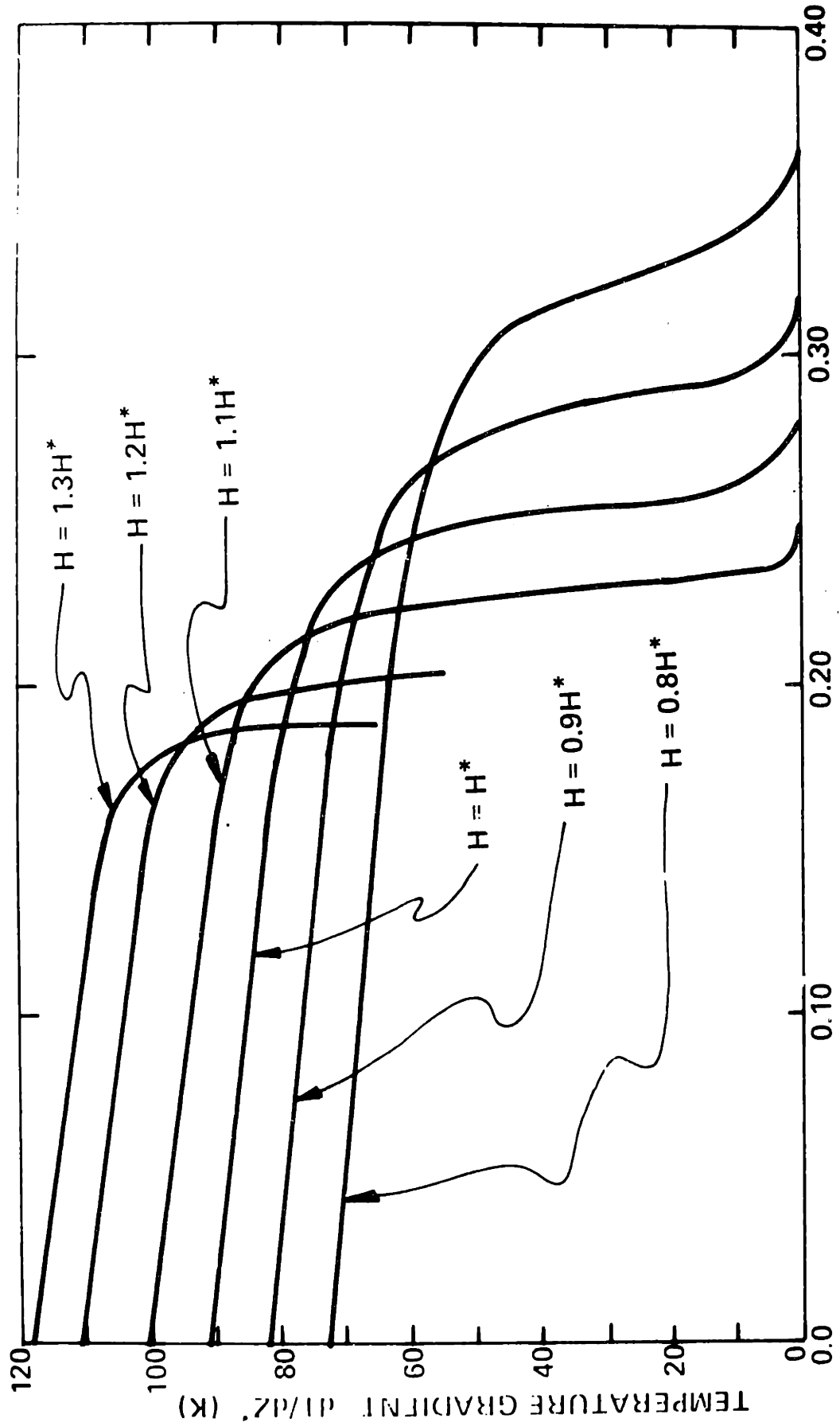
where  $T(f_s) = T(f_s(z^*))$  is the temperature where the solid fraction is at  $f_s$ . The first term in equation (IV-40) is the energy flux necessary to change the temperature of the liquid from the free-field temperature to the solidification temperature, and the second is the flux required to sub-cool the solid. Both components



NON-DIMENSIONAL AXIAL POSITION,  $Z^*$

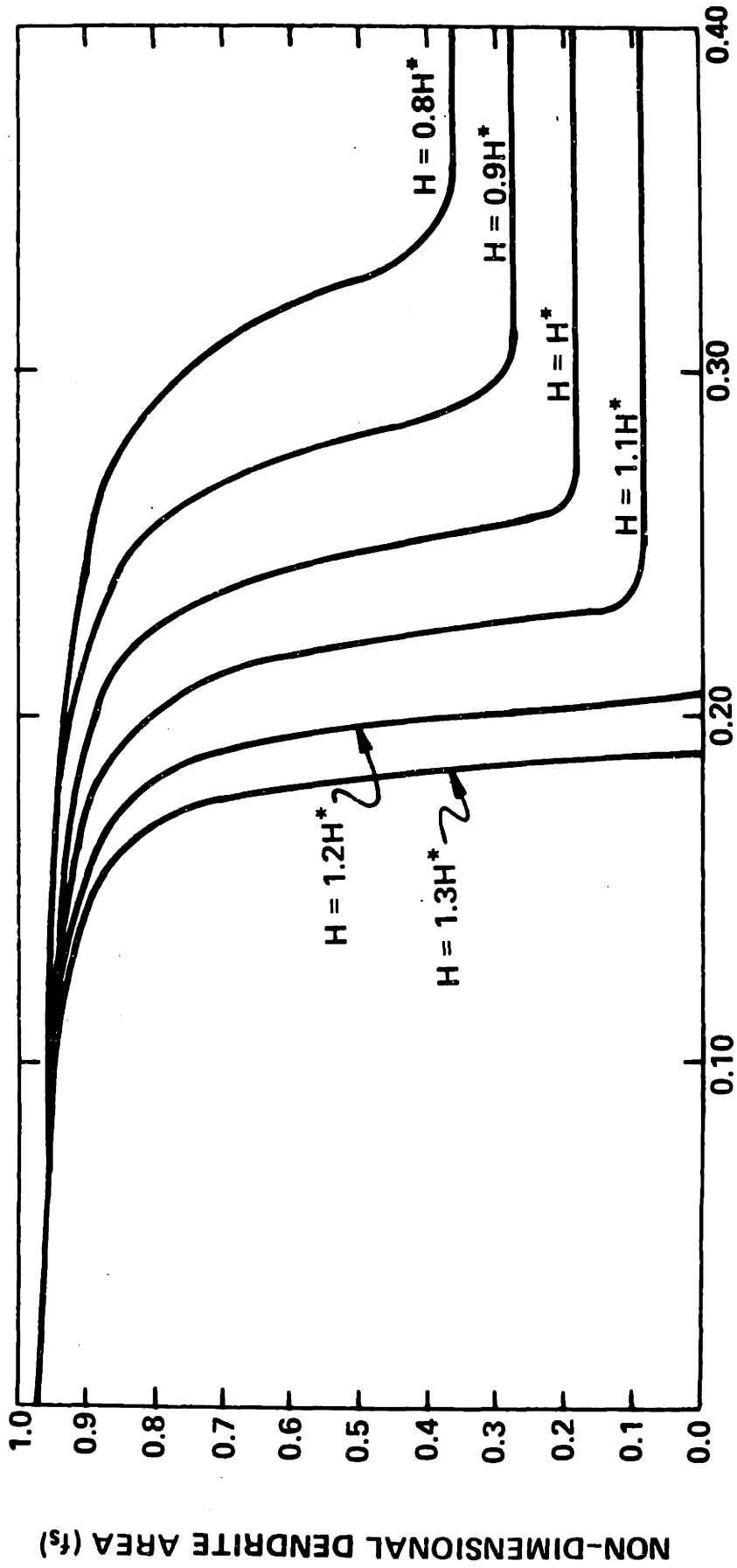
Figure (IV-6) Equilibrium Region Temperature Profiles





NON-DIMENSIONAL AXIAL POSITION

Figure (IV-7) Equilibrium Region Temperature Gradient Profiles.



NON-DIMENSIONAL AXIAL POSITION,  $Z^*$

Figure (IV-8) Equilibrium Region Dendrite Shape Profiles.

contribute to the axial variation of the heat flux but the solidification flux is dominant.

The equilibrium solution predicts that the dendrite cross-sectional area decreases almost linearly with axial position in the region near the basal plane (see Figure (IV-8)), and is closely followed by a similar small decrease in the heat flux, in agreement with equation (IV-39). The temperature profiles are nearly linear in this region since the temperature gradient changes by only a small amount. In the vicinity of the dendrite tip,  $f_s$  drops very sharply followed by similar changes in the heat flux.

Several values of heat flux were used in generating this family of solutions. When the basal heat flux is about 1.1 times the flux necessary for solidification alone, it is just enough to solidify the entire field and remove the necessary sensible heat. In this case the heat flux goes to zero just when the dendrite ends ( $f_s \rightarrow 0$ ). Reducing the heat flux below this "critical" value provides insufficient energy removal to solidify the entire field. Mathematically the heat flux decreases to zero before the solid fraction has gone to zero (as it would at the dendrite tip). This situation corresponds to a hypothetical free-field boundary condition where the material entering the control volume (see Figure IV-5) is part solid.

As the basal heat flux is increased above 1.1  $H^*$ , more

than sufficient heat flux is imposed at the basal plane, and there will be some "leftover" heat flux at the dendrite tips. The hypothetical boundary condition corresponding to this situation is that in which some heat flux enters the control volume from the free field. Physically, this occurs when the free-field temperature is higher than the dendrite tip temperature.

## IV-C HEAT AND MASS TRANSPORT NEAR THE DENDRITE TIPS

### IV-C.1 Introduction

Many different coordinate systems exist besides the familiar cartesian, circular cylinder or spherical systems. In some of these systems, a one-dimensional surface would be transformed to a curved surface in the "real-life" Cartesian system. The objective in this section is to find a particular coordinate system whose one-dimensional translation into the cartesian or circular cylinder system yields surfaces which are geometrically similar to the dendrite tips. Transport equations will then be derived and solved which will describe the temperature and concentration fields in terms of a single independent spatial coordinate.

### IV-C.2 Spheroidal Coordinate System

A plausible assumption about the shape of the tips is that their cross-sectional area is related to  $z$  by a quadratic form, described by

$$r = \alpha + \beta z + \gamma z^2 \quad . \quad (IV-41)$$

From surface energy considerations, the tips must be convex out, which places restrictions on possible values of the coefficients. The most general mathematical expression of the

quadratic form with these restrictions is the oblate or prolate spheroidal coordinate system. These systems are shown schematically in Figure (IV-9) and are mathematically related to the Cartesian coordinate system by

$$\begin{aligned}x &= a \cosh\eta \sin\theta \cos\psi \\y &= a \cosh\eta \sin\theta \sin\psi \\z &= a \sinh\eta \cos\theta\end{aligned}\tag{IV-42}$$

for the oblate case, and

$$\begin{aligned}x &= a \sinh\eta \sin\theta \cos\psi \\y &= a \sinh\eta \sin\theta \sin\psi \\z &= a \cosh\eta \cos\theta\end{aligned}\tag{IV-43}$$

for the prolate case. Using the standard transformation from Cartesian to circular cylinder coordinates, we have

$$\begin{aligned}r &= a \cosh\eta \sin\theta \\z &= a \sinh\eta \cos\theta\end{aligned}\tag{IV-44}$$

} oblate

and

$$\begin{aligned}r &= a \sinh\eta \sin\theta \\z &= a \cosh\eta \cos\theta\end{aligned}\tag{IV-45}$$

} prolate

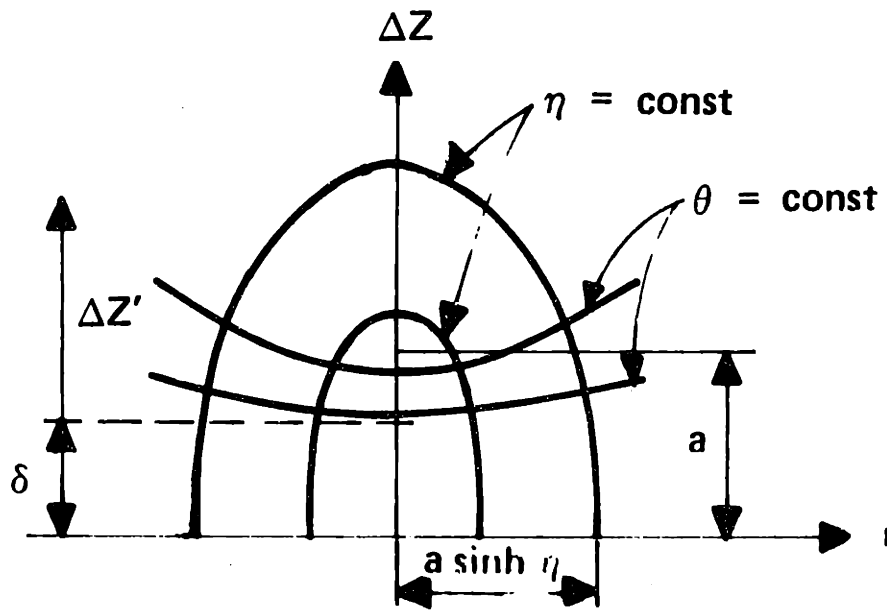
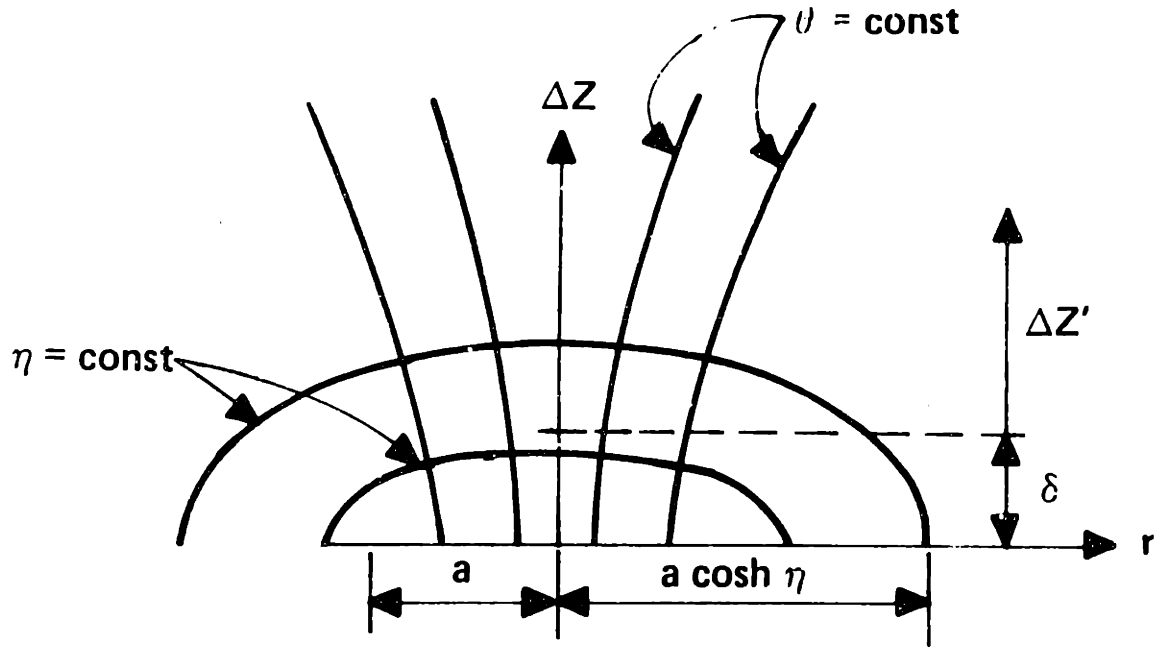


Figure (IV-9) Oblate (top) and Prolate Spheroidal Coordinate Systems.

These spheroidal coordinate systems are axially symmetric ellipsoidal systems generated by rotating an orthogonal family of confocal ellipses and hyperbolas about the major (prolate) or minor (oblate) axes of the ellipses.

The surfaces  $\eta = \text{constant}$  describe specific kinds of paraboloids identical in form to these described by equation (IV-41) and may be used to express the shape of the dendrite tips. The major and minor axes  $b_1$  and  $c_1$  respectively, of a typical ellipsoid ( $\eta = \text{constant}$ ) are given by

$$b_1 = a \cosh \eta \quad (\text{IV-45a})$$

and

$$c_1 = a \sinh \eta \quad (\text{IV-45b})$$

where  $a$  is the position of the ellipsoidal foci (see Figure (IV-9)).

$\eta$  ranges from 0 to infinity relating to varying degrees of "pointedness" of the dendrite tips in either the oblate or prolate case. Oblate spheroids range from flattened discs of radius  $a$  ( $\eta=0$ ) to spherical ( $\eta \rightarrow \infty$ ) and prolate spheroids vary from spherical ( $\eta \rightarrow \infty$ ) to infinitely pointed, i.e., a focal line segment of length  $a$ , as  $\eta \rightarrow 0$ . Thus



dendrite tips described by the surfaces  $\eta = \text{constant}$  may assume any degree of "pointedness", within the convex-out restriction.

The coordinate  $\eta = \eta_{\text{tip}}$  describes the oblate spheroid at the dendrite surface. To describe the surface in the form of equation (IV-41) the  $\theta$  dependence is eliminated in equations (IV-44) and (IV-45) to obtain,

$$r = a \cosh \eta_{\text{tip}} \sqrt{1.0 - \left[ \frac{\Delta z}{a \sinh \eta_{\text{tip}}} \right]^2} \quad (\text{IV-46a})$$

for the oblate case and

$$r = a \sinh \eta_{\text{tip}} \sqrt{1.0 - \left[ \frac{\Delta z}{a \cosh \eta_{\text{tip}}} \right]^2} \quad (\text{IV-46b})$$

for the prolate case, where  $\Delta z$  is measured from the origin of the spheroidal coordinate system (see Figure (1: 9)).

In order to provide some additional flexibility in describing the tip spheroid, we transform to a coordinate system displaced by a distance  $\delta$  in the positive  $z$  direction. Using the transformation

$$\Delta z = \Delta z' + \delta \quad (\text{IV-47})$$

in equations (IV-46), we have

$$r = a \cosh \eta_{\text{tip}} \sqrt{1 - \left[ \frac{\Delta z' + \delta}{a \sinh \eta_{\text{tip}}} \right]^2} \quad (\text{IV-48a})$$

and

$$r = a \sinh \eta_{\text{tip}} \sqrt{1 - \left[ \frac{\Delta z' + \delta}{a \cosh \eta_{\text{tip}}} \right]^2} \quad (\text{IV-48b})$$

for the oblate and prolate cases respectively. Finally, we use the definition of the solid fraction  $f_s$ , given by

$$f_s = \frac{\text{cross-sectional area occupied by solid material}}{\text{total cross-sectional area}} \quad (\text{IV-49})$$

Substituting into equation (IV-48) we have

$$\begin{aligned} f_s &= \left( \frac{a}{L_D} \right)^2 \cosh^2 \eta_{\text{tip}} - \delta^2 \left( \frac{L^*}{L_D} \right)^2 \coth^2 \eta_{\text{tip}} \quad (\text{IV-50a}) \\ &\quad - 2\delta \left( \frac{L^*}{L_D} \right)^2 \coth^2 \eta_{\text{tip}} (\Delta z^*) - \left( \frac{L^*}{L_D} \right)^2 \coth^2 \eta_{\text{tip}} (\Delta z^*)^2 \end{aligned}$$

and

$$\begin{aligned} f_s &= \left( \frac{a}{L_D} \right)^2 \sinh^2 \eta_{\text{tip}} - \delta^2 \left( \frac{L^*}{L_D} \right)^2 \tanh^2 \eta_{\text{tip}} \quad (\text{IV-50b}) \\ &\quad - 2\delta \left( \frac{L^*}{L_D} \right)^2 \tanh^2 \eta_{\text{tip}} (\Delta z^*) - \left( \frac{L^*}{L_D} \right)^2 \tanh^2 \eta_{\text{tip}} (\Delta z^*)^2 \end{aligned}$$

for the oblate and prolate cases respectively, where

$$\Delta z^* = \Delta z' / L^*$$

$L^*$  = the characteristic dendrite length

(see section III-B).

and

$L_D$  = the dendrite spacing (see Appendix II).

Equations (IV-50) describe the dendrite tip surface in terms of the spheroidal coordinate parameters. It will be necessary to have the tips described in this manner for the equilibrium-spheroidal matching procedure described in Section E.

#### IV-C.3 Transport Equation

The equation describing the steady heat and mass transport fields near the dendrite tips is given by

$$\nabla^2 P + \frac{R}{D_i} \frac{\partial P}{\partial z} = 0 \quad (IV-52)$$

where  $P$  represents either temperature or concentration and  $i = m, \ell$  or  $s$ , denoting the mass diffusivity or the thermal diffusivity in the liquid or solid, respectively. The scalar Laplacian  $\nabla^2$  and the partial derivative  $\partial/\partial z$  may be expressed in spheroidal coordinates by using equations (IV-42)

and (IV-43) [42]. With these transformations equation (IV-52) becomes

$$\frac{1}{a^2 (\sinh^2 \eta + \sin^2 \theta)} \left[ \frac{\partial^2 P}{\partial \eta^2} + \coth \eta \frac{\partial P}{\partial \eta} + \frac{\partial^2 P}{\partial \theta^2} + \cot \theta \frac{\partial P}{\partial \theta} \right] + \frac{R}{D_i a \sinh \eta \cos \theta} \frac{\partial P}{\partial \eta} = 0 \quad (\text{IV-53a})$$

for the prolate case and

$$\frac{1}{a^2 (\cosh^2 \eta + \sin^2 \theta)} \left[ \frac{\partial^2 P}{\partial \eta^2} + \tanh \eta \frac{\partial P}{\partial \eta} + \frac{\partial^2 P}{\partial \theta^2} + \tan \theta \frac{\partial P}{\partial \theta} \right] + \frac{R}{D_i a \cosh \eta \cos \theta} \frac{\partial P}{\partial \eta} = 0 \quad (\text{IV-53b})$$

for the oblate case.

Ivantsov [4] analyzed heat and mass transport in the vicinity of dendrite tips described by equation (V-41). He found that the isotherms and isoconcentrates are mathematically similar in form to the dendrite tip equation. This result implies that the iso-potential loci are  $\eta = \text{constant}$  surfaces and that the temperature and concentration fields are one-dimensional in the spheroidal coordinate  $\eta$  in both the oblate and prolate cases. Eliminating the  $\frac{\partial}{\partial \theta}$  and  $\frac{\partial^2}{\partial \theta^2}$  terms in equations (IV-53) and using  $\sin \theta \approx 0$  and  $\cos \theta \approx 1$ , we have

$$\frac{\partial^2 P}{\partial \eta^2} + [\text{Pec}_i \cosh \eta + \tanh \eta] \frac{\partial P}{\partial \eta} = 0 \quad (\text{IV-54a})$$

for the oblate case and

$$\frac{\partial^2 P}{\partial \eta^2} + [\text{Pec}_i \sinh \eta + \coth \eta] \frac{\partial P}{\partial \eta} = 0 \quad (\text{IV-54b})$$

for the prolate case, where

$$\text{Pec}_i = \frac{\text{Ra}}{D_i} = \text{the Peclet number for mass and thermal diffusion.}$$

These Peclet numbers are related by

$$\text{Pec}_m = \frac{D_L}{D_m} \text{Pec}_L \quad (\text{IV-55})$$

and

$$\text{Pec}_m = \frac{D_S}{D_m} \text{Pec}_S \quad (\text{IV-56})$$

Using numerical values of  $D_m$ ,  $D_S$  and  $D_L$  from Table III-2 gives  $\text{Pec}_m \approx 10^3 D_S$  and  $\text{Pec}_m \approx 10^4 D_L$ . The temperature and concentration fields will be geometrically similar in shape, but the "parametric distortion" of the concentration field will be about  $10^3 - 10^4$  times as much. Equations (IV-54) apply in the region bounded by  $\theta = 0$  (dendrite axis) and  $\theta \approx 30^\circ$  to comply with

the simplifications. These equations are first order in

$\frac{\partial P}{\partial \eta}$  allowing them to be integrated analytically, yielding the following solution:

$$\frac{dP}{d\eta} = - K_j^i \frac{e^{-Pec_i \cosh \eta}}{\sinh \eta} \quad (IV-57a)$$

$$P(\eta_{tip}) - P_\infty = K_j^i \int_{\eta_{tip}}^{\infty} \frac{e^{-Pec_i \cosh \eta}}{\sinh \eta} d\eta \quad (IV-57b)$$

for the prolate case, and

$$\frac{dP}{d\eta} = - K_j^i \frac{e^{-Pec_i \sinh \eta}}{\cosh \eta} \quad (IV-57c)$$

$$P(\eta_{tip}) - P_\infty = K_j^i \int_{\eta_{tip}}^{\infty} \frac{e^{-Pec_i \sinh \eta}}{\cosh \eta} d\eta \quad (IV-57d)$$

for the oblate case, where the  $K$ 's are constants of integration and  $j =$  oblate or prolate and  $i = m, \ell$  or  $s$ .

For convenience, let us define two sets of functions

$f(\eta, Pec_i)$  and  $g(\eta, Pec_i)$  as follows:

$$f_{oblate} = \frac{e^{-Pec_i \sinh \eta}}{\cosh \eta} \quad (IV-58)$$

$$f_{prolate} = \frac{e^{-Pec_i \cosh \eta}}{\sinh \eta} \quad (IV-59)$$

$$g_{\text{oblate}} = \int_{\eta}^{\infty} f_{\text{oblate}} d\eta \quad (IV-60)$$

$$g_{\text{prolate}} = \int_{\eta}^{\infty} f_{\text{prolate}} d\eta \quad (IV-61)$$

Substituting equations (IV-58) - (IV-61) into equations (IV-57), we have

$$\frac{dP_i}{d\eta} = -K_j^i f_j(\text{Pec}_i, \eta)$$

and (IV-62)

$$P_i(\eta_{\text{tip}}) - P_{\infty} = K_j^i g_j(\text{Pec}_i, \eta_{\text{tip}})$$

#### IV-C.4 Boundary Conditions

Equations (IV-57b) and (IV-57d) were obtained by using the free-field boundary condition

$$P \rightarrow P_{\infty} \text{ as } \eta \rightarrow \infty \quad (IV-63)$$

which applies for both the temperature and concentration fields. Complete rejection of solute from the ice crystal requires the solute particle velocity to vanish at the dendrite surface giving

$$D_m \nabla C_s + RC_s = 0 \text{ (on dendrite surface) .} \quad (\text{IV-64})$$

Transforming to the spheroidal coordinate geometry, we have

$$\frac{\partial C_s}{\partial \eta} + Pec_m \sinh \eta C_s = 0 \quad (\eta = \eta_{tip}) \quad (\text{IV-65a})$$

for the prolate case and

$$\frac{\partial C_s}{\partial \eta} + Pec_m \cosh \eta C_s = 0 \quad (\eta = \eta_{tip}) \quad (\text{IV-65b})$$

for the oblate case. Substituting equations (IV-62) into equations (IV-65) gives

$$K_o^m = \frac{C_\infty Pec_m \cosh \eta_{tip}}{f_o(Pec_m, \eta_{tip}) - Pec_m \cosh \eta_{tip} g_o(Pec_m, \eta_{tip})} \quad (\text{IV-66})$$

and

$$K_p^m = \frac{C_\infty Pec_m \sinh \eta_{tip}}{f_p(Pec_m, \eta_{tip}) - Pec_m \sinh \eta_{tip} g_p(Pec_m, \eta_{tip})} . \quad (\text{IV-67})$$

Specifying the foci coordinate  $a$ , the degree of "pointedness" of the dendrite tip, and the interface speed  $R$ , uniquely determines the concentration field ahead of the dendrites.



The thermal interface boundary condition for the liquid phase temperature profile may be calculated by using the equilibrium condition given by equation (III-13):

$$T(\eta_{tip}) = a' + b'C_s(\eta_{tip}) + c'C_s^2(\eta_{tip}) + d'C_s^3(\eta_{tip}). \quad (III-13)$$

Using equations (IV-62) with the relationship yields

$$K_p^\ell = \frac{T(\eta_{tip}) - T_\infty}{g_p(Pec_\ell, \eta_{tip})} \quad (IV-68)$$

and

$$K_o^\ell = \frac{T(\eta_{tip}) - T_\infty}{g_o(Pec_\ell, \eta_{tip})} \quad (IV-69)$$

The solid phase integration constant,  $K_j^S$  is determined by using equation (IV-62) and the moving boundary condition at the interface given by

$$\left[\frac{\partial T}{\partial z}\right]_{solid} = \frac{K_s}{K_\ell} \left[\frac{\partial T}{\partial z}\right]_{liquid} + \frac{R \rho_s L_{HF}}{K_\ell} \quad (III-16)$$

Combining these results, we have

$$K_p^S = \frac{K_\ell}{K_s} K_p^\ell \frac{f_p(Pec_\ell, \eta_{tip})}{f_p(Pec_s, \eta_{tip})} - \frac{R \rho_s L_{HF}}{K_s} a \sinh \eta_{tip} \quad (IV-70)$$

and

$$K_0^S = \frac{K_l}{K_s} K_0^l \frac{f_0(\text{Pec}_L, \eta_{\text{tip}})}{f_0(\text{Pec}_S, \eta_{\text{tip}})} - \frac{R \rho_s L_{\text{HF}}}{K_s} a \cosh \eta_{\text{tip}} \quad (\text{IV-71})$$

#### IV-C.5 Results

The relative concentration and temperature profiles are shown in Figures (IV-10) and (IV-11) as a function of the dendrite tip geometry ( $\eta_{\text{tip}}$ ) and the Peclet number. The spatial coordinate  $\eta$  is measured from the origin of the spheroidal coordinate system and is related to axial displacement by

$$\Delta z = a \sinh \eta \quad (\text{IV-72})$$

for the oblate case, and

$$\Delta z = a \cosh \eta \quad (\text{IV-73})$$

for the prolate case.

The curves in both figures change very rapidly near the dendrite surface but trail off slowly approaching the free-field. The concentration and temperature variation is of the form  $\exp(-\text{Pec} \exp(\eta))$  near the dendrite tips by equation (IV-57).

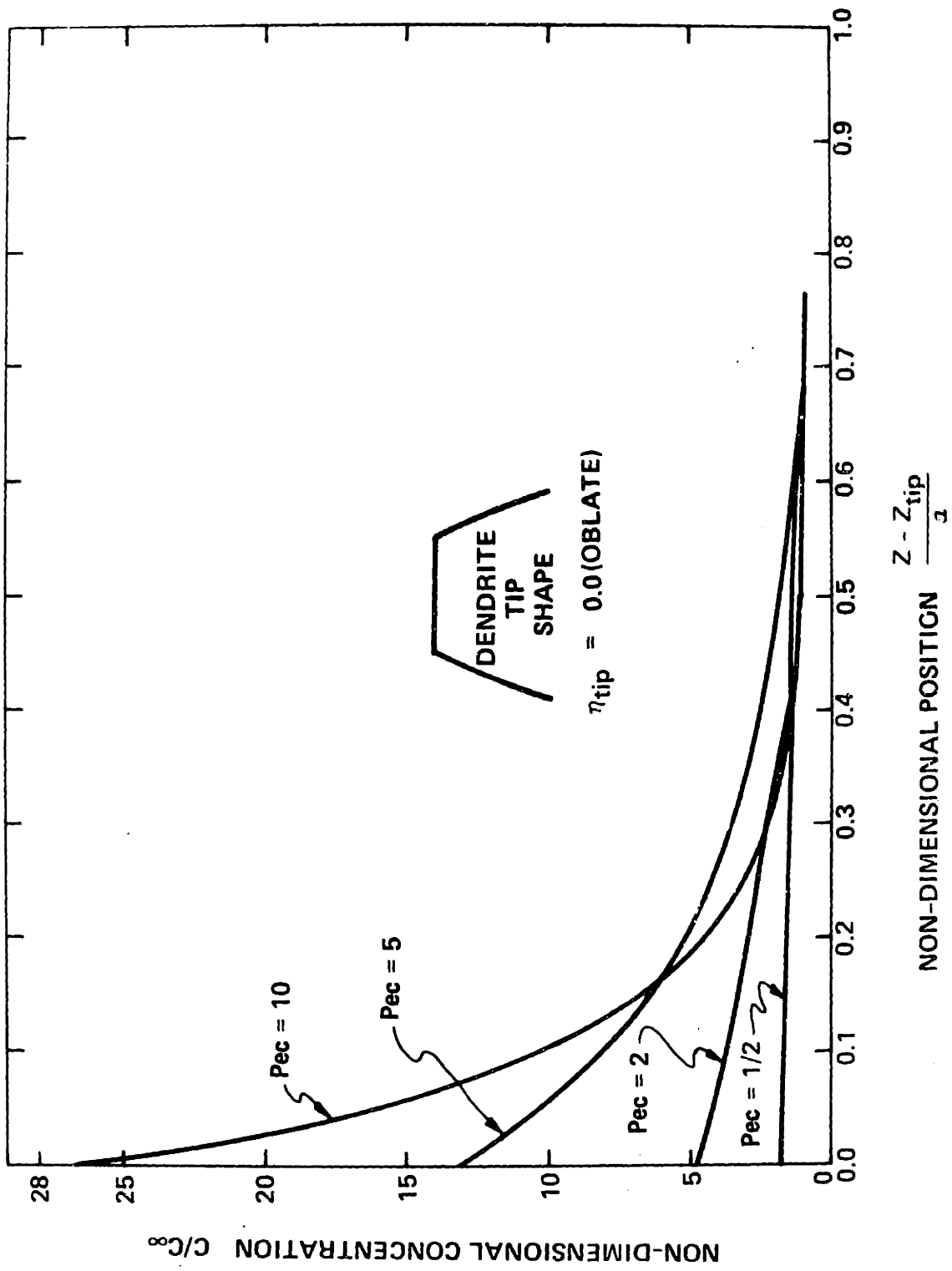
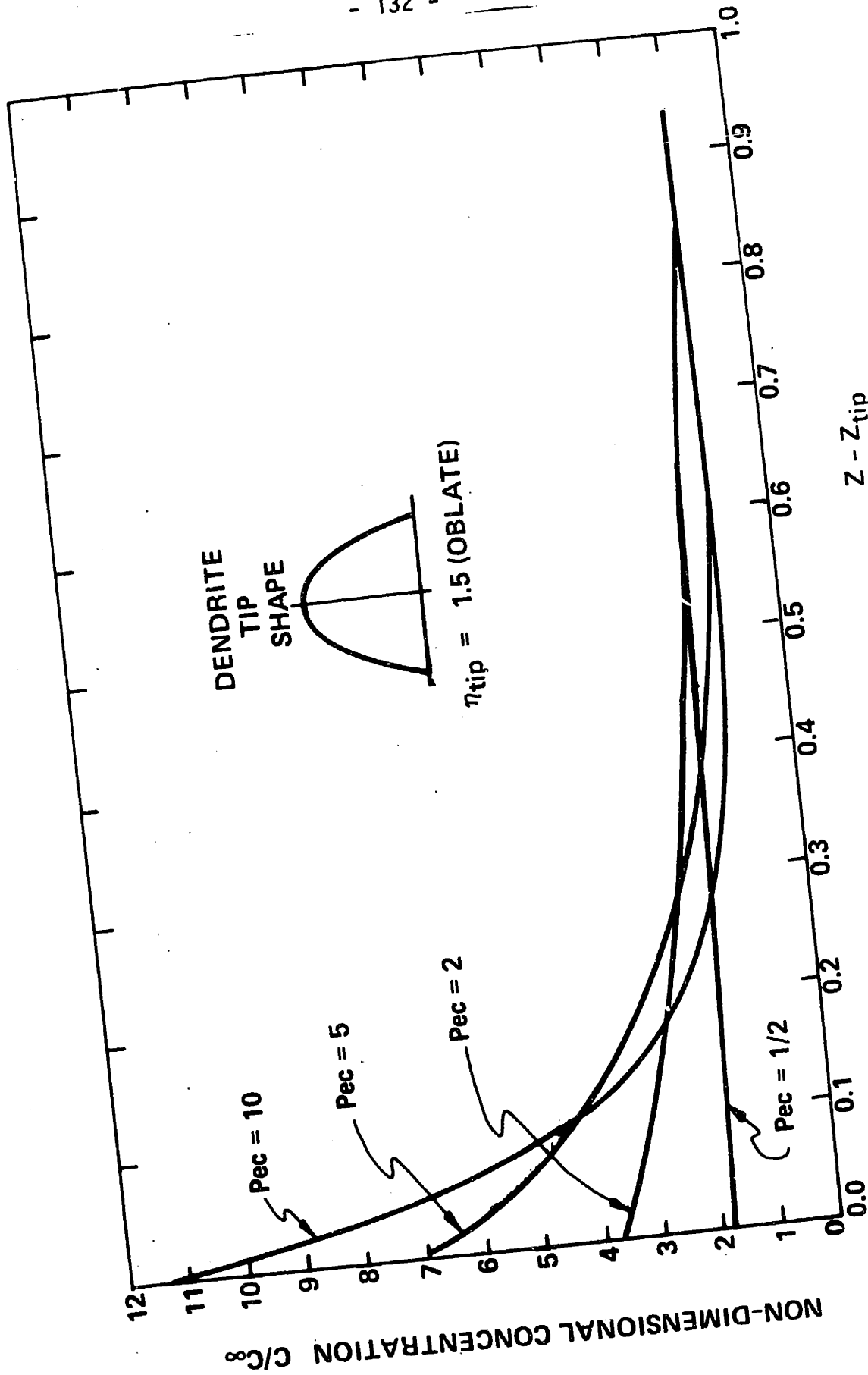


Figure (IV-10a) Spheroidal Coordinate Region Concentration Profile,  $\eta_{tip} = 0.0$  (oblate).



NON-DIMENSIONAL POSITION  $\frac{Z - Z_{tip}}{a}$   
 $\eta_{tip} = 1.5$

Figure (IV-10b) Spheroidal Coordinate Region Concentration Profile,  $\eta_{tip} = 1.5$  (oblate).

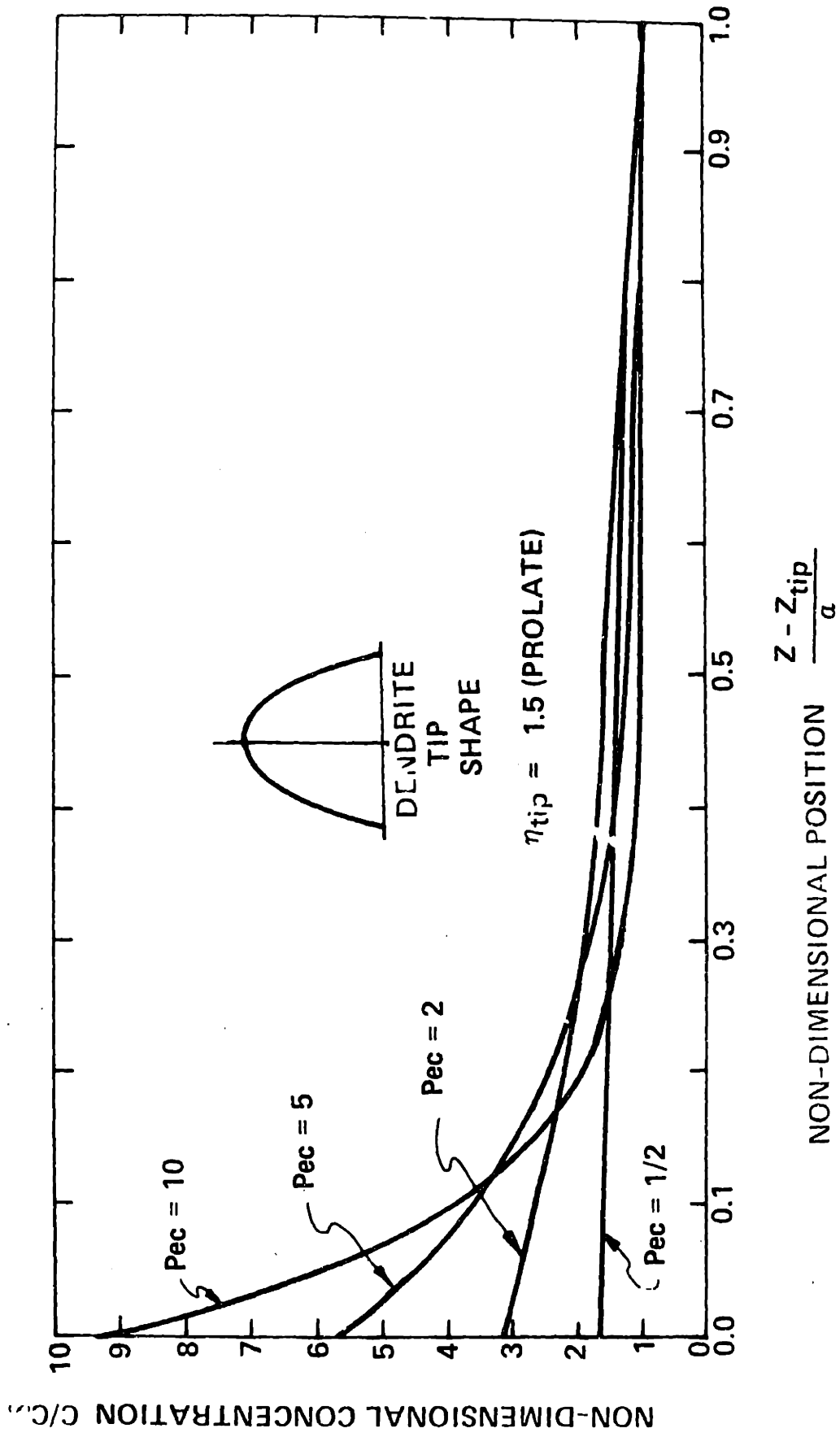
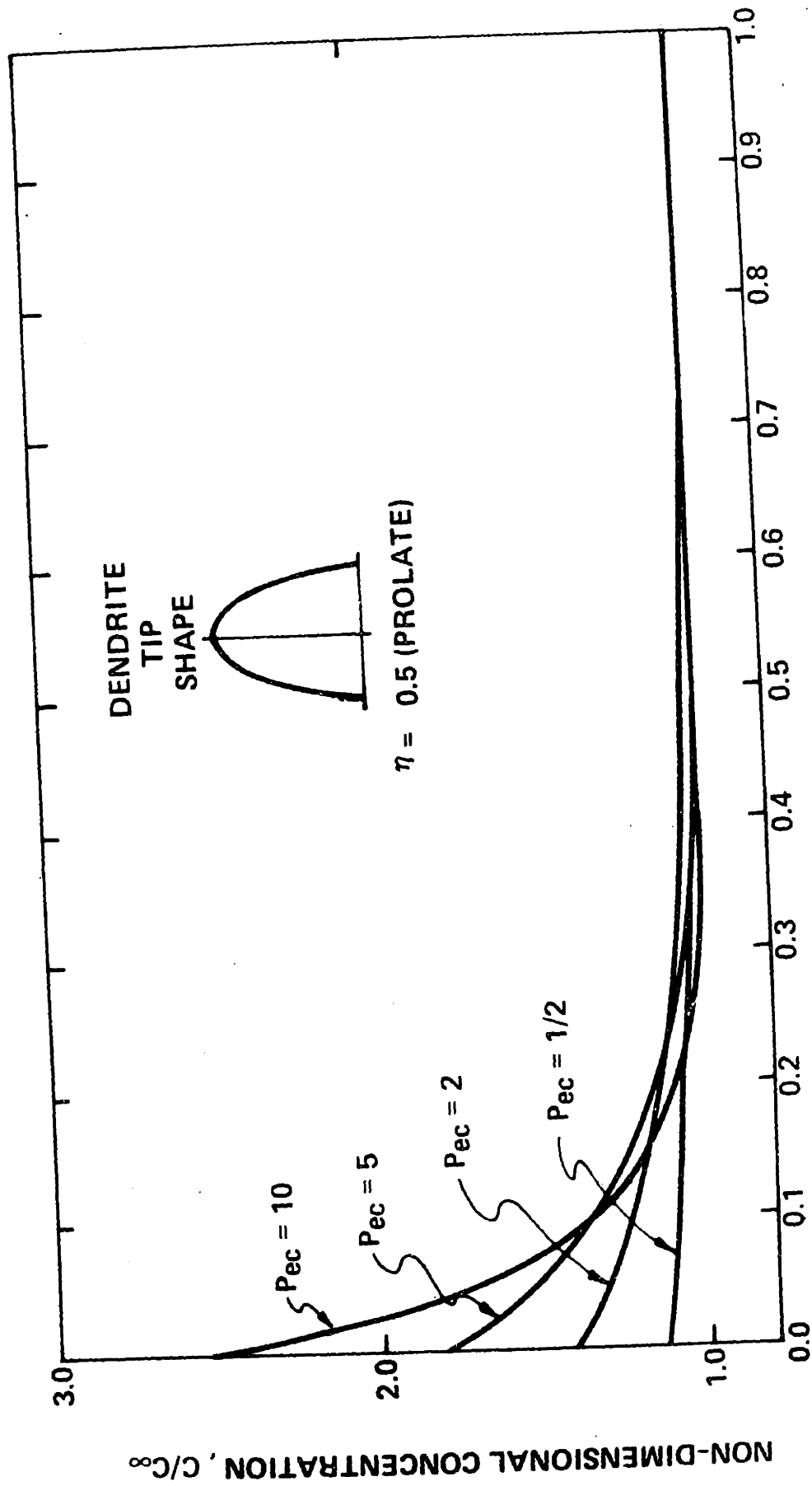


Figure (IV-10c) Spheroidal Coordinate Region Concentration Profile,  $\eta_{tip} = 1.5$  (prolate).



NON-DIMENSIONAL POSITION,  $\frac{Z - Z_{tip}}{a}$

Figure (IV-10d) Spheroidal Coordinate Region Concentration Profile,  $\eta_{tip} = 0.5$  (prolate).

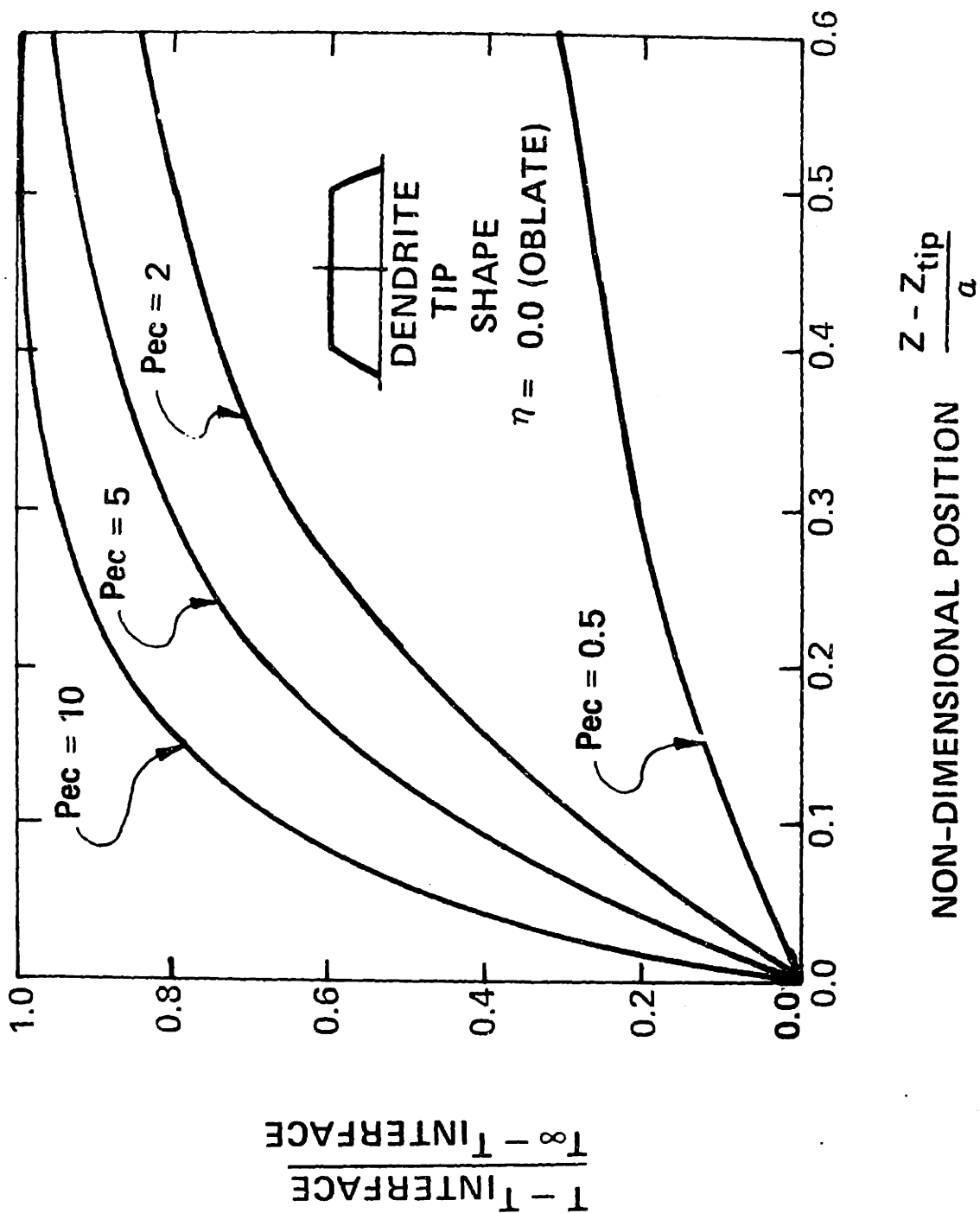


Figure (IV-11a) Spheroidal Coordinate Region Temperature Profile,  $\eta_{\text{tip}} = 0.0$  (oblate).

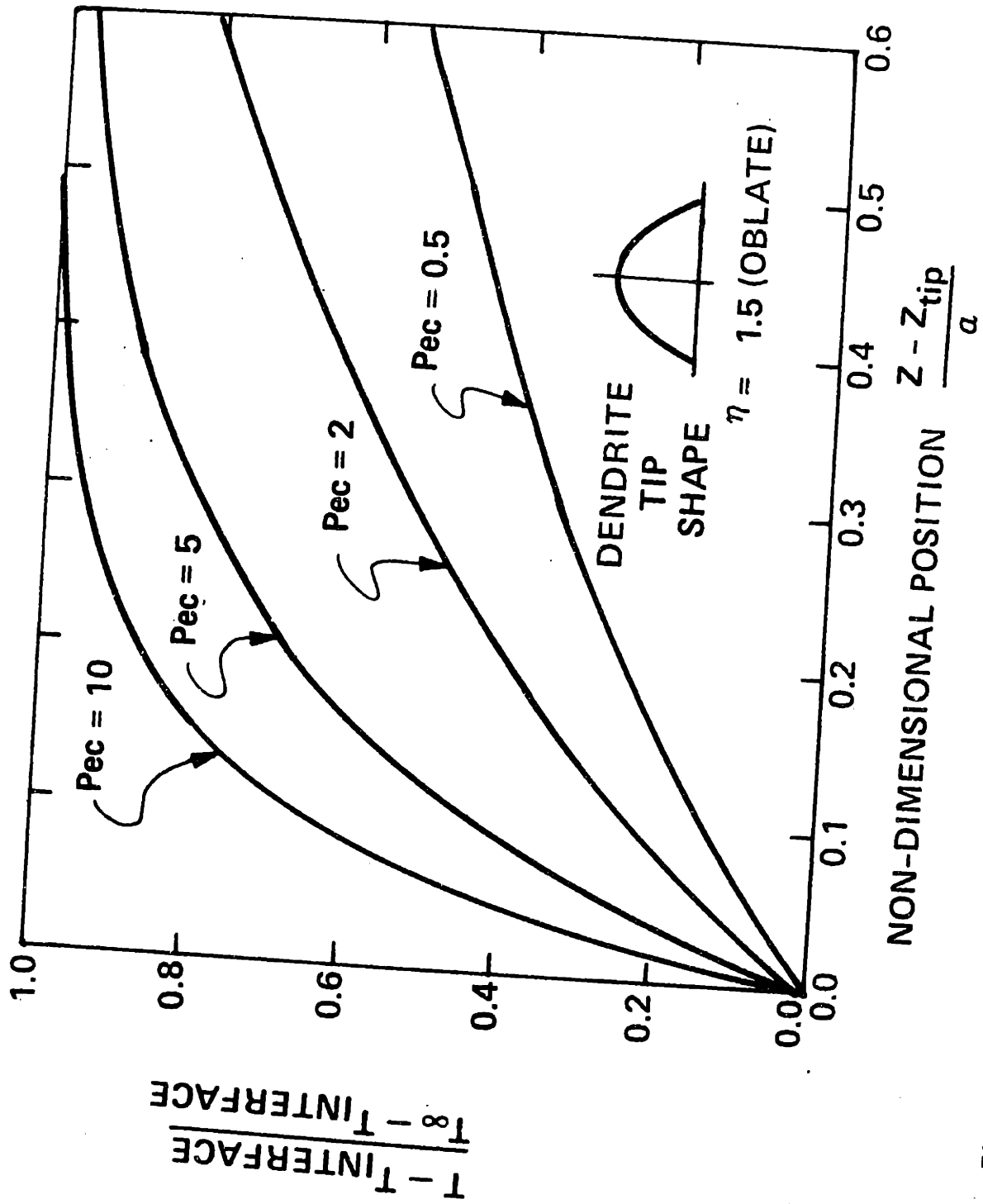


Figure (IV-11b) Spheroidal Coordinate Region Temperature Profile,  $\eta_{\text{tip}} = 1.5$  (oblate).



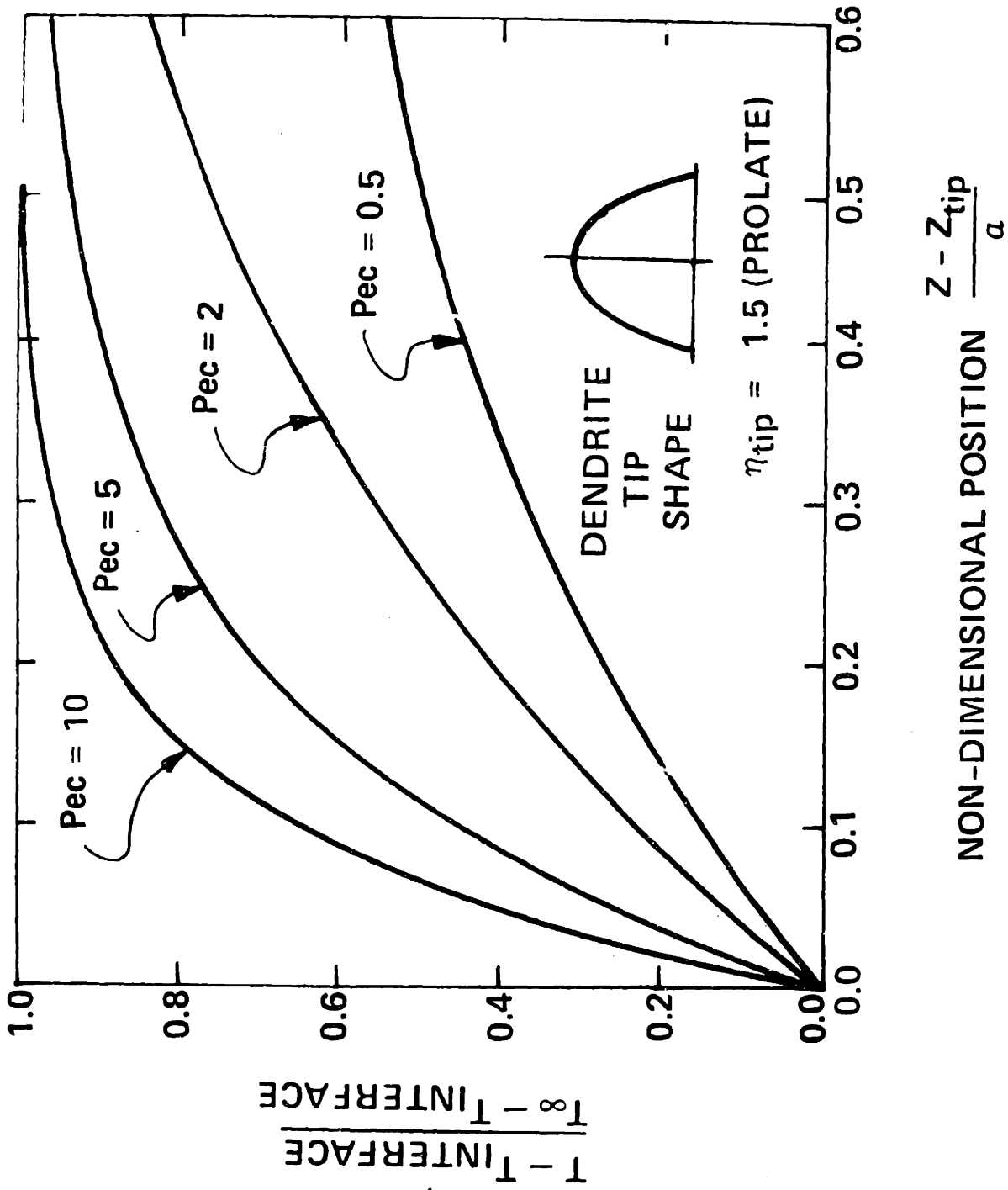


Figure (IV-11c) Spheroidal Coordinate Region Temperature Profile,  $\eta_{\text{tip}} = 1.5$  (prolate).

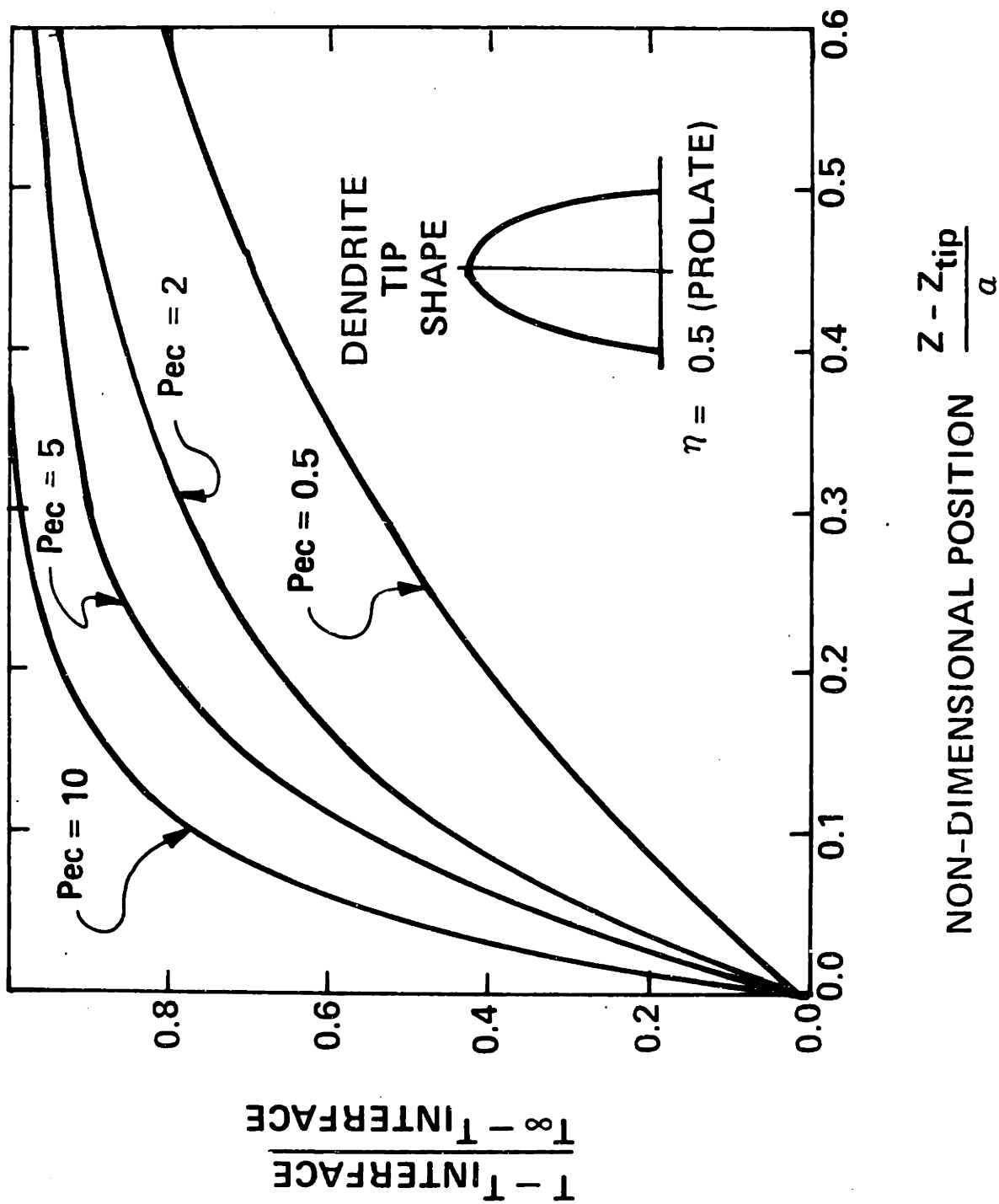


Figure (IV-11d) Spheroidal Coordinate Region Temperature Profile,  $\eta_{\text{tip}} = 0.5$  (prolate).

The temperature profiles shown in Figure (IV-11) are generated by the same equation as the concentration profiles and their form and variation are similar.

There are three factors influencing the magnitude of the concentration profile: the degree of pointedness of the dendrite, the rate of advance of the interface and the extent (width) of the dendrite tip. The profiles are expected to be much less severe as the pointedness is increased (all other factors constant) and this is illustrated in Figures (IV-10) and (IV-11) by comparing profiles with constant  $Pec_m$  and different  $\eta_{tip}$  (for example  $Pec = 1/2$  for  $\eta_{tip} = 0$ , 1.5 (oblate) and 5.0, 0.5 (prolate)). However, the width of the dendrite tip is given by a  $\cosh \eta_{tip}$  or a  $\sinh \eta_{tip}$  (prolate and oblate, respectively) from equations (IV-41) and (IV-42). Thus, changing the degree of pointedness ( $\eta_{tip}$ ) at constant  $R$  and  $Pec$ , changes the width of the dendrite. Increasing  $\eta_{tip}$  produces two opposite effects: a reduction in magnitude of the concentration field due to an increase in pointedness and an intensification of the field due to an increase in the dendrite width.

To compare the relative concentration and temperature profiles in front of dendrites of varying pointedness but constant width, we construct a family of curves at constant

interface speed  $R$  and constant dendrite width  $a \cosh n_{tip}$  or a  $\sinh n_{tip}$  (oblate or prolate). This is shown in figures (IV-12) and (IV-13) for a dendrite width of  $100 \mu\text{m}$  and various values of interface speed and pointedness. Plotted in this way, the drastic effect of interface speed, and degree of pointedness is obvious.

#### IV-D Optimization Condition

As discussed in Section IV-A.3, an additional condition is necessary to complete the problem specification. Since the problem is assumed to be at steady-state, the dendrite tips must be thermodynamically stable. Otherwise, the perturbed dendrite tips would transform to a more pointed and stable configuration, and the original dendrite shape was not truly steady. This restriction still leaves an infinite number of possible dendrite configurations. These include the unique, marginally stable shape and any other shape within the "more than stable" region.

Dendrites are formed from an initially planar interface that becomes unstable. The growth of perturbations tends to relieve the instability, and the dendrites will continue to become more pointed until they become stable. The driving force for a change of configuration then, is the thermodynamic instability. The configuration that is truly steady is the one

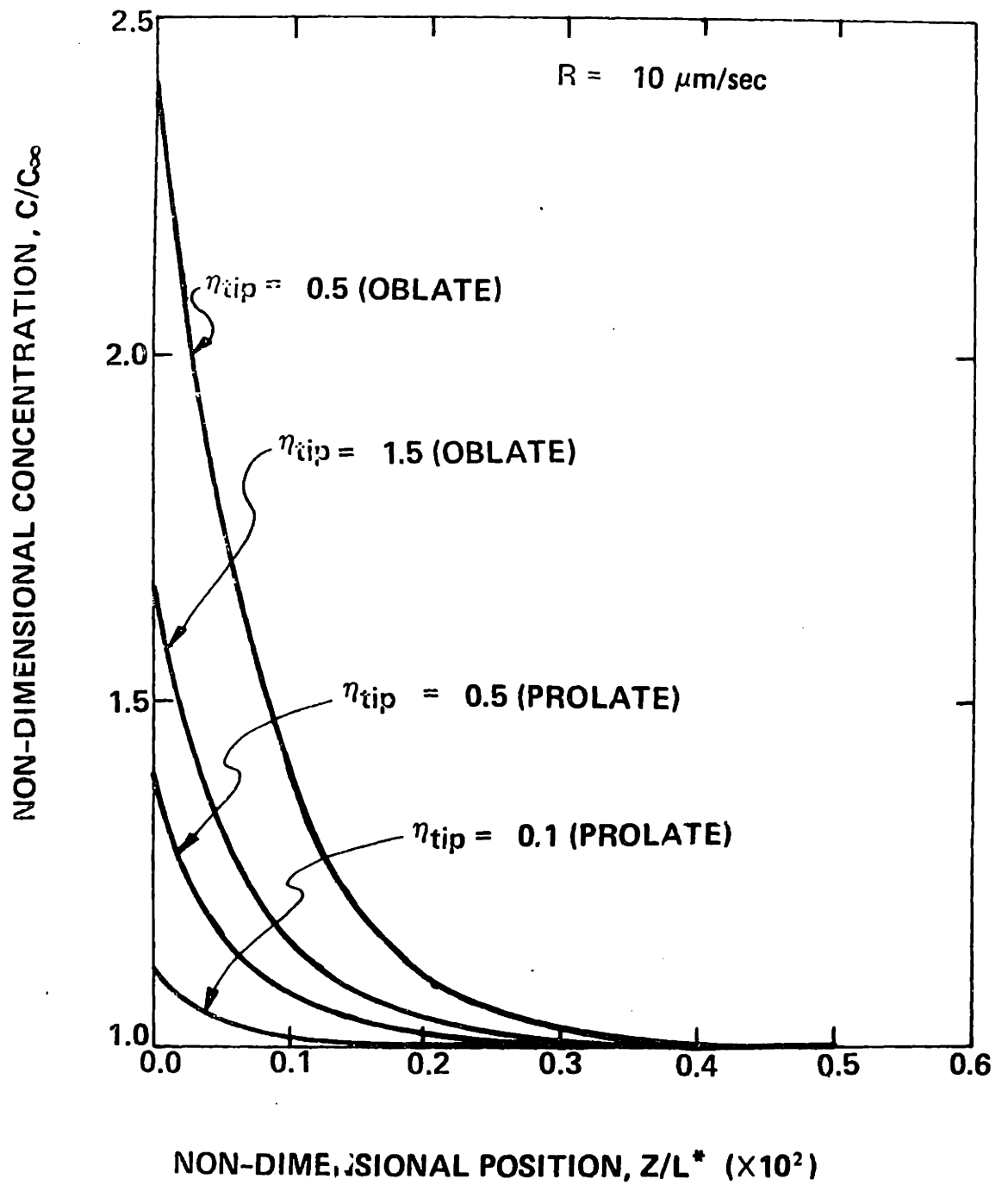


Figure (IV-12a) Relative Concentration Profiles for Constant Dendrite Width,  $R = 10 \mu\text{m/sec}$ .

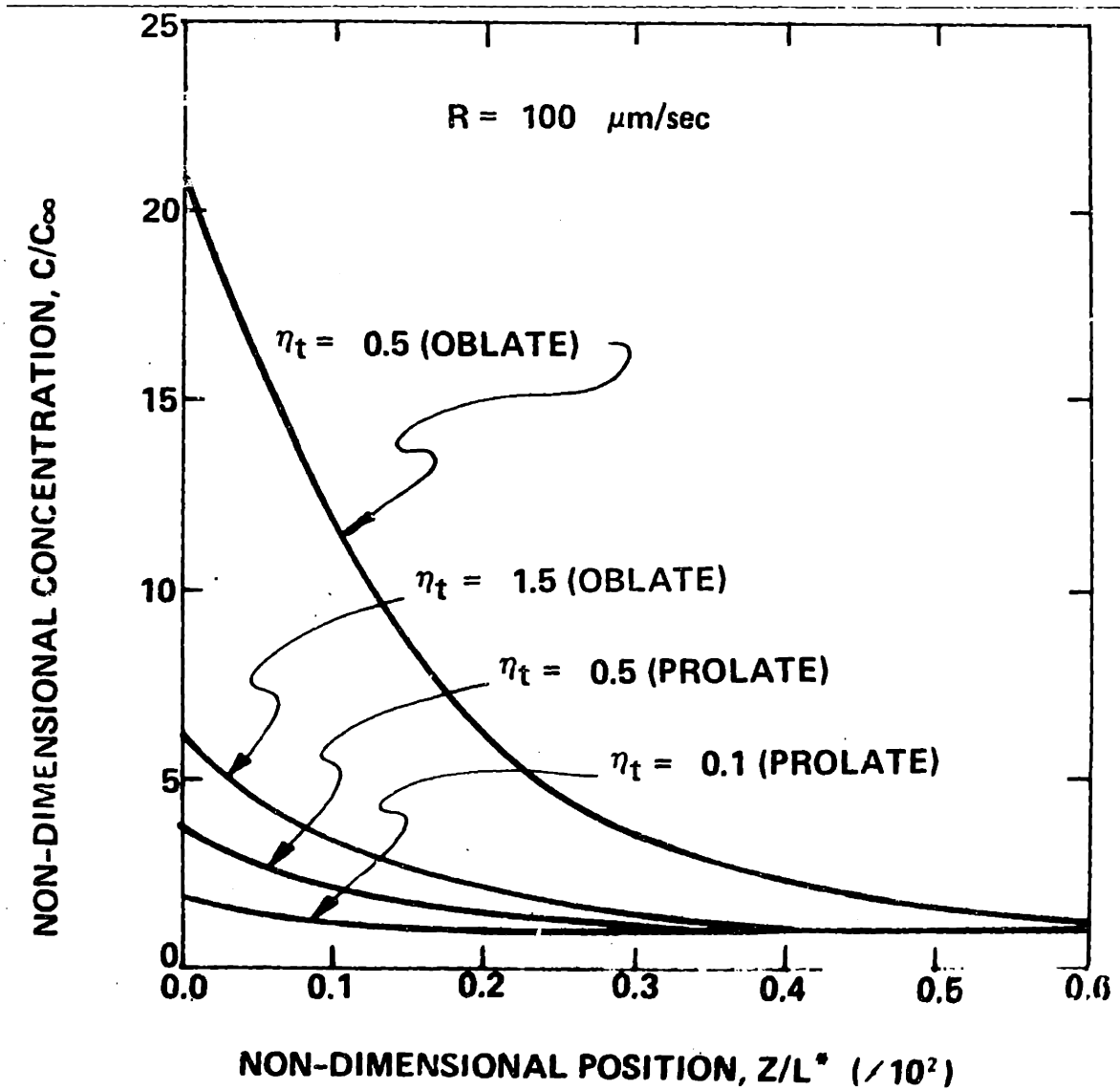


Figure (IV-12b) Relative Concentration Profiles for Constant Dendrite Width,  $R = 100 \mu\text{m}/\text{sec}$ .

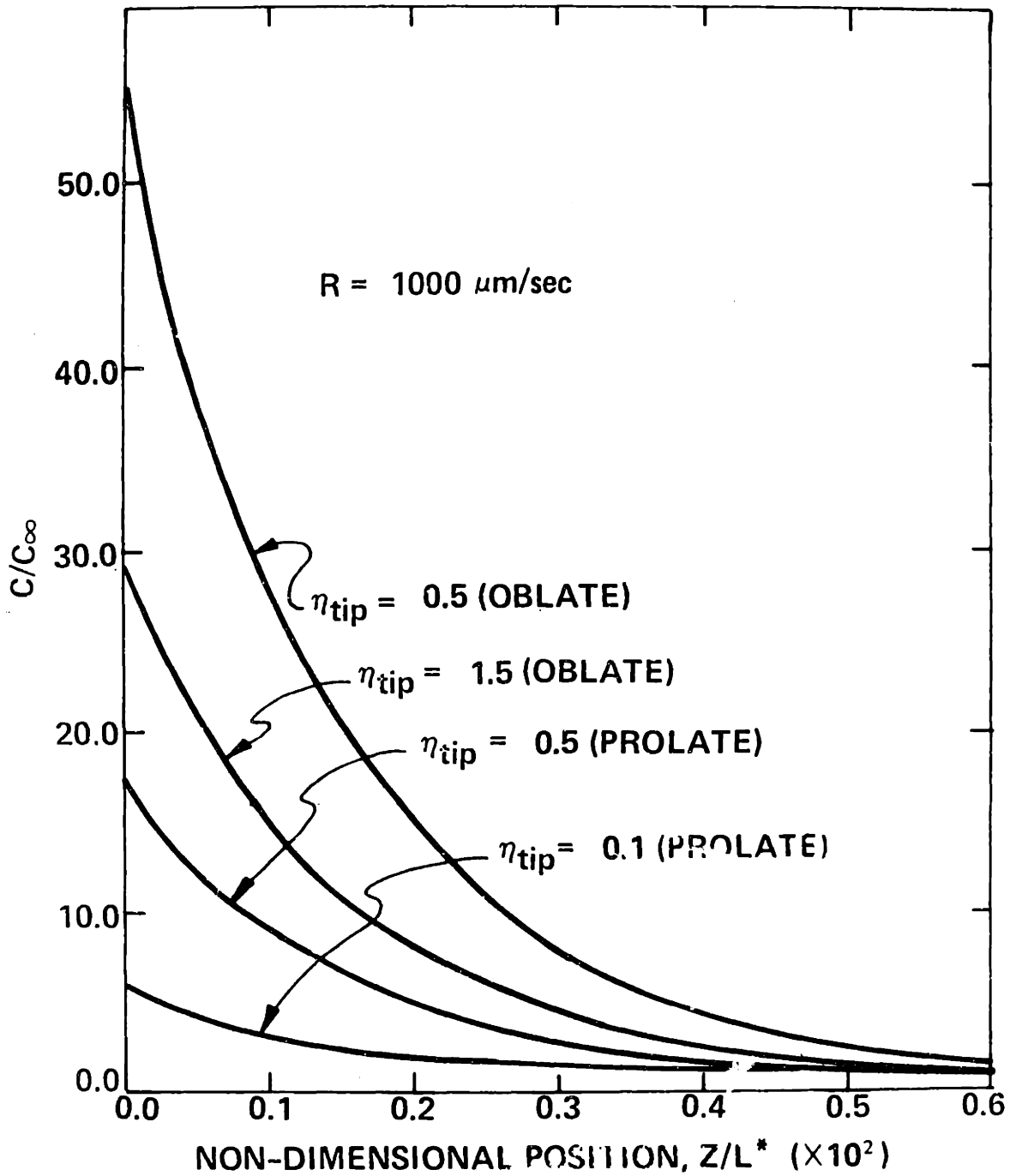
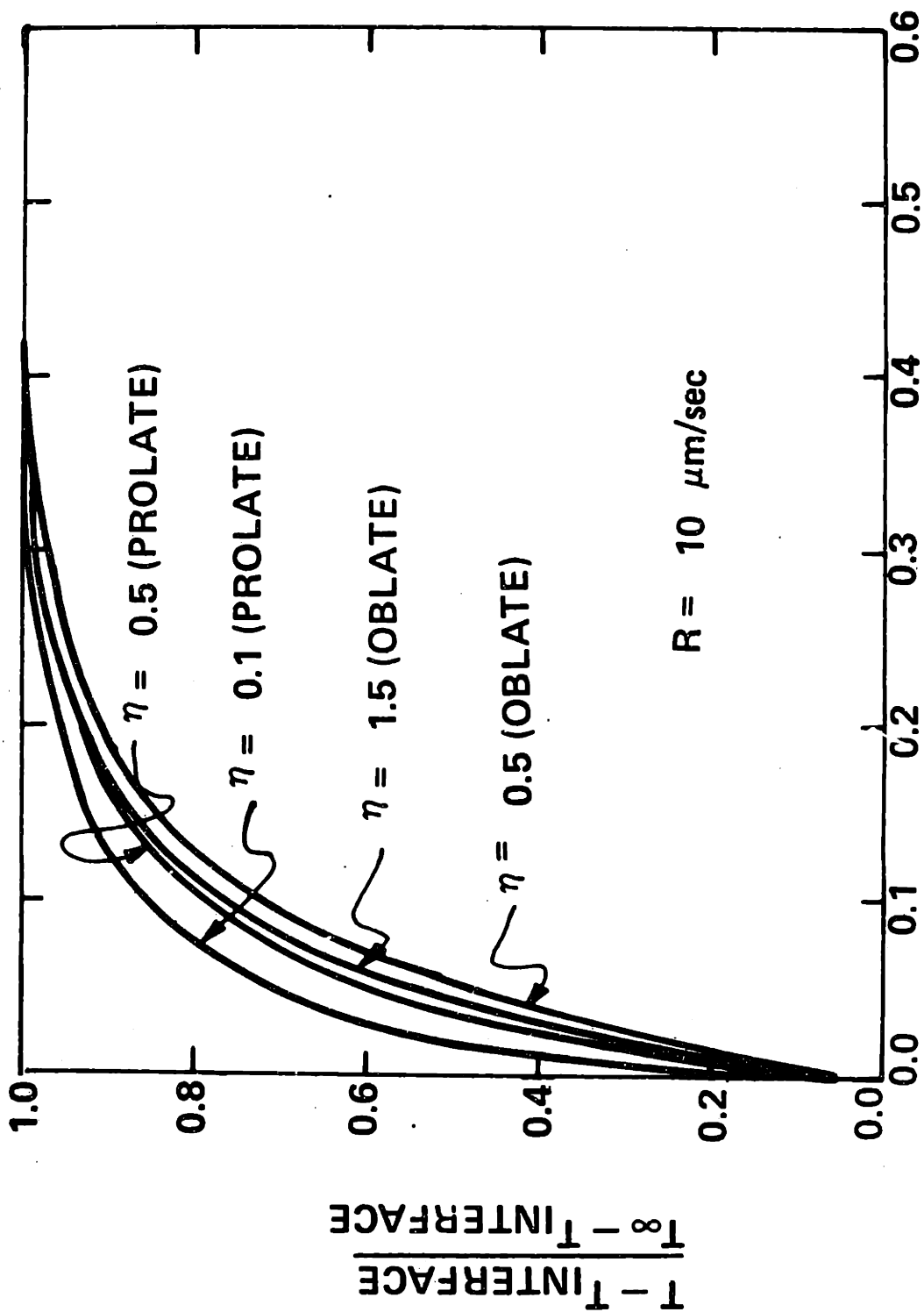


Figure (IV-12c) Relative Concentration Profiles for Constant Dendrite Width,  $R = 1000\mu\text{m}/\text{sec}$ .



NON-DIMENSIONAL POSITION,  $Z/L^* (\times 10^2)$

Figure (IV-13a) Relative Temperature Profiles for Constant Dendrite Width,  $R = 10 \mu\text{m}/\text{sec}$ .



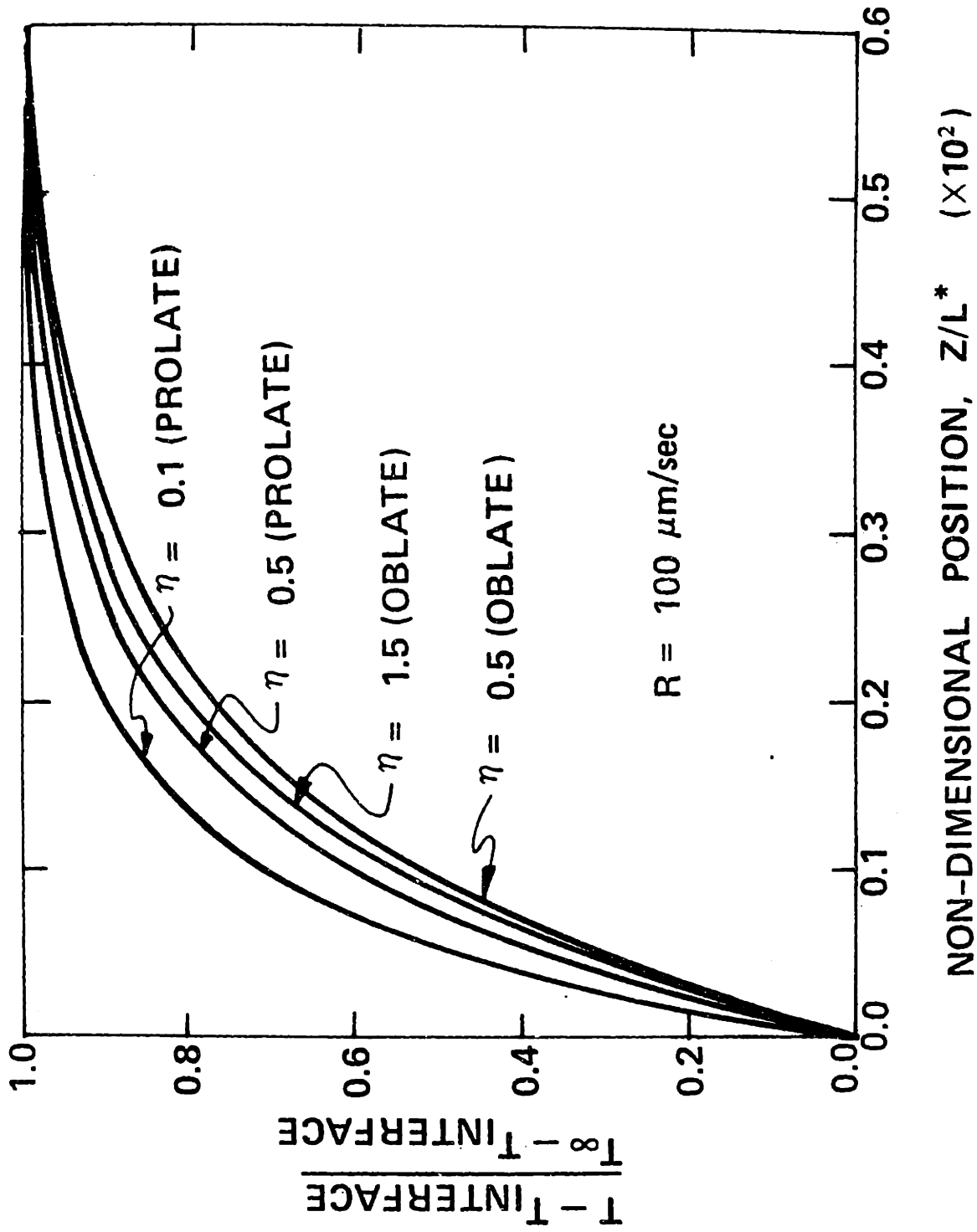


Figure (IV-13b) Relative Temperature Profiles for Constant Dendrite Width,  
 $R = 100\mu\text{m}/\text{sec}$ .

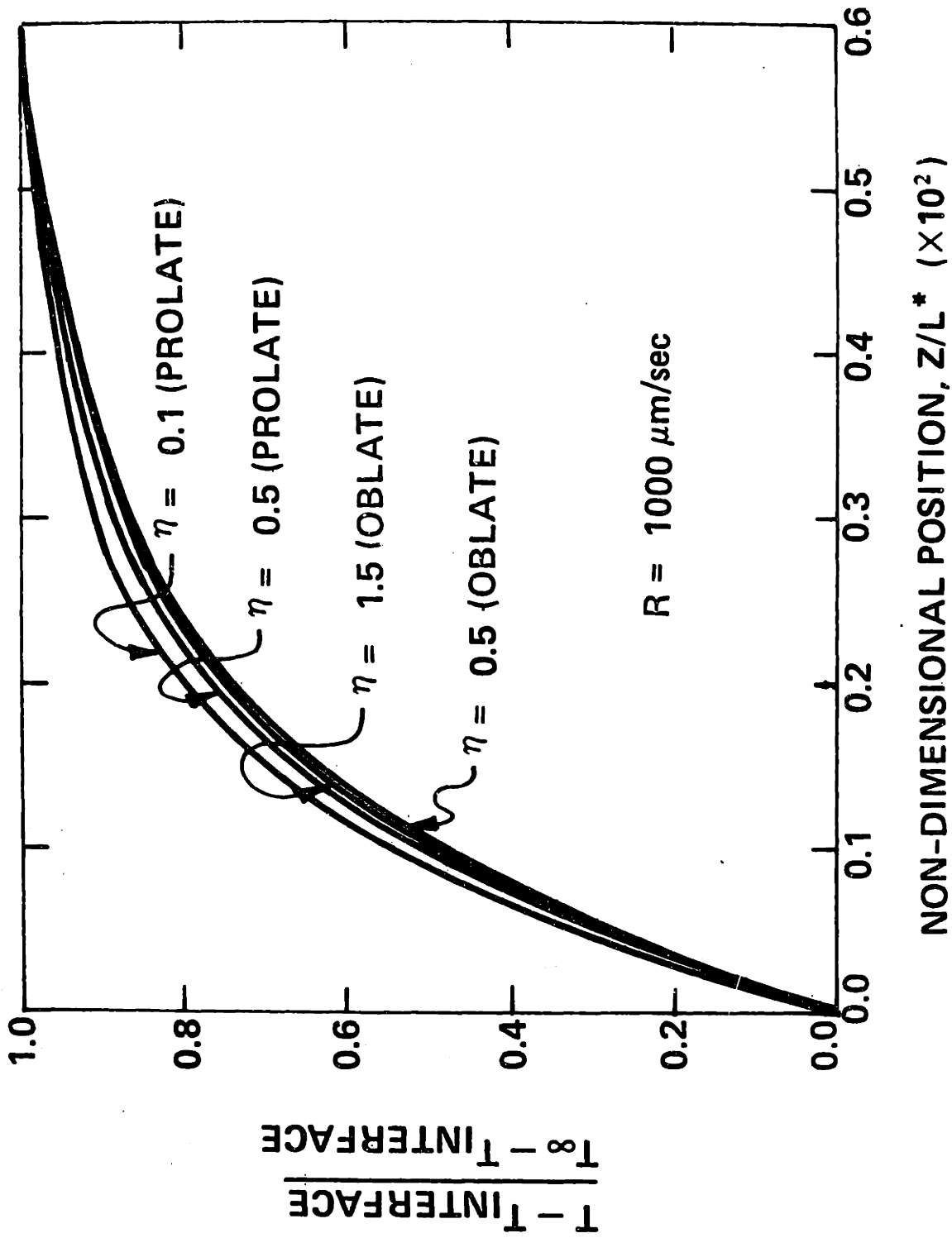


Figure (IV-13c) Relative Temperature Profiles for Constant Dendrite Width,  $R = 1000 \mu\text{m}/\text{sec}$ .

which just eliminates the instability. This configuration is the unique marginally stable shape, and applies as an optimization condition to steadily advancing dendrites.

The Mullins-Sekerka stability criterion [17] developed in Section III-D applies equally well to the present case. Since we are again considering the freezing of an aqueous solution, solute is completely rejected from the solid phase and the simplified M-S criterion applies:

$$-\frac{1}{2} (g_l + g_s) + mG_c < 0 \quad (\text{IV-74})$$

where  $g_l$  and  $g_s$  are the temperature gradients in the liquid and solid, respectively, weighted with respect to thermal conductivity. The term  $mG_c$  represents the gradient in liquidus temperature at the dendrite surface and may be evaluated by using the chain rule,

$$mG_c = \frac{d(T_E)}{dz} = \frac{d(T_E)}{dC_s} \frac{dC_s}{d\eta} \left(\frac{d\eta}{dz}\right) \quad (\text{IV-75})$$

where

$$\frac{dT_E}{dC} = b' + 2c' C_s (\eta_{\text{tip}})^2 + 3d' C_s (\eta_{\text{tip}})^3 \quad (\text{IV-76})$$

$$\frac{1}{a \sinh \eta} \quad \text{for the prolate case} \quad (\text{IV-77a})$$

$$\frac{d\eta}{dz} =$$

$$\frac{1}{a \cosh \eta} \quad \text{for the oblate case} \quad (\text{IV-77b})$$

and  $dC_s/d\eta$  is given by equation (IV-62) with boundary condition (IV-65). The derivative of liquidus temperature with concentration (equation (IV-76)) was obtained by differentiating equation (III-13). Substituting equations (IV-62) and (IV-65) into equation (IV-74), we have

$$mG_c = \frac{[b' + 2c'C_s(\eta_{tip}) + 3d'C_s(\eta_{tip})^2] f_p(\eta_{tip}, Pec_m) C_\infty Pec_m \sinh(\eta_{tip})}{a \sinh \eta_{tip} (f_p(Pec_m, \eta_{tip}) - Pec_m \sinh \eta_{tip} g_p(Pec_m, \eta_{tip}))} \quad (\text{IV-78a})$$

for the prolate case, and

$$mG_c = \frac{[b' + 2c'C(\eta_{tip}) + 3d'C(\eta_{tip})^2] f_o(\eta_{tip}, Pec_m) C_\infty Pec_m \cosh(\eta_{tip})}{a \cosh \eta_{tip} (f_o(Pec_m, \eta_{tip}) - Pec_m \cosh \eta_{tip} g_o(Pec_m, \eta_{tip}))} \quad (\text{IV-78b})$$

for the oblate case, where  $C(\eta_{tip})$  is given by equations (IV-62) for the two cases.

The thermal gradients may be evaluated by using equation (IV-62) with boundary conditions (IV-68) - (IV-71),

$$\frac{2K_\ell}{K_s + K_\ell} \frac{(T(n_{tip}) - T_\infty)}{g_o(Pec_\ell, n_{tip})} \frac{f_o(n_{tip}, Pec_\ell)}{a \cosh n_{tip}} \text{oblate} \quad (IV-79b)$$

$$g_\ell = \frac{2K_\ell}{K_s + K_\ell} \frac{(T(n_{tip}) - T_\infty)}{g_p(Pec_\ell, n_{tip})} \frac{f_p(n_{tip}, Pec_\ell)}{a \sinh n_{tip}} \text{prolate} \quad (IV-79b)$$

$$\frac{2K_s}{K_s + K_L} \left\{ \frac{K_{prolate}^{solid} f_p(n_{tip}, Pec_s)}{a \sinh n_{tip}} \right\} \text{prolate} \quad (IV-80a)$$

$$g_s = \frac{2K_s}{K_s + K_L} \left\{ \frac{K_{oblate}^{solid} f_o(n_{tip}, Pec_s)}{a \sinh(n_{tip})} \right\} \text{oblate} \quad (IV-80b)$$

where  $T(n_{tip})$  is given by equation (III-i3).

The final form of the M-S criterion may be obtained by substituting into equation (IV-74). After simplification, we have

$$\frac{\rho_s}{2(K_\ell + K_s)} L_{HF} + \frac{2C_\ell(T_\infty - T(n_{tip}))}{Pec_\ell \frac{\sinh n_{tip} g_p(n_{tip}, Pec_\ell)}{f_p(n_{tip}, Pec_\ell)}} + \quad (IV-81a)$$

$$\frac{C_\infty}{D_m} \left( \frac{dT_E}{dC_s} \right) \frac{1}{1 - \frac{Pec_m \sinh n_{tip} g_p(n_{tip}, Pec_m)}{f_p(n_{tip}, Pec_m)}} \geq 0$$

for the prolate case, and

$$\frac{\rho_s}{2(K_l + K_s)} \left\{ L_{HF} + \frac{2C_l (T_\infty - T(n_{tip}))}{Pec_l \frac{\cosh n_{tip} g_o(n_{tip}, Pec_l)}{f_o(n_{tip}, Pec_l)}} \right\} + \quad (IV-81b)$$

$$\frac{C_\infty}{D_m} \left( \frac{dT_E}{dC_s} \right) \frac{1}{1 - \frac{Pec_m \cosh n_{tip} g_o(n_{tip}, Pec_m)}{f_p(n_{tip}, Pec_m)}} \geq 0$$

for the oblate case, where  $dT_E/dC_s$  is given by equation (IV-76),  $T(n_{tip})$  is given by equation (III-13) and  $C(n_{tip})$  is given by equations (IV-62).

Steady dendrite tips are marginally stable, so to apply equations (IV-81) as an optimization criterion would require use of the "equals" sign.

#### IV-E Spheroidal-Equilibrium Matching Procedure

The equilibrium solution is used (for a particular basal temperature gradient) from the basal plane to a point located back from the dendrite tips at  $z^* = z_{change}$  and  $f_s = f_{end}$  (see Figure IV-3). At this point, the assumptions governing the equilibrium region reach their limit. Similarly, the spheroidal coordinate solution will be used to describe

the transport in the liquid ahead of the dendrite tips. There is an additional small region, not described by either the equilibrium or spheroidal systems, where the iso-potential surfaces transform from spheroidal to planar. The transport is two dimensional but non-spheroidal in this volume and will not be treated in the present work. It will be shown, however, that this region is small enough in extent to have a negligible effect on any transport process being considered.

The mathematics for both solution schemes have been carefully developed in sections B and C, but the overall solution still requires calculation of several variables. In the equilibrium region, the basal temperature gradient  $dT/dz^*$ , must be determined as well as the changeover position  $z_{\text{change}}$  (or equivalently  $f_{\text{end}}$ ). In the spheroidal region, the pointedness of the dendrite tip ( $\eta_{\text{tip}}$ ), the characteristic dimension  $a$  and the axis displacement  $\delta$  need to be calculated. In short, a particular equilibrium-spheroidal combination is sought which is compatible, unique, and satisfies the applicable boundary conditions.

IV-E.1 Geometric Compatibility

From simple geometric considerations, the value of  $f_s$  at  $z_{\text{change}}$  must equal the value of  $f_s$  described by the spheroid at the tip surface. In addition, no "points" may exist on the dendrite surface, so the slope  $df_s/dz$  must match as well. Using equations (IV-48), we may mathematically state these criteria as

$$f_{\text{end}} = \left(\frac{a}{L_D}\right)^2 \cosh^2 \eta_{\text{tip}} - \delta^2 \left(\frac{L^*}{L_D}\right) \coth^2 \eta_{\text{tip}} \quad (\text{IV-82a})$$

$$\left(\frac{df}{dz^*}\right)_{z=z_{\text{change}}} = -2\delta \left(\frac{L^*}{L_D}\right)^2 \coth^2 \eta_{\text{tip}} \quad (\text{IV-82b})$$

for the oblate case, and

$$f_{\text{end}} = \left(\frac{a}{L_D}\right)^2 \sinh^2 \eta_{\text{tip}} - \delta^2 \left(\frac{L^*}{L_D}\right)^2 \tanh^2 \eta_{\text{tip}} \quad (\text{IV-82c})$$

$$\left(\frac{df}{dz^*}\right)_{z=z_{\text{change}}} = -2\delta \left(\frac{L^*}{L_D}\right)^2 \tanh^2 \eta_{\text{tip}} \quad (\text{IV-82d})$$

Equations (IV-82) are two independent equations relating the five unknown quantities  $f_{\text{end}}$ ,  $\left(\frac{df}{dz^*}\right)_{z_{\text{change}}}$ ,  $a$ ,  $\delta$  and  $\eta_{\text{tip}}$ .



### IV-E.2 Tip Stability

In the argument presented in Section D, it was shown that the tips of steadily advancing dendrites are marginally stable. Equations (IV-81) therefore apply as matching criteria. The reader should note that either equation (IV-81a) or equation (IV-81b) applies to a particular situation but not both simultaneously. The mathematics describing a particular optimization problem will determine whether the dendrite tips are prolate or oblate spheroids. For example, if for particular values of  $\left(\frac{dT}{dz^*}\right)_{z^*=0}$  and  $f_{end}$ , the oblate spheroidal solution (equation (IV-81b)) yields an unstable tip for any value of  $\eta_{tip}$ , the tip geometry would be described by a prolate spheroid.

### IV-E.3 Thermal Matching Conditions

In any physical system, there are two thermodynamic conditions that must be satisfied: the temperature and heat flux (in the absence of energy sources or sinks) must be continuous. In the present case, however, exact compliance with these restrictions is impossible since the temperature fields in the spheroidal and the equilibrium regions are geometrically different (see Figure IV-3). We will satisfy the thermal matching conditions only on the average over the cross-section at  $z = z_{change}$ .

The spheroidal heat flux prediction at  $z = z_{\text{change}}$  has three components: the convective energy input from the free field, the energy needed to solidify the tip region of the dendrite cap, and the energy needed to change the temperature of the solid from the tip temperature to the temperature at  $z = z_{\text{change}}$ . The energy needed to change the temperature of the solid is negligible compared to the other terms since the thermal mass of the solid is small and the temperature difference from the dendrite tip to  $z = z_{\text{change}}$  is similarly small. The resulting heat flux expression is given by

$$h_{\text{spheroidal}} = R \rho_s L_{\text{HF}} f_{\text{end}} + R \rho_l C_l (T_{\infty} - T(\eta_{\text{tip}})) . \quad (\text{IV-83})$$

Setting this equal to the equilibrium heat flux prediction: we have (after simplification)

$$\left. \left( \frac{dT}{dz^*} \right) \right|_{z^*=z_{\text{change}}} = \frac{R \rho_l (f_{\text{end}} L_{\text{HF}} + C_l (T_{\infty} - T(\eta_{\text{tip}}))) L^*}{(f_{\text{end}} K_s + (1-f_{\text{end}}) K_l)} . \quad (\text{IV-84})$$

A plot of the isotherms in the tip region is shown in Figure (IV-14). The spheroidal temperature field changes in the transverse direction at  $z = z_{\text{change}}$ , with the lowest temperature at the dendrite core and the highest at the dendrite surface. It is clear from Figure (IV-14) that the actual

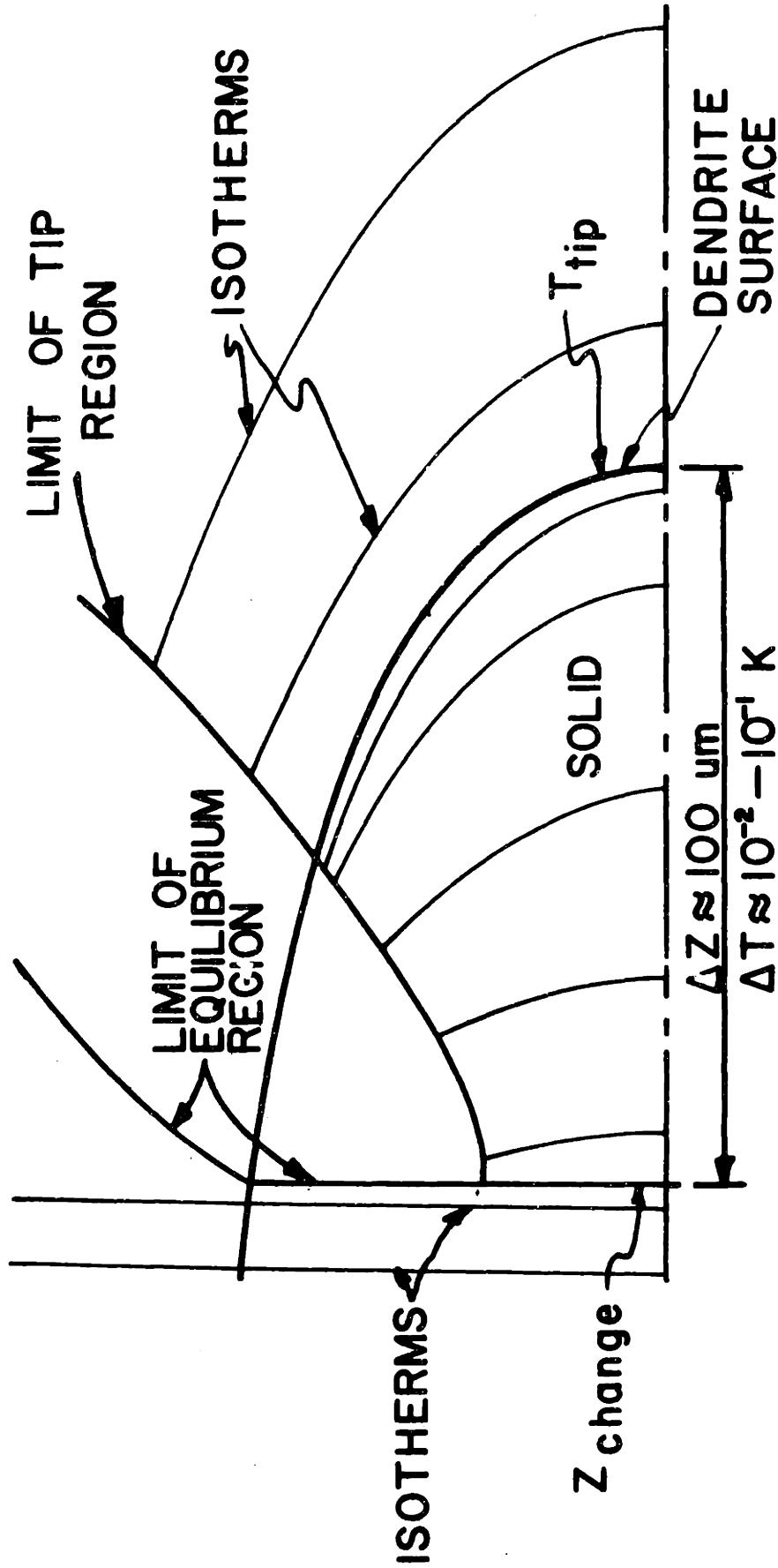


Figure (IV-14) Dendrite Tip Region Isotherms.

isotherm that coincides with the changeover line is at a temperature between  $T(n_{tip})$  and the core temperature. If the temperature difference between the dendrite surface and the core is sufficiently small, our "matching" temperature may be assumed to be the tip temperature without appreciable error. An estimate of this temperature difference is given by the temperature gradient multiplied by the distance from the dendrite tip to the spheroidal origin  $\Delta z'$ . The temperature gradient in the solid near the tip is approximately,

$$\left(\frac{dT}{dz}\right)_{\text{tip region}} \approx \frac{R \rho_s L_{HF}}{K_s} \quad (\text{IV-85})$$

and  $\Delta z'$  is at most the width of the dendrite ( $\sim 100 \mu\text{m}$ ). Using the data listed in Table III-2, we have

$$\Delta T \sim 10^{-1} - 10^{-2} (\text{K}) .$$

It is within the limits of accuracy of this work to match the temperature at  $z_{\text{end}}$  generated by the equilibrium solution to the dendrite surface temperature. With this condition, the temperature matching criterion becomes

$$T(z=z_{\text{end}}) = T(n_{tip}) . \quad (\text{IV-86})$$

This simplified criterion will result in a 0.1K error, at most.

Equations (IV-81), (IV-82), and (IV-86) comprise a system of five equations in five unknowns which may be solved numerically to find the basal temperature gradient and tip geometry as a function of the independent parameters.

#### IV-E.4 Method of Solution

Of the five unknowns mentioned above, only three are independent. It is mathematically equivalent to choose any three of the five variables, so the basal temperature gradient ( $dT/dz^*$ ), the solid fraction at  $z_{\text{change}}$  ( $f_{\text{end}}$ ) and the tip pointedness ( $\eta_{\text{tip}}$ ) are chosen arbitrarily.

A block diagram of the solution scheme is shown in Figure (IV-15). Mathematically the problem is to find the solution vector of a system of non-linear algebraic equations using a one-point iteration scheme. The procedure is started by guessing values for the three variables. The equilibrium equations are then integrated from the basal plane to a point where  $f_s$  equals the initial guess. Using this value of  $f_{\text{end}}$  and its first derivative (from the equilibrium solution), the spheroidal parameters  $a$  and  $\delta$  are calculated from equations (IV-81). Similarly, with the assumed value of  $\eta_{\text{tip}}$ , the

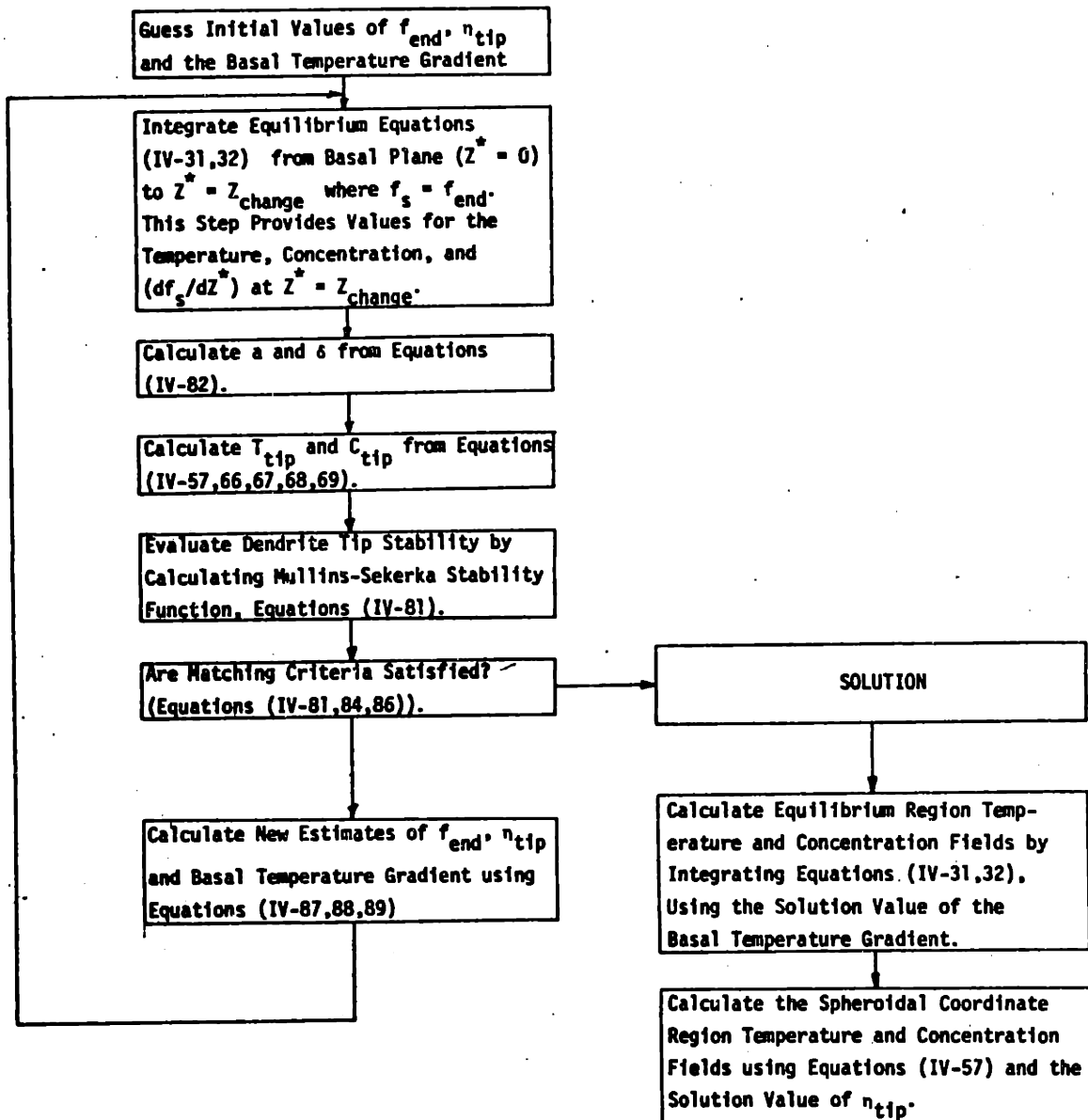


Figure (IV-15) Block Diagram of Overall Solution Scheme

concentration and temperature are calculated from equations (IV-62) and (IV-68) - (IV-71), and the tip stability is evaluated from equations (IV-81). If the matching criteria are not satisfied a new guess of the solution vector is calculated from

$$n_{tip}^{new} = - \epsilon_1 * \text{EXP}(n_{tip}^{old}) * M-S + n_{tip}^{old} \quad (\text{IV-87})$$

$$\begin{aligned} \left(\frac{dT}{dz^*}\right)_{z^*=0}^{new} = \epsilon_2 \left( \left(\frac{dT}{dz^*}\right)_{equil}^{old} - \left(\frac{dT}{dz^*}\right)_{spher\ z=z_{change}}^{old} \right) \\ + \left(\frac{dT}{dz^*}\right)_{z^*=0}^{old} \end{aligned} \quad (\text{IV-88})$$

and

$$f_{end}^{new} = \epsilon_3 [T_{equil}(z_{change}^*) - T(n_{tip})] + f_{end}^{old} \quad (\text{IV-89})$$

where  $\epsilon_1$ ,  $\epsilon_2$  and  $\epsilon_3$  are scaling factors and the superscripts "old" and "new" refer to the  $i^{th}$  and  $(i+1)^{th}$  iterations respectively. These three equations are simply "correcting equations which change the value of the variable most sensitive to the quantity mismatched. The "new" solution vector is used to start the procedure over again and the process is continued until the actual solution vector is obtained, within some

accuracy level.

The reader should note that the optimization procedure does not depend on the interface speed  $R$ . The characteristic dimension of the spheroid,  $a$ , is proportional to the dendrite spacing (see Appendix II) which is in turn proportional to  $1/R$ . When  $a$  is multiplied by  $R/D_i$  to obtain the Peclet number, the  $R$ 's cancel and the interface speed dependence disappears.

#### IV.F RESULTS

Plots of the relative tip concentration, tip temperature, basal temperature gradient and dendrite length are shown in Figures (IV-16) - (IV-19). Two independent parameters are needed to specify each freezing condition: the free-field temperature and the free-field concentration (interface speed dependence has been eliminated by the similarity transformations (equation IV-29)). An equivalent way of expressing the temperature boundary condition is by the relative free-field superheat  $(\Delta T)_S$  which is defined by

$$(\Delta T)_S = T_\infty - T_E(C_\infty) \quad (\text{IV-90})$$

For solutions initially at the freezing temperature,  $\Delta T$  is zero and the maximum superheat considered is 32K.



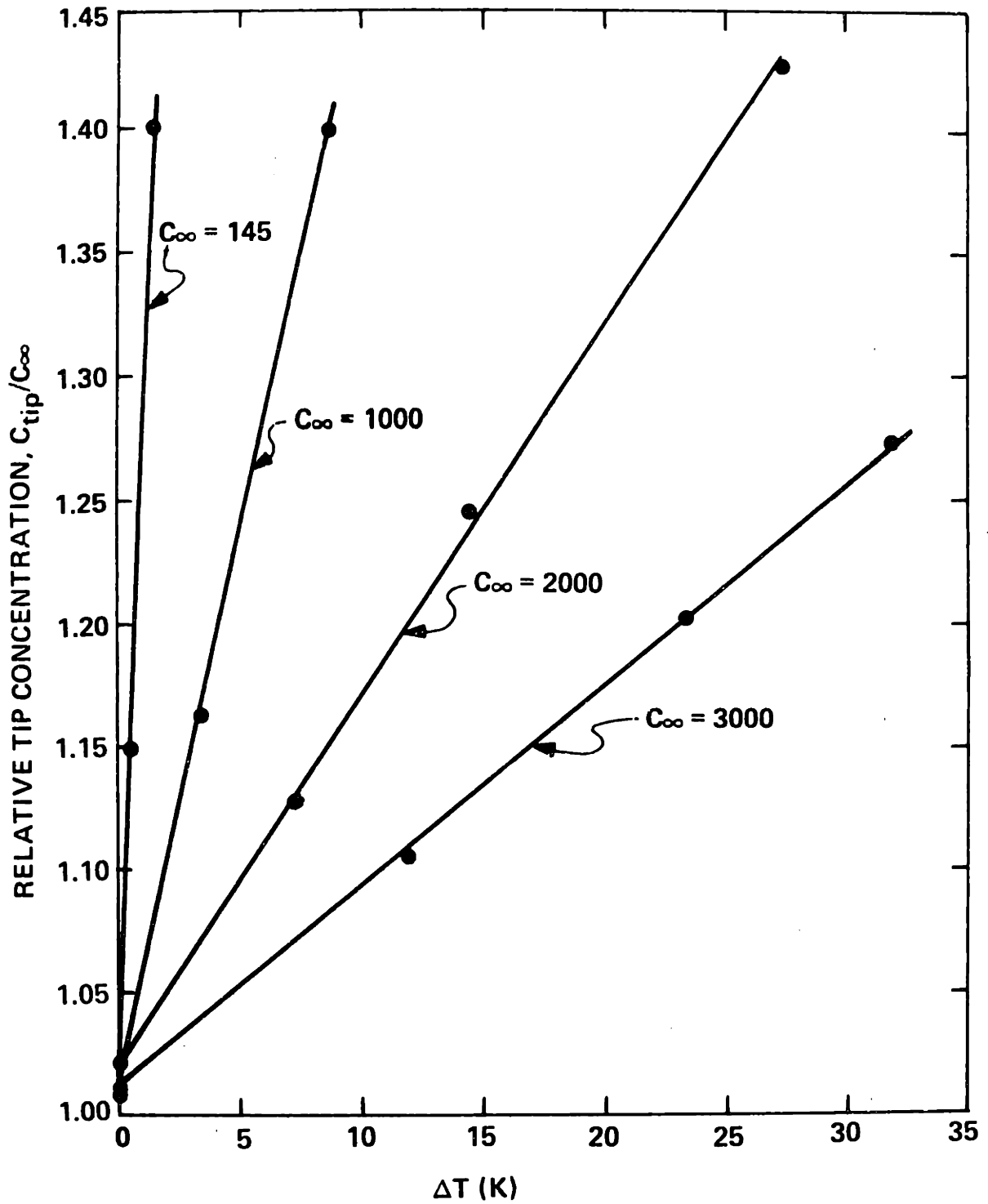


Figure (IV-16) Relative Tip Temperature Versus Free-Field Superheat.

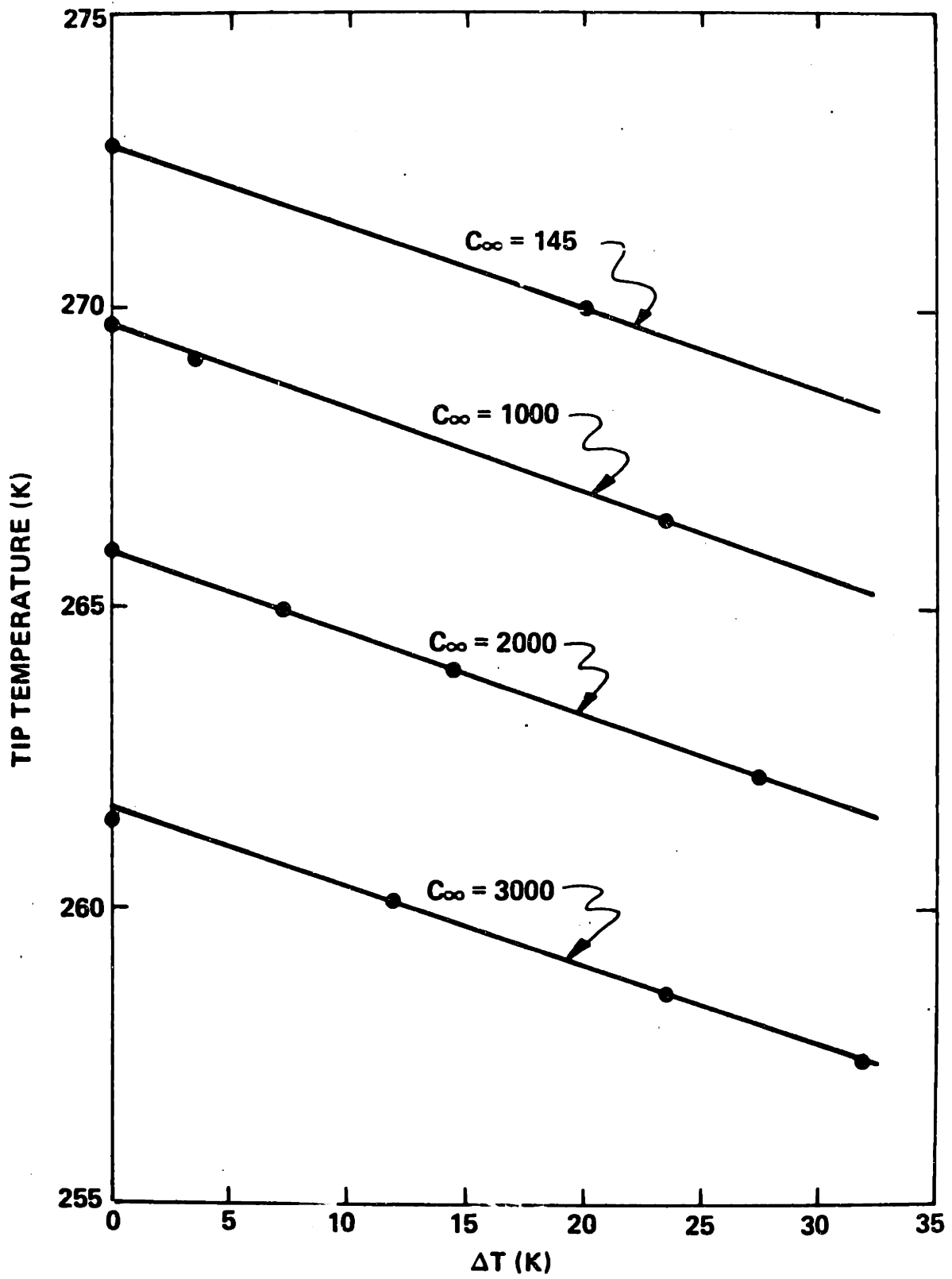


Figure (IV-17) Dendrite Tip Temperature Versus Free-Field Superheat.

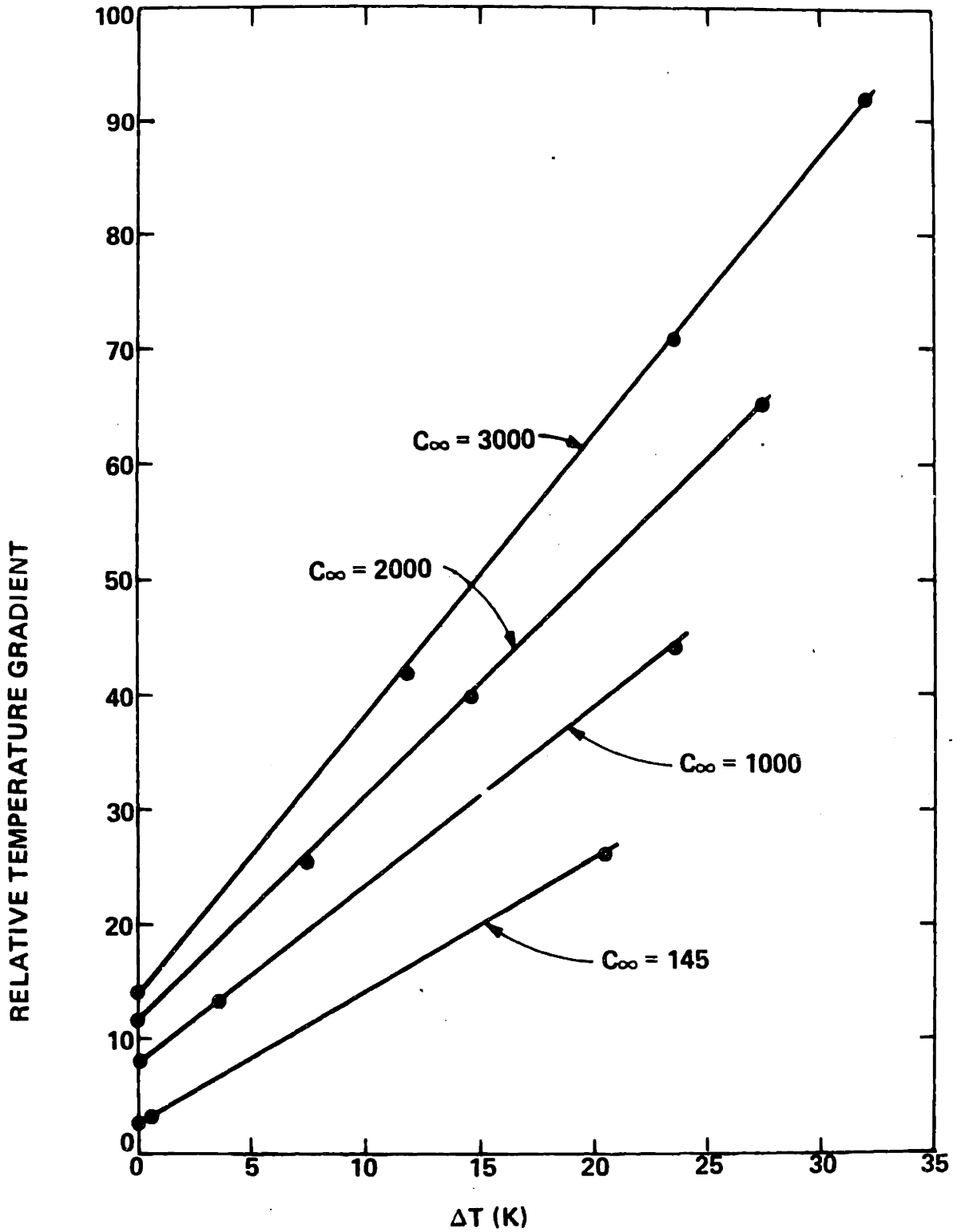


Figure (IV-18) Basal Temperature Gradient Versus Free-Field Superheat.

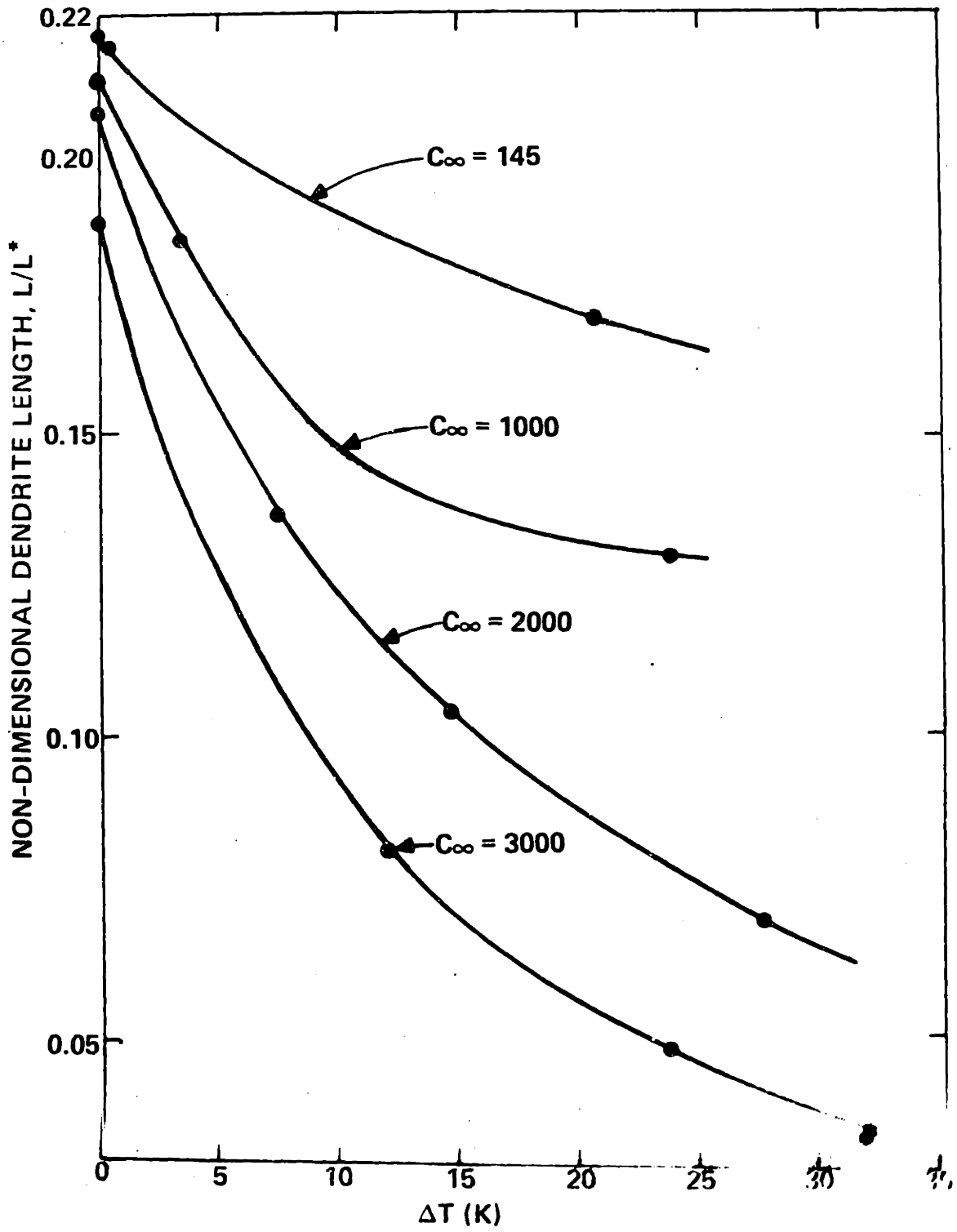


Figure (IV-19) Relative Dendrite Length Versus Free-Field Superheat.

The relative basal temperature gradient is defined by

$$\Delta \left( \frac{dT}{dz^*} \right)_{z^*=0} = \left( \frac{dT}{dz^*} \right)_{z^*=0} - \left( \frac{dT}{dz^*} \right)_{z^*=0, \text{ solidification only}} \quad (\text{IV-91})$$

This quantity represents the basal heat flux required in addition to that required for solidification only (i.e., latent heat only). As a particle goes through the solidification zone, it undergoes two distinct energy interactions in addition to the removal of the latent heat of fusion. First, the particle is reduced from the free-field temperature to the dendrite tip temperature. The heat flux associated with this interaction is given by

$$\delta \dot{E}_1 = R \rho_l C_l (T_\infty - T(\eta_{\text{tip}})) (\delta f_s) \quad (\text{IV-92})$$

where  $\delta f_s$  is an incremental change in solid fraction representing the infinitesimal particle. This quantity is very nearly proportional to  $T_\infty$ , since the tip temperature change is only a few degrees (see Figure (IV-17)). The second interaction is the cooling of the particle from the tip temperature to the freezing temperature as liquid, and then from the freezing temperature to the basal temperature as solid. This interaction is given by

$$\delta E_2 = (\delta f_s) R(\rho_l C_l T(\eta_{tip}) - T_E) + \rho_s C_s (T_E - T_{eut}). \quad (IV-93)$$

The freezing temperature depends on the interface concentration at the point where the particle is solidified and varies with the dendrite shape and free-field conditions. The nearly constant slope of the basal heat flux is due to the first energy interaction, (equation IV-92) since  $\Delta T$  is proportional to  $T_\infty$ . The small difference in slopes at different concentrations is caused by progressively higher tip temperature depression at higher free-field concentrations which increase the effect of  $\delta E_1$ . The second type of energy interaction causes the positive value of the temperature gradient at  $\Delta T = 0$ . Although this quantity is expected to vary with free-field concentration, its magnitude is too small to affect the linearity of the temperature gradient plots.

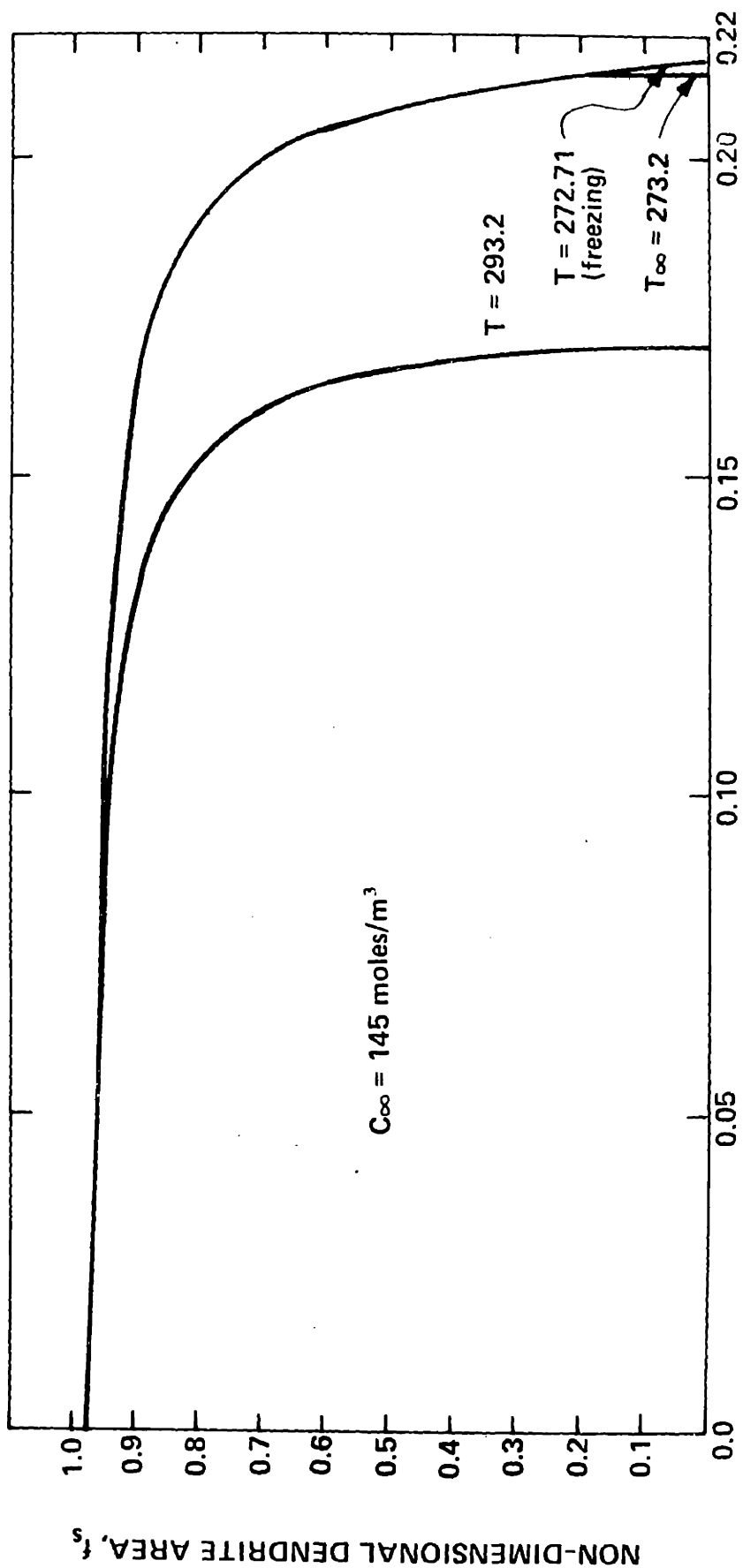
The relative tip concentration, shown in Figure IV-16, exhibits a sharp increase with increasing free-field superheat. Increasing the superheat increases the liquid phase heat flux at the dendrite tip, which by equation (IV-74) makes the tip more stable. The resulting "bluntness" of the dendrite tips at marginal stability allows a higher tip concentration. Note that the  $\Delta T = 0$  intercept is at an interface concentration at about  $C_\infty$ , indicating that an aqueous solution initially at the freezing temperature will exhibit very long, sharply pointed

dendrites.

Because equilibrium is assumed everywhere on the dendrite surface, the tip temperature (Figure (IV-17)) follows the trend of the tip concentration. An increase in the tip concentration causes the tip temperature to decrease by equation (III-13). Since the interface concentration is nearly the free field value at  $\Delta T = 0$ , the tip temperature at  $\Delta T = 0$  is nearly the freezing temperature at the free-field concentration. This accounts for the different intercepts at  $\Delta T = 0$  for different concentrations.

The relative dendrite length also decreases sharply with increasing superheat. With the tip temperature decreasing with increasing  $\Delta T$ , the temperature matching condition imposed by equation (IV-86) requires a progressively lower temperature at the end of the equilibrium solution ( $z^* = z_{\text{change}}$ ). Since the temperature in the equilibrium zone increases with distance from the basal plane, the dendrite stalks must be shorter (smaller  $z^*$ ) to match the equilibrium end temperature with a lower tip temperature.

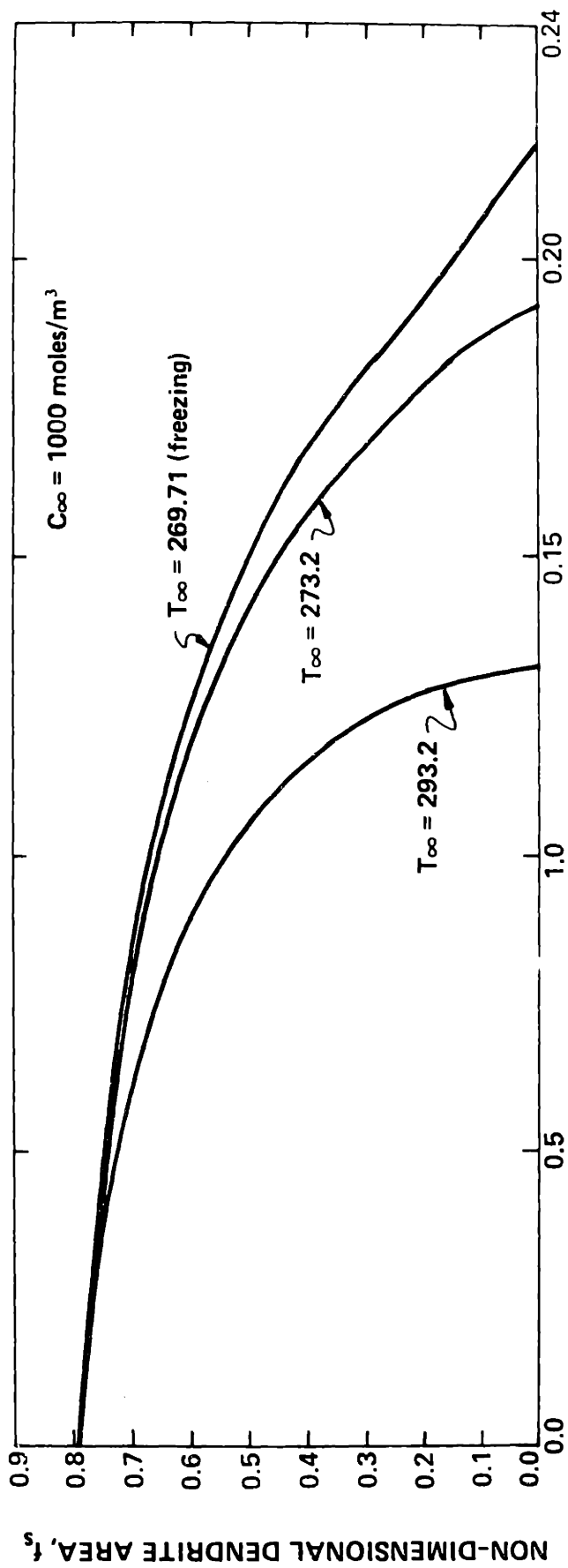
The dendrite shape profiles are shown in Figure (IV-20). The portion of the dendrite forward of the vertical slash mark is described by the appropriate spheroid, and the portion behind the mark is generated by the equilibrium solution. The profiles



NON-DIMENSIONAL AXIAL POSITION,  $Z^*$

Figure (IV-20a) Overall Dendrite Shape Profiles,  $C_\infty = 145 \text{ moles/m}^3$ .





NON-DIMENSIONAL AXIAL POSITION,  $Z^*$   
Figure (IV-20b) Overall Dendrite Shape Profiles,  $C_\infty = 1000 \text{ moles/m}^3$ .

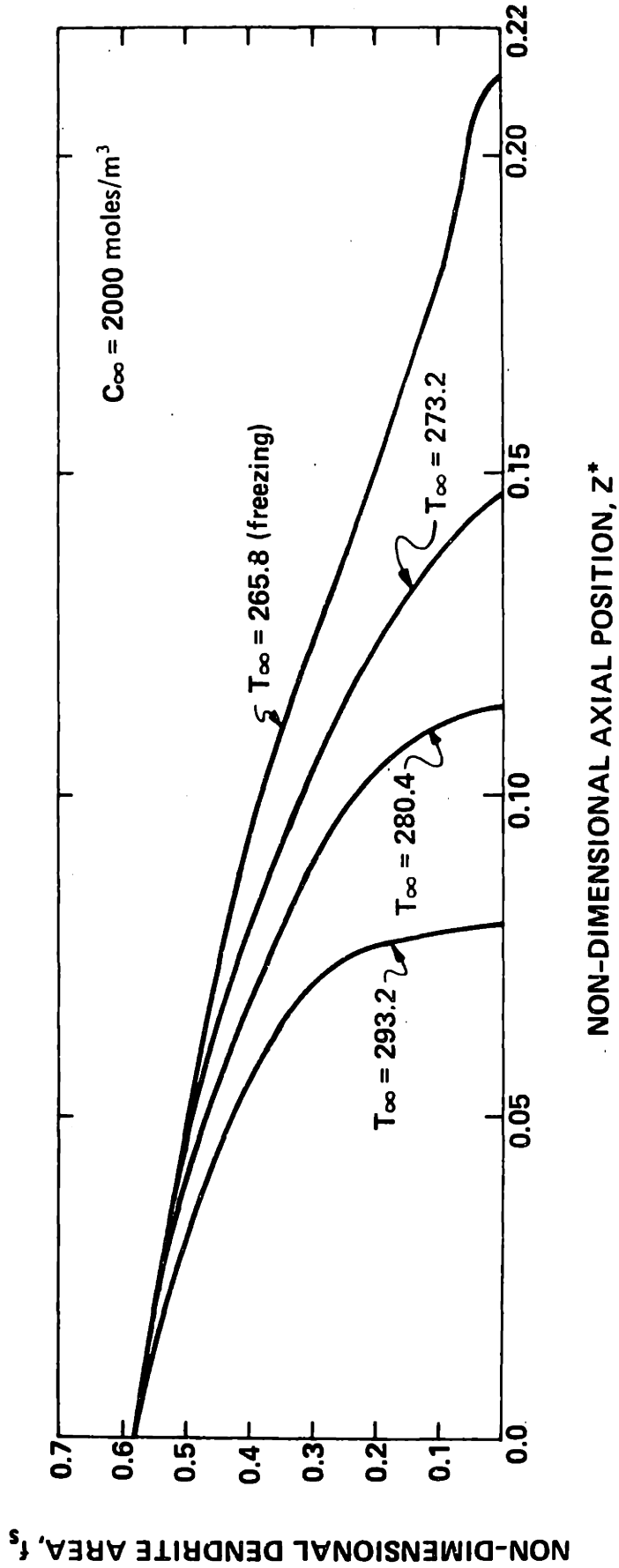


Figure (IV-20c) Overall Dendrite Shape Profiles,  $C_\infty = 2000 \text{ moles/m}^3$ .

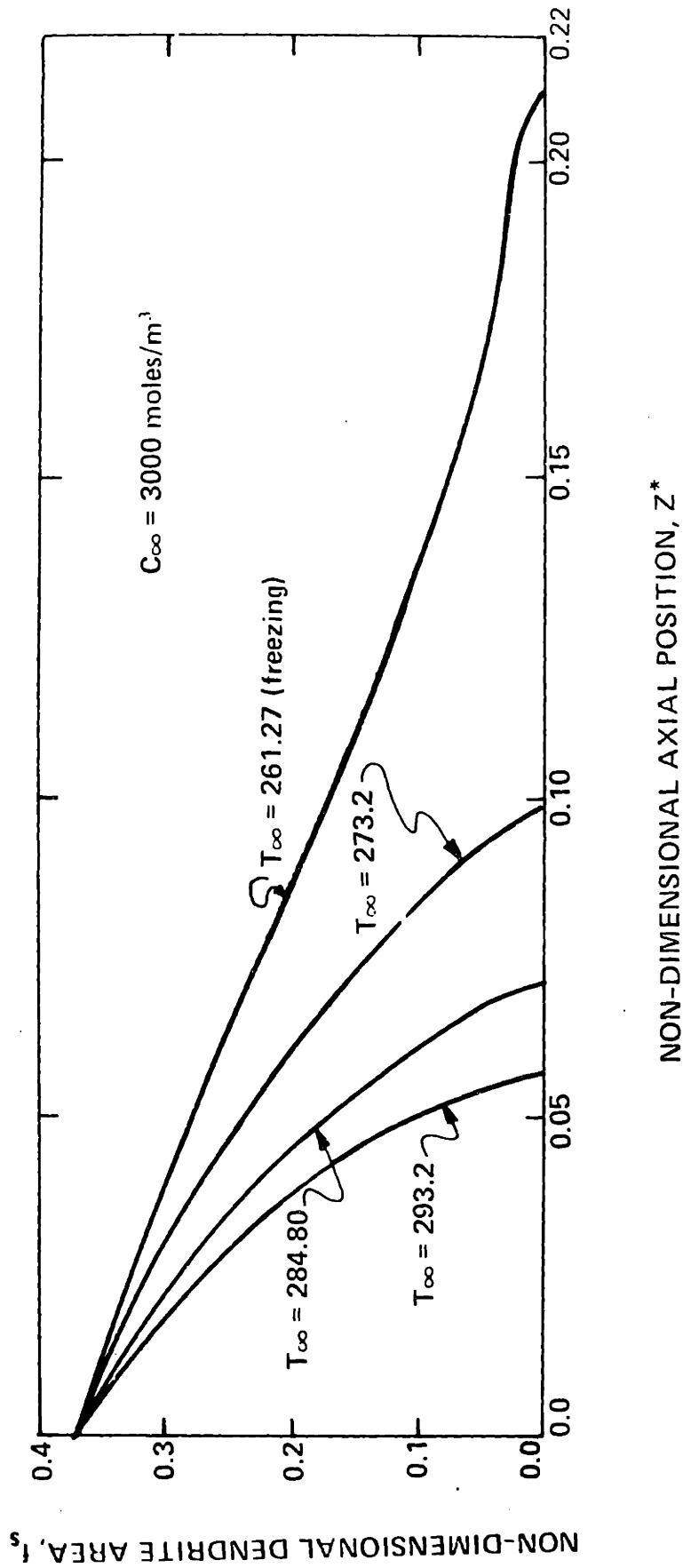
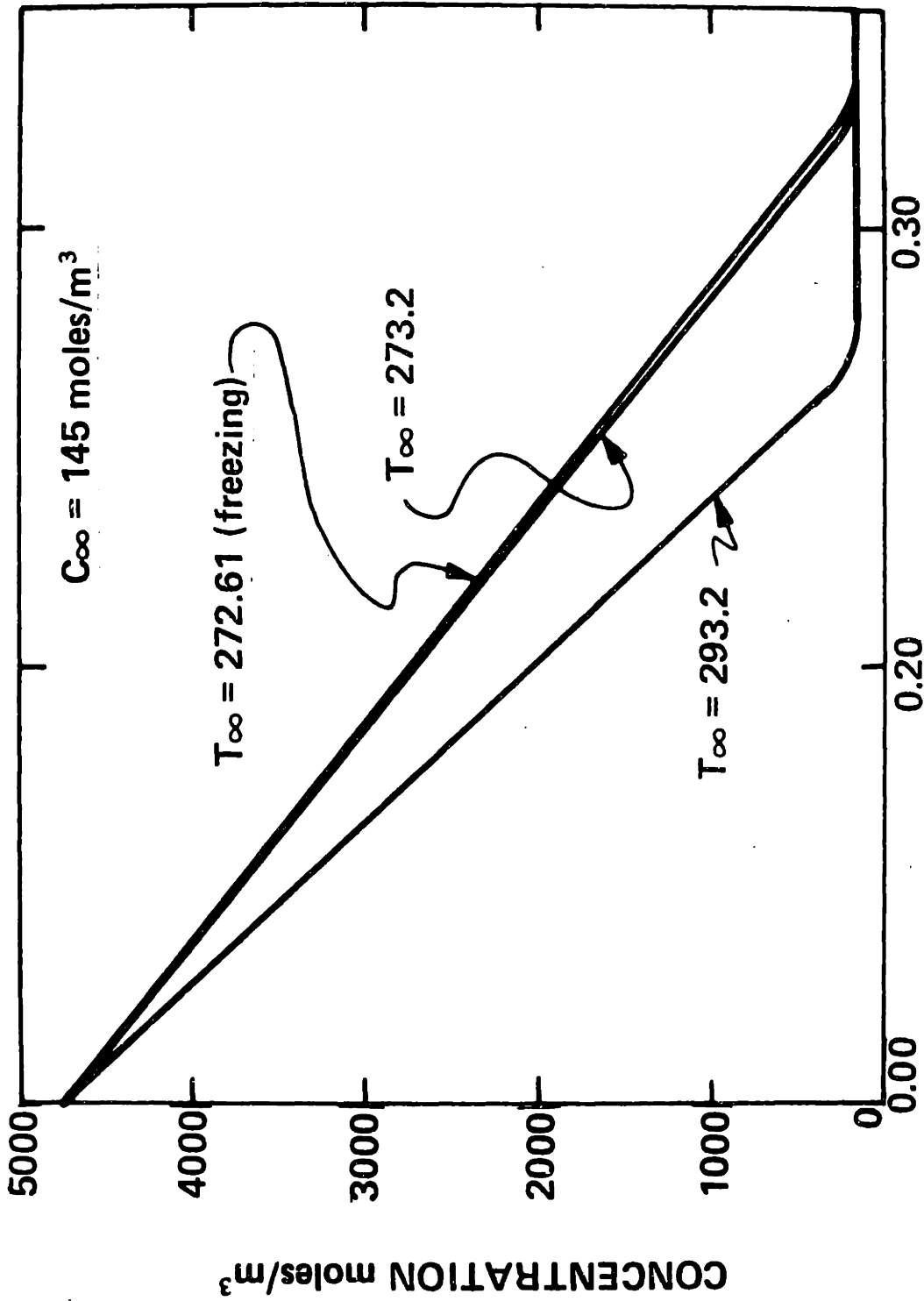


Figure (IV-20d) Overall Dendrite Shape Profiles,  $C_\infty = 3000$  moles/m<sup>3</sup>.

for the  $C_{\infty} = 145 \text{ moles/m}^3$  case are all extremely blunt for all free-field temperatures. For this case, the interface concentration may build up to several times the free-field value without attaining a significant concentration profile (see Figure (IV-10)). The stability criterion then predicts that the tips may be very blunt (stabilized by solid phase heat flux) since constitutional supercooling is unlikely.

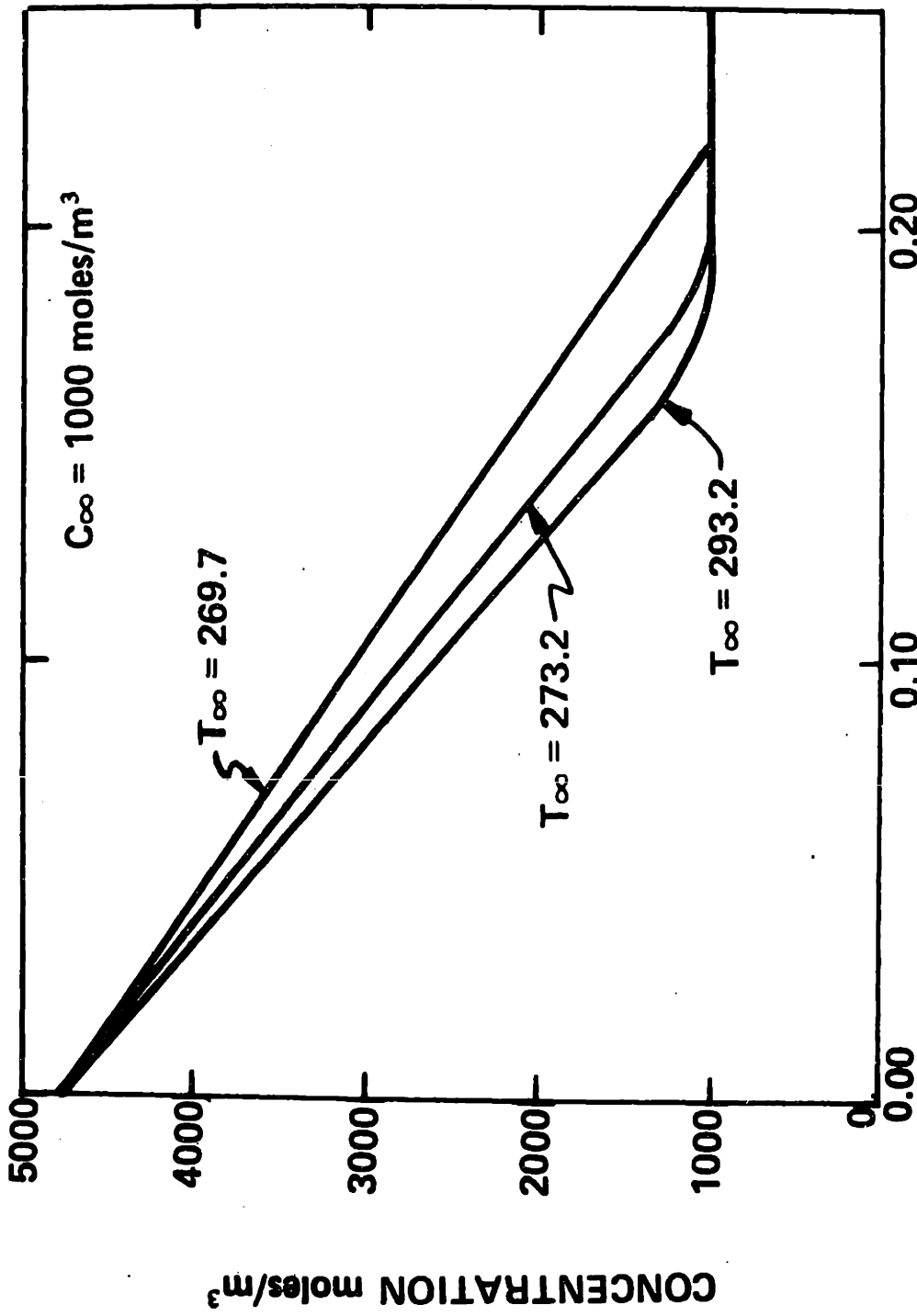
Since the stabilizing effect of the liquid phase heat flux is very small when solutions are frozen at their freezing temperatures, the dendrite shapes are extremely pointed. As the superheat increases, the dendrites tend to be more and more blunt. The most pointed result was for the freezing of a  $3000 \text{ mole/m}^3$  solution initially at its freezing temperature. The prolate spheroid describing the dendrite tip was at  $\eta = 0.011$ , which gives an aspect ratio (length/width) of over 100. Similarly, the most blunt case was for a  $145 \text{ mole/m}^3$  solution at  $T = 293.2\text{K}$  which had an oblate spheroidal tip with an aspect ratio of .0062 (nearly flat).

The concentration and temperature profiles at the centerline of the interdendritic liquid are shown in Figures (IV-21) and (IV-22). Both profiles are very nearly linear except for the decay to the free-field temperature and concentration values just beyond the dendrite tips.



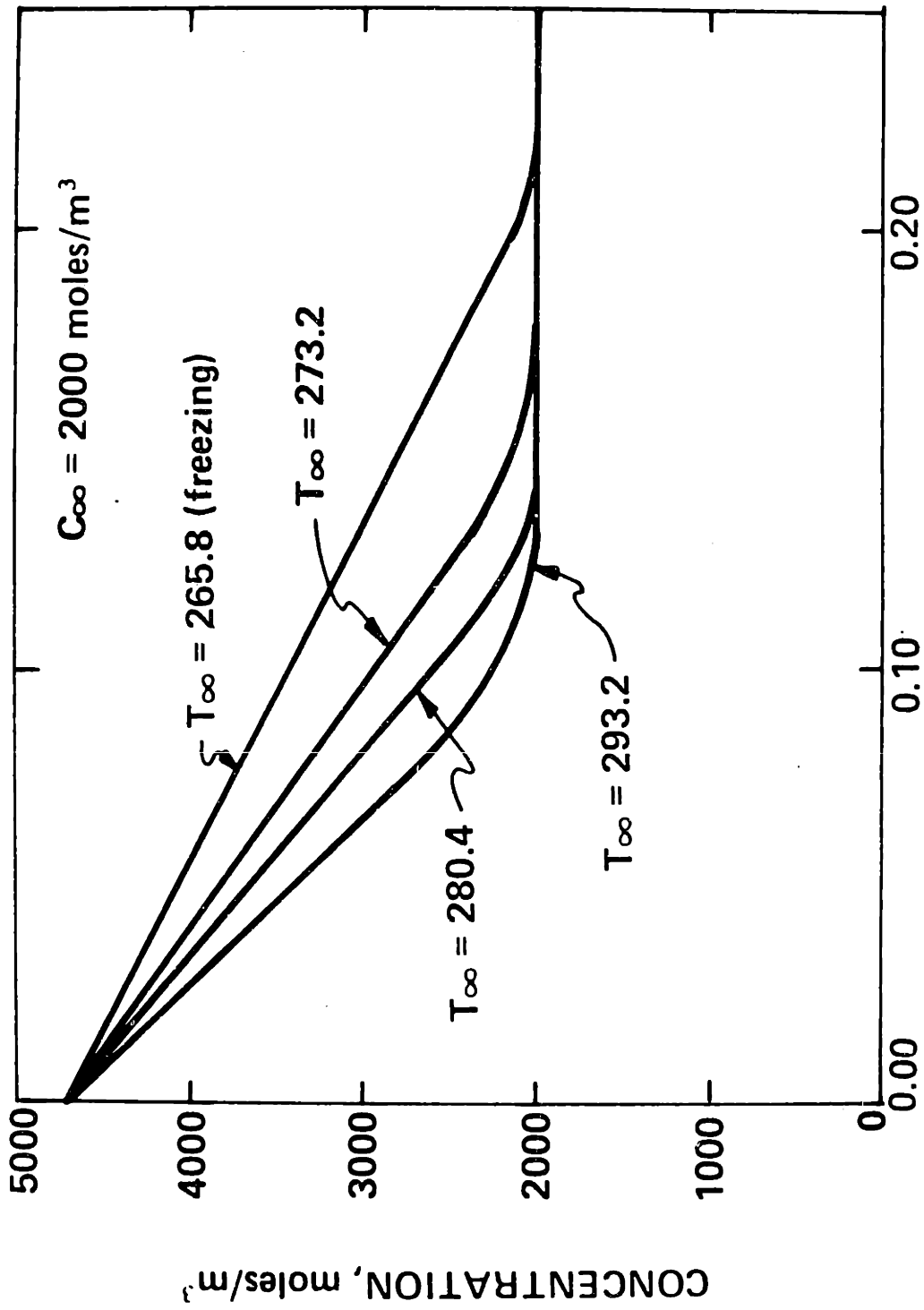
NON-DIMENSIONAL AXIAL POSITION, Z\*

Figure (IV-21a) Concentration Profiles Along the Interdendritic Mid-line, C<sub>∞</sub> = 145 moles/m<sup>3</sup>.

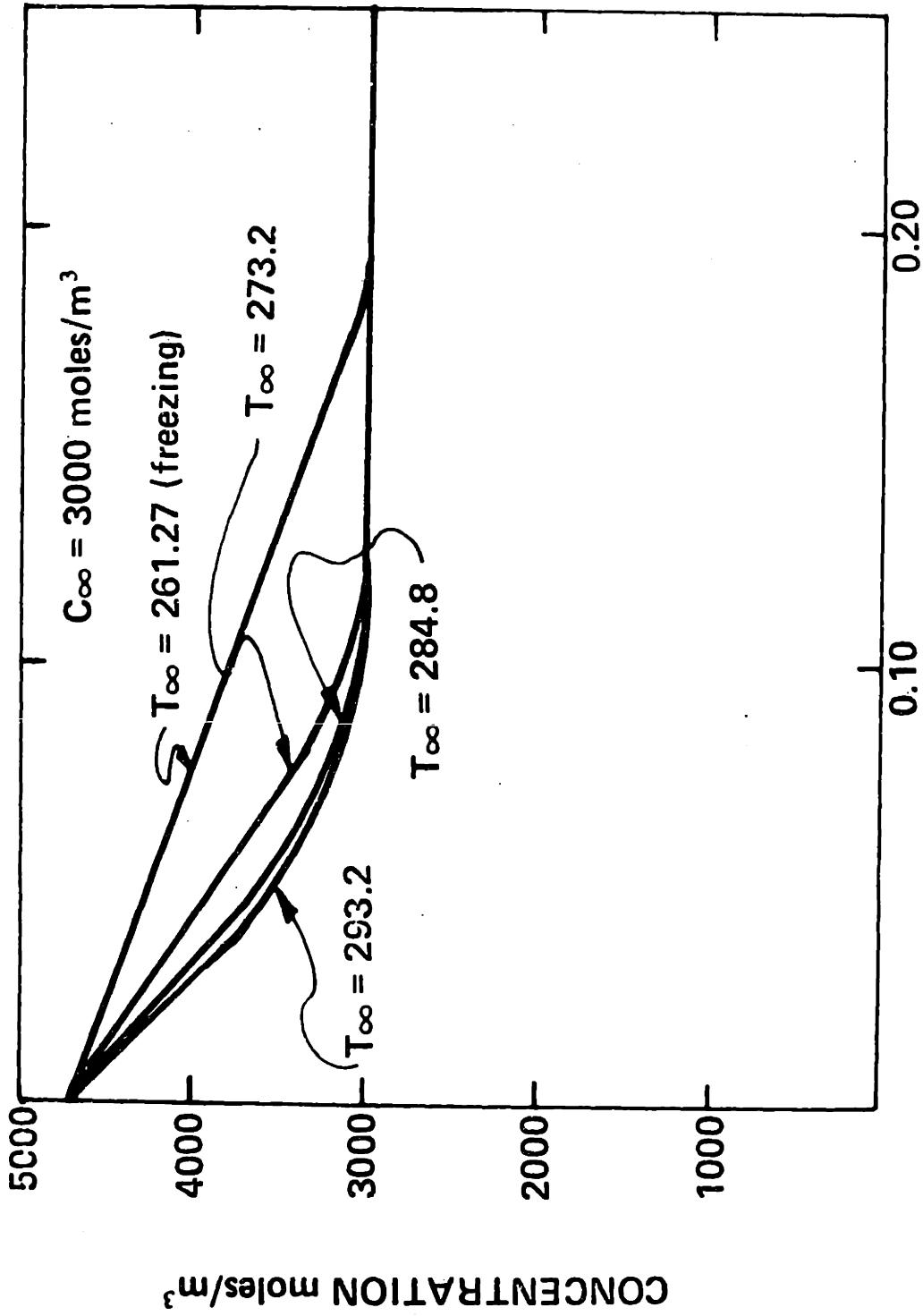


NON-DIMENSIONAL AXIAL POSITION,  $Z^*$

Figure (IV-21b) Concentration Profiles Along the Interdendritic Mid-line,  $C_\infty = 1000$  moles/m<sup>3</sup>.



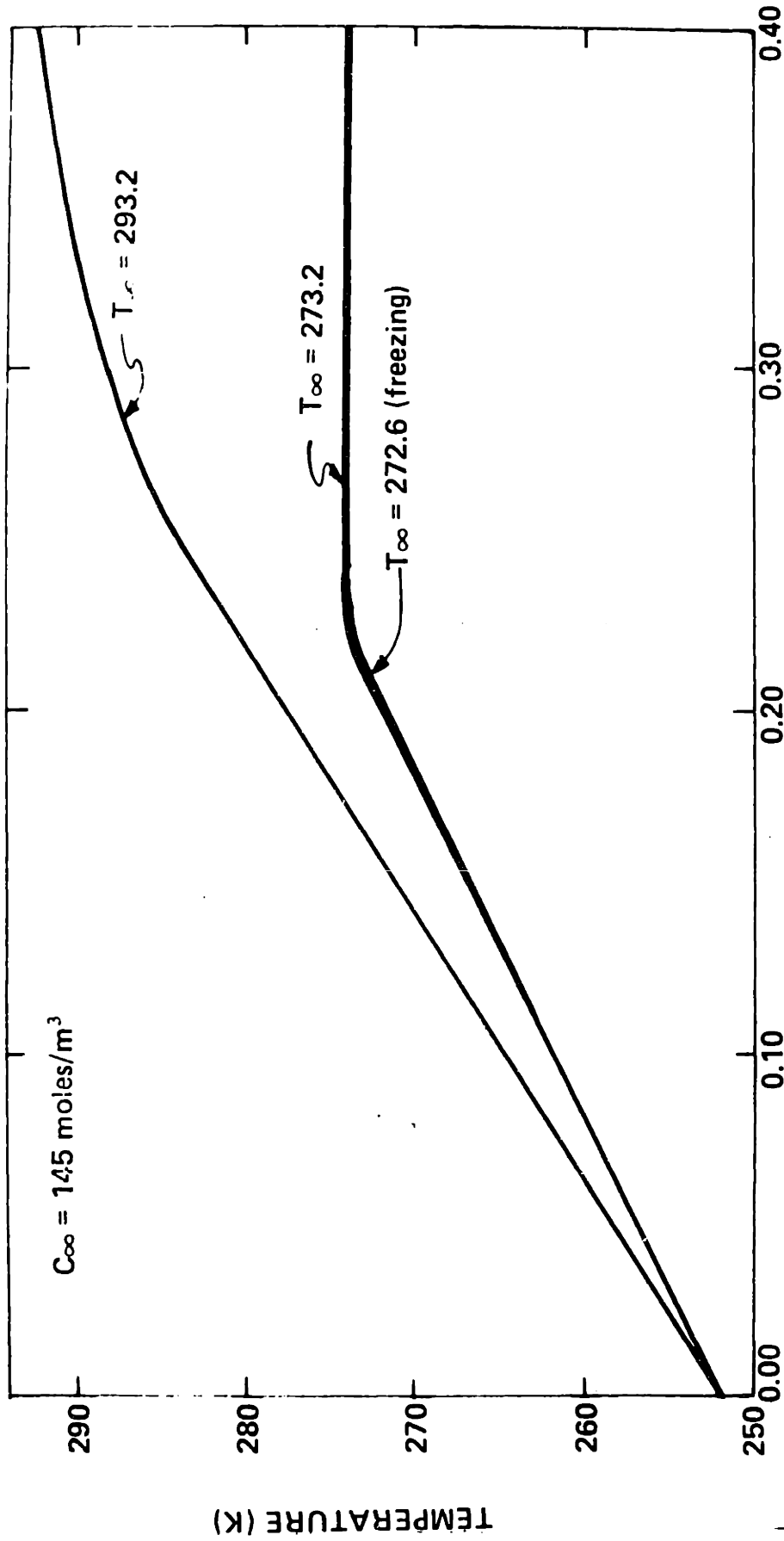
NON-DIMENSIONAL AXIAL POSITION, Z\*  
Figure (IV-21c) Concentration Profiles Along the Interdendritic Mid-line,  
 $C_{\infty} = 2000$  moles/m<sup>3</sup>.



NON-DIMENSIONAL AXIAL POSITION, Z\*

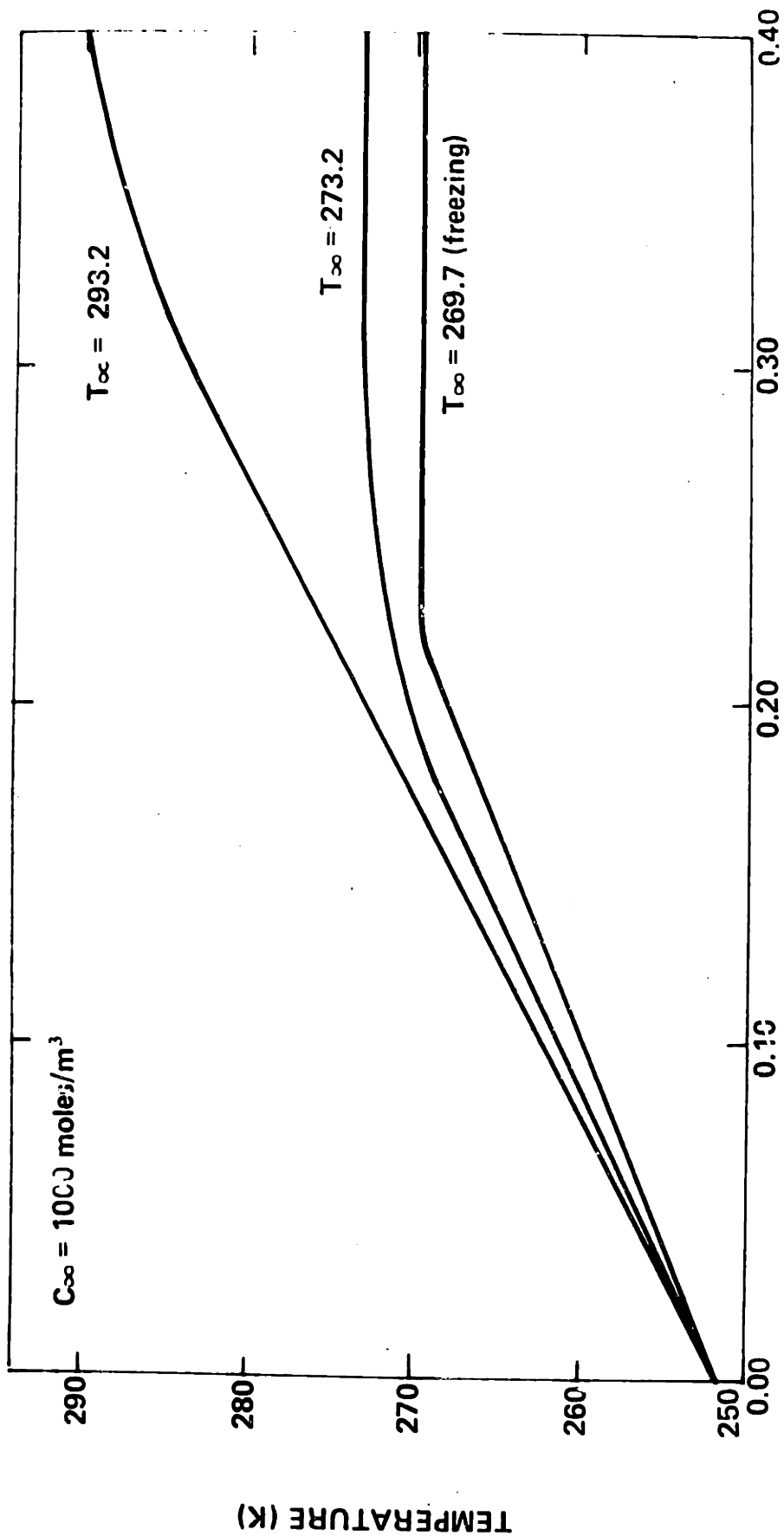
Figure (IV-21d) Concentration Profiles Along the Interdendritic Mid-line,  
 $C_{\infty} = 3000 \text{ moles/m}^3$ .





NON-DIMENSIONAL AXIAL POSITION,  $Z^*$

Figure (IV-22a) Temperature Profiles Along the Interdendritic Mid-line,  
 $C_\infty = 145 \text{ moles/m}^3$ .



NON-DIMENSIONAL AXIAL POSITION,  $z^*$

Figure (IV-22b) Temperature Profiles Along the Interdendritic Mid-Line,  
 $C_\infty = 1000 \text{ moles/m}^3$ .

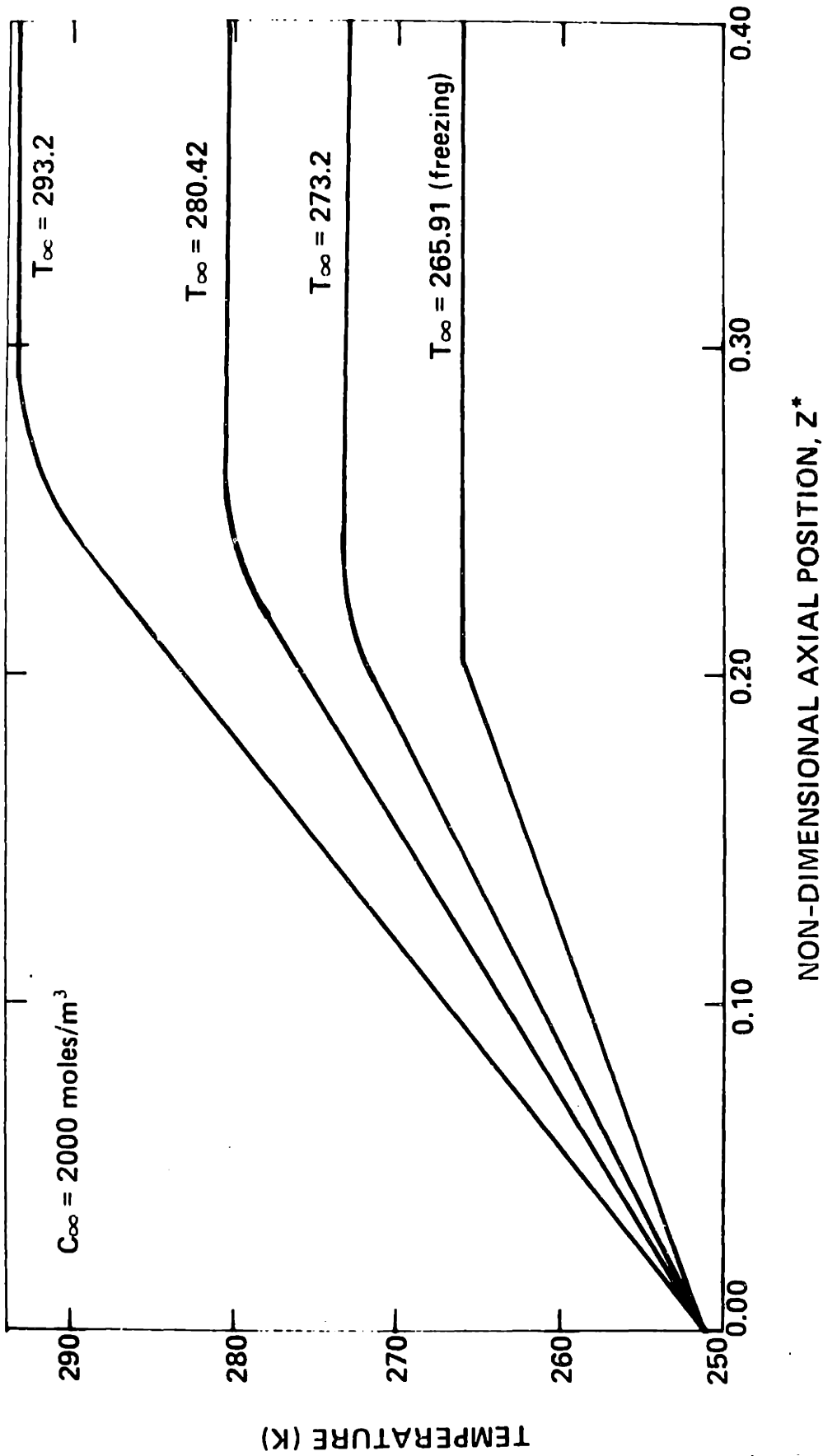
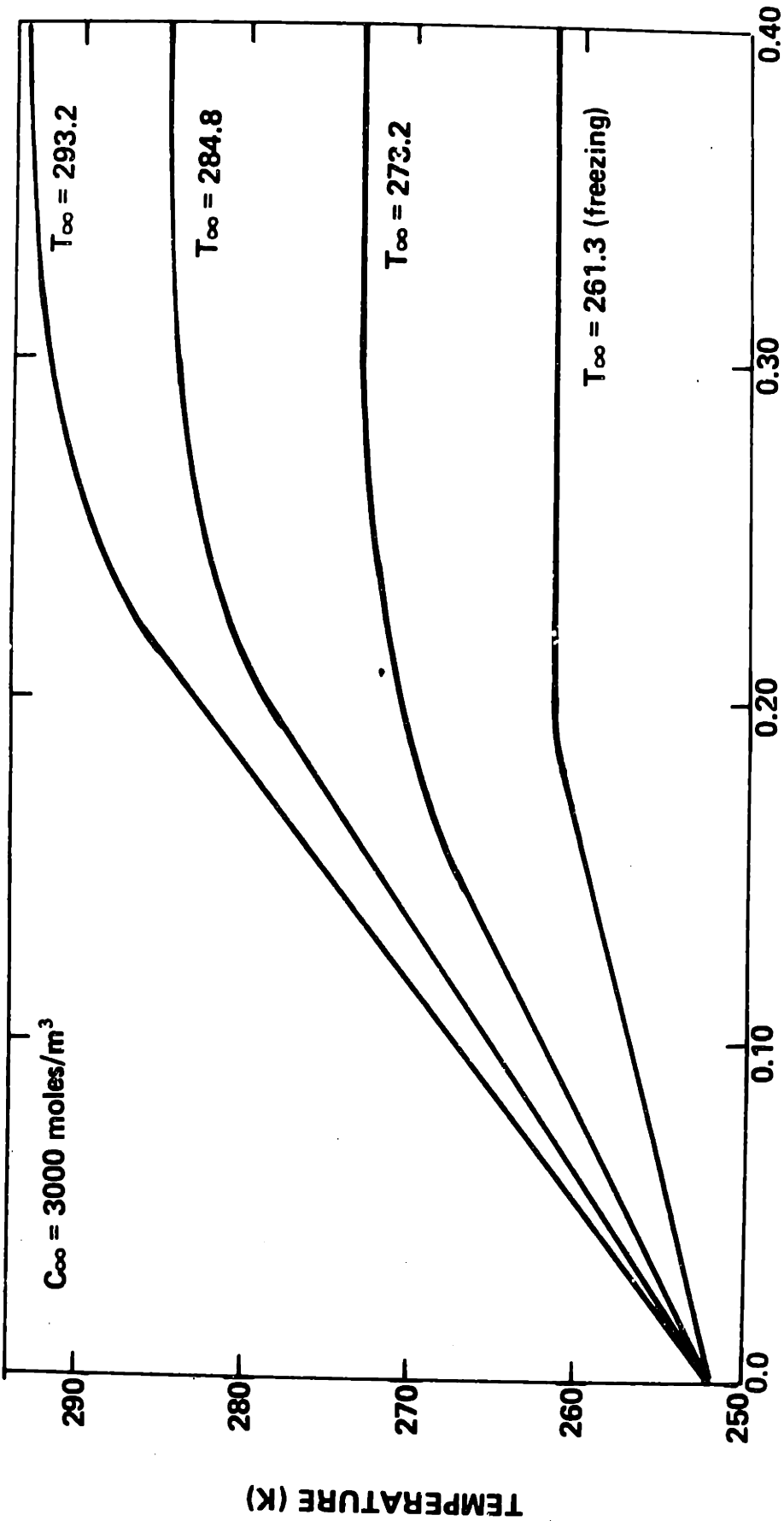


Figure (IV-22c) Temperature Profiles Along the Interdendritic Mid-Line,  
 $C_\infty = 2000 \text{ moles/m}^3$ .



NON-DIMENSIONAL AXIAL POSITION,  $Z^*$

Figure (IV-22d) Temperature Profiles Along the Interdendritic Mid-line,  
 $C_\infty = 3000$  moles/m<sup>3</sup>.

CHAPTER 5 KINETICS OF CELLULAR DEHYDRATION

V-A TRANSPORT EQUATION

The rate of water flux from the intracellular to the extracellular medium is given by [43]:

$$\frac{dN_w^I}{dt} = \frac{kA_c}{v_w} (\ln a_w^I - \ln a_w^O) \quad (V-1)$$

where  $A_w$  is the activity of water and the superscripts I and O refer to the intracellular and extracellular media respectively.

The water flux represents an attempt by the intracellular medium to attain equilibrium with the extracellular medium and is proportional to the departure from equilibrium across the cell membrane. The "departure" from equilibrium is given by the difference in the activity of water,  $(\ln a_w^I - \ln a_w^O)$ . The flux is also proportional to the membrane water conductivity  $k$  and the area for mass transfer  $A_c$ .

The characteristics of the water transport kinetics will depend on two parameters: the rate of change of the extracellular activity of water, and the membrane permeability. As discussed in Chapter 1, the membrane permeability in the present model will range from 0.1 to 1.0 times the permeability of the human erythrocyte. The erythrocyte permeability has been extensively modeled by Levin [44],

who derived the following permeability expression:

$$k = k_{tg} \exp \left\{ - \frac{E_K}{R_{GC}} \left( \frac{1}{T} - \frac{1}{T_G} \right) \right\} \quad (V-2)$$

where

$k_{tg}$  is the permeability at temperature  $T_G$   
 $E_K$  is the kinetic activation energy, and  
 $R_{GC}$  is the universal gas constant.

The value of  $k_{TG}$  at  $T_G = 298$  K has been measured by several investigators [45-47], and an average value is about  $17.3 \times 10^{-5}$  m/sec. Its value in the present work will range from  $1.73 \times 10^{-5}$  m/sec to  $17.3 \times 10^{-5}$  m/sec.

The extracellular activity of water is found using the temperature and concentration profiles along the interdendritic midline as shown in Figures (IV-21) and (IV-22). These transport fields were expressed in a coordinate system in which the interface was stationary and the biomaterial was moving. The spatial variable in this system is related to the temporal variable in the laboratory fixed system by:

$$\frac{d}{dt} = - R \frac{d}{dz} \quad (V-3)$$

Using this transformation, equation (V-1) becomes

$$\frac{dN_w^I}{dz} = - \frac{kA_c}{Rv_w} (\ln a_w^I - \ln a_w^0) \quad (V-4)$$

This equation allows direct calculation of  $\ln a_w^0$  from the temperature and concentration fields of Chapter IV. In the equilibrium region, the extracellular activity of water is derived by integrating the van't Hoff relationship:

$$\frac{\partial \ln a_w^0}{\partial T} = \frac{L_{HF}}{R_{GC} T^2} \quad (V-5)$$

using

$$L_{HF} = L_{HF}^0 + 9.08 T - 0.027 T^2 + 2.16 \times 10^{-4} T^3 \quad (V-6)$$

The resulting expression is given by

$$\begin{aligned} \ln \bar{a}_w^0 = & 3.736 \times 10^3 \left( \frac{1}{T} - \frac{1}{T_0} \right) + 36.18 \ln \left( \frac{T}{T_0} \right) \\ & + 0.1024 (T_0 - T) + 5.435 \times 10^{-5} (T^2 - T_0^2) \end{aligned} \quad (V-7)$$

where

$$T_0 = 273.15 \text{ K.}$$

In the region where the solution is superheated, the water activity will depend only on the concentration to good approximation [48]. In this case, the activity is found by calculating the freezing temperature corresponding to the concentration at a given position (equation III-16) and using the resulting temperature in equation (V-7). The activity of the superheated solution calculated in this manner is the same as if the same solution was at its freezing temperature, i.e., there is no dependence of activity on temperature.

The activity of the intracellular water,  $a_w^I$ , is expressed using the "pseudo-binary" solution model [10]. All of the intracellular solute is lumped into a single equivalent species and the osmotic data for this solution is curve-fit to a van-Laar [49] expression. The resulting activity is given by

$$\ln a_w^I = \frac{1.88 \times 10^{-2}}{(1.0 + 1.89 \times 10^{-2} \frac{X_w^I}{1 - X_w^I})} + \ln X_w^I \quad (V-8)$$

where

$$X_w^I = \frac{N_w^I}{N_w^I + N_m^H} \quad (V-9)$$

and  $N_m^H$  is the number of moles of hydrated equivalent solute contained within the cell.



Since the cell membrane is assumed permeable to water only,  $N_m^H$  is constant. Therefore, the intracellular water activity depends only on the number of moles of water remaining within the cell.

Let us define a dimensionless quantity of water as

$$\bar{N}_w = \frac{N_w^I}{N_{w0}^I} \quad (V-10)$$

where  $N_{w0}^I$  = the number of moles of intracellular water present initially. Substituting into equation (V-4), we have

$$\frac{d\bar{N}_w}{dz^*} = - \frac{L^* A_C k}{R v_w N_{w0}^I} (\ln a_w^I - \ln a_w^0) \quad (V-11)$$

where equation (IV-29) was used to transform to the  $z^*$  system. Finally, using equation (V-2) we have

$$\frac{d\bar{N}_w^I}{dz^*} = K_{KR} (\ln A_w^I - \ln A_w^0) \exp\left\{-\frac{E_K}{R}\left(\frac{1}{T} - \frac{1}{T_G}\right)\right\} \quad (V-12)$$

where

$$K_{KR} = \frac{K_{TG}}{R^2} \left\{ \frac{A_C}{V_w} \frac{(K_s - K_\ell)}{(\rho_s C_s - \rho_\ell C_\ell)} \right\} \cdot \quad (V-13)$$

Limiting values of  $K_{KR}$  are found by using  $K_{TG} = 1.73 \times 10^{-5}$  m/s,  $R = 1000 \mu\text{m}/\text{sec}$  for the lower limit and  $K_{TG} = 1.73 \times 10^{-5}$  m/s,

$R = 10 \text{ } \mu\text{m/s}$  for the upper limit. Substituting the appropriate numerical values into equation (V-13) gives

$$2 \times 10^1 \leq K_{KR} \leq 2 \times 10^6. \quad (\text{V-14})$$

Equation (V-10) may also be used non-dimensionalize the mole fraction expression, equation (V-9), to obtain

$$X_w^I = \frac{\bar{N}_w}{\bar{N}_w + N_m^H/N_{w0}^I}. \quad (\text{V-15})$$

The numerical data for the simulation of equation (V-12) are shown in Table (V-1). The cells are assumed initially in equilibrium with saline solution at the various free-field conditions. The initial number of moles of intracellular water, therefore, decreases with increasing free-field concentration.

## V.B. Results

Figure (V-1) shows the loci of thermodynamic states of the intracellular medium for a tissue initially at  $T_\infty = 273.2 \text{ K}$  and  $C_\infty = 145 \text{ moles/m}^3$ . This plot of the chemical potential of water versus temperature is the only unambiguous representation of the intracellular thermodynamic state. The upper right hand curve is the locus of two phase equilibrium states for a system of NaCl solution and pure ice;

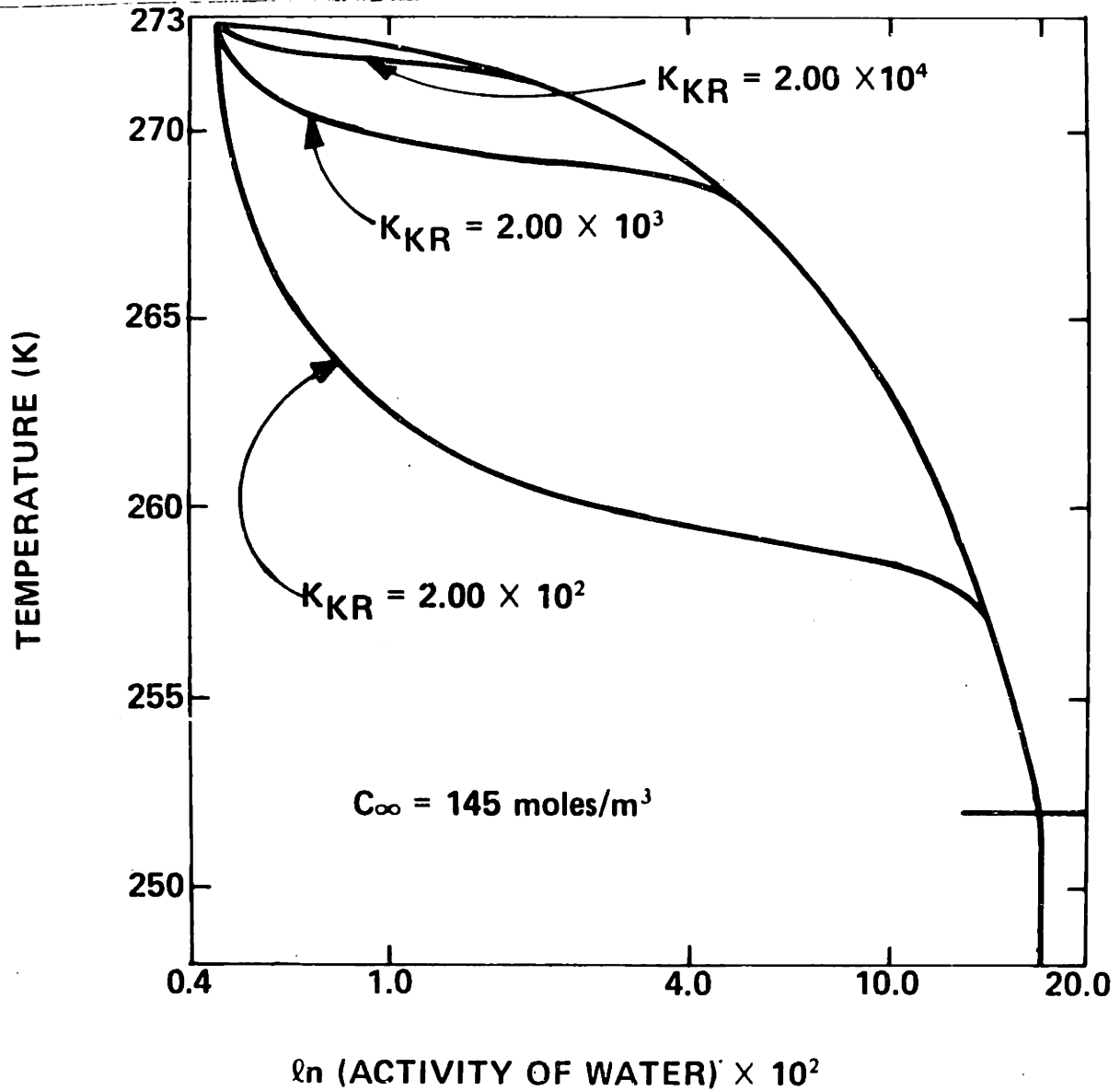


Figure (V-1) Loci of Intracellular Thermodynamic States,  
 $C_\infty = 145 \text{ moles/m}^3$ ,  $T_\infty = 273.2 \text{ K}$ .

all other points to the left of this curve represent non-equilibrium states. The driving force for water flux is the horizontal distance between the non-equilibrium locus of the intracellular solution and the equilibrium locus at a given temperature. As the cooling rate is increased or the permeability decreased (decreasing  $K_{KR}$ ) the cells become increasingly more supercooled in their attempt to attain equilibrium. As water is expressed from the cells, the non-equilibrium locus moves toward the equilibrium curve until finally the intracellular water attains the equilibrium activity.

The water volume flux out of the cells is plotted as a function of temperature in Fig. (V-2). The flux is not constant, but goes through a maximum that is a function of  $K_{KR}$ . The reason that the maximum water flux increases with higher interface speeds (at constant  $K_{tg}$ ) is that although the membrane permeability decreases with decreasing temperature (see Eq. (V-2)), the difference in chemical potential of water ( $\ln a_w^I - \ln a_w^O$ ) is greater at higher interface speeds. That is, at higher interface speeds, the extracellular activity of water is depressed more rapidly than the cells can respond to by expressing water. The intracellular medium tends to supercool, increasing the probability of intracellular ice nucleation.

For comparison, a thermodynamic trajectory is shown in Fig. (V-3) for  $C_{\infty} = 1000 \text{ moles/m}^3$  and  $T_{\infty} = 273.2(K)$ . Since the cells are initially in equilibrium with a higher concentration of saline, they contain less water. These cells have effectively completed part of

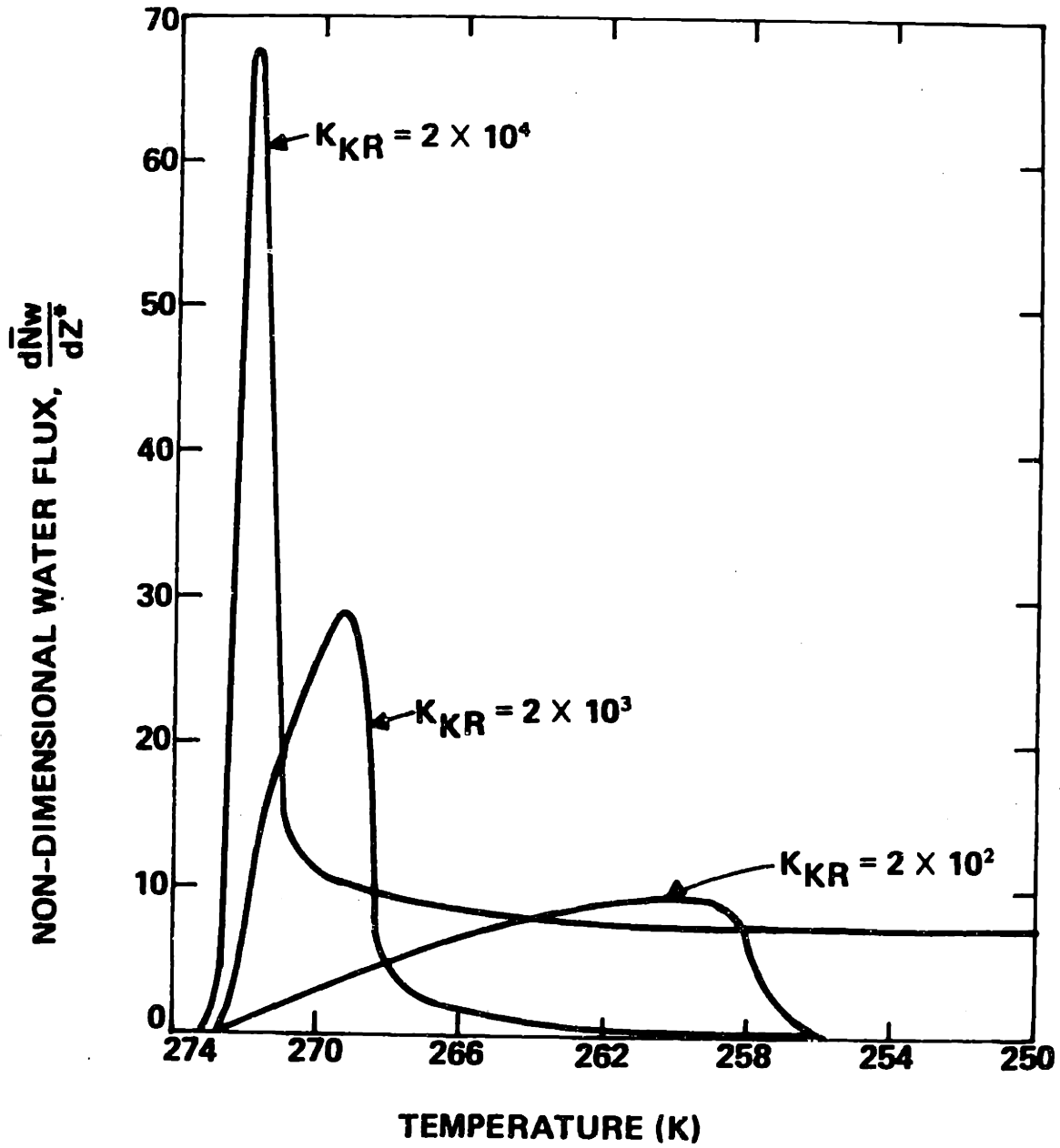


Figure (V-2) Water Volume Flux Versus Temperature,  $C_\infty = 145 \text{ moles/m}^3$ ,  $T_\infty = 273.2 \text{ K}$ .

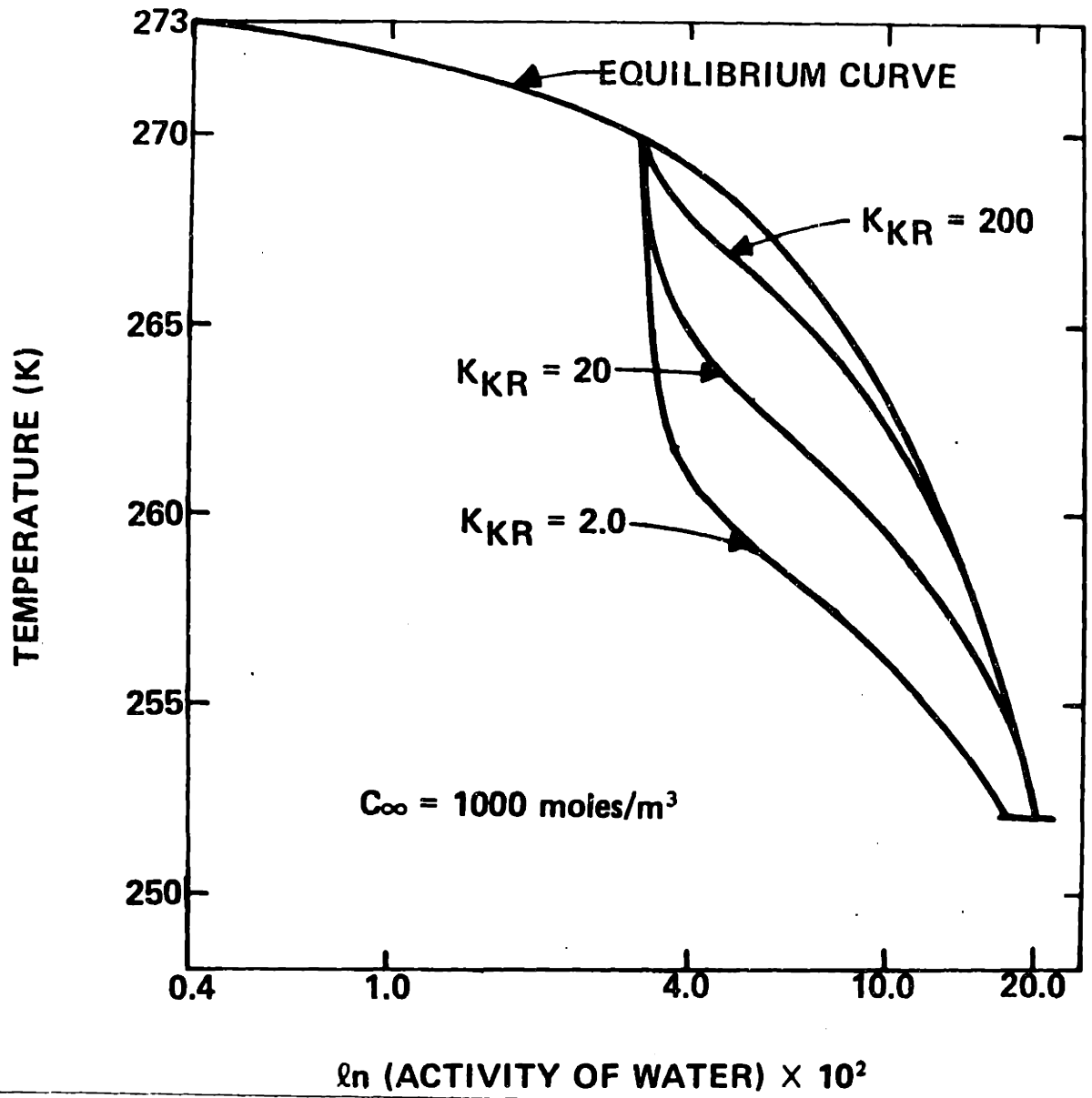


Figure (V-3) Loci of Intracellular Thermodynamic States,  $C_\infty = 1000 \text{ moles/m}^3$ ,  $T_\infty = 273.2 \text{ K}$ .

the dehydration process before the freezing protocol begins, and, therefore, have less tendency to supercool.

The criterion of most importance in assessing thermal protocols is the tendency of the cells to freeze internally. This is, in turn, related to the maximum departure from equilibrium of the intracellular substance represented by the quantity  $(\ln a_w^0 - \ln a_w^I)$ . A plot of this parameter versus  $K_{KR}$  is shown in Fig. (V-4) for various free-field conditions. The thermodynamic trajectories shown in Fig. (V-1) indicate that the maximum difference in the activity of water (MDA) decreases with increasing  $K_{KR}$  and this is confirmed in Fig. (V-4) for all cases. The MDA decreases markedly with free-field concentration. This is due to the large amount of water that has been expressed prior to freezing at the higher free-field concentrations. Substantially smaller driving force for mass transfer is required (represented by the MDA) since less water remains to be expressed. Increasing free-field temperature increases the MDA due mainly to the shorter characteristic dendrite length at higher values of superheat (see Fig. IV-19). The effective cooling rate is higher for shorter dendrites so the driving force for mass transfer must be larger.

The curves shown in Fig. V-4 are expected to be asymptotic at very high and very low values of permeability. At the lower permeability, essentially none of the intracellular water can escape during freezing, and reducing the temperature of the system serves only to supercool the cells. This asymptotic MDA is given by:

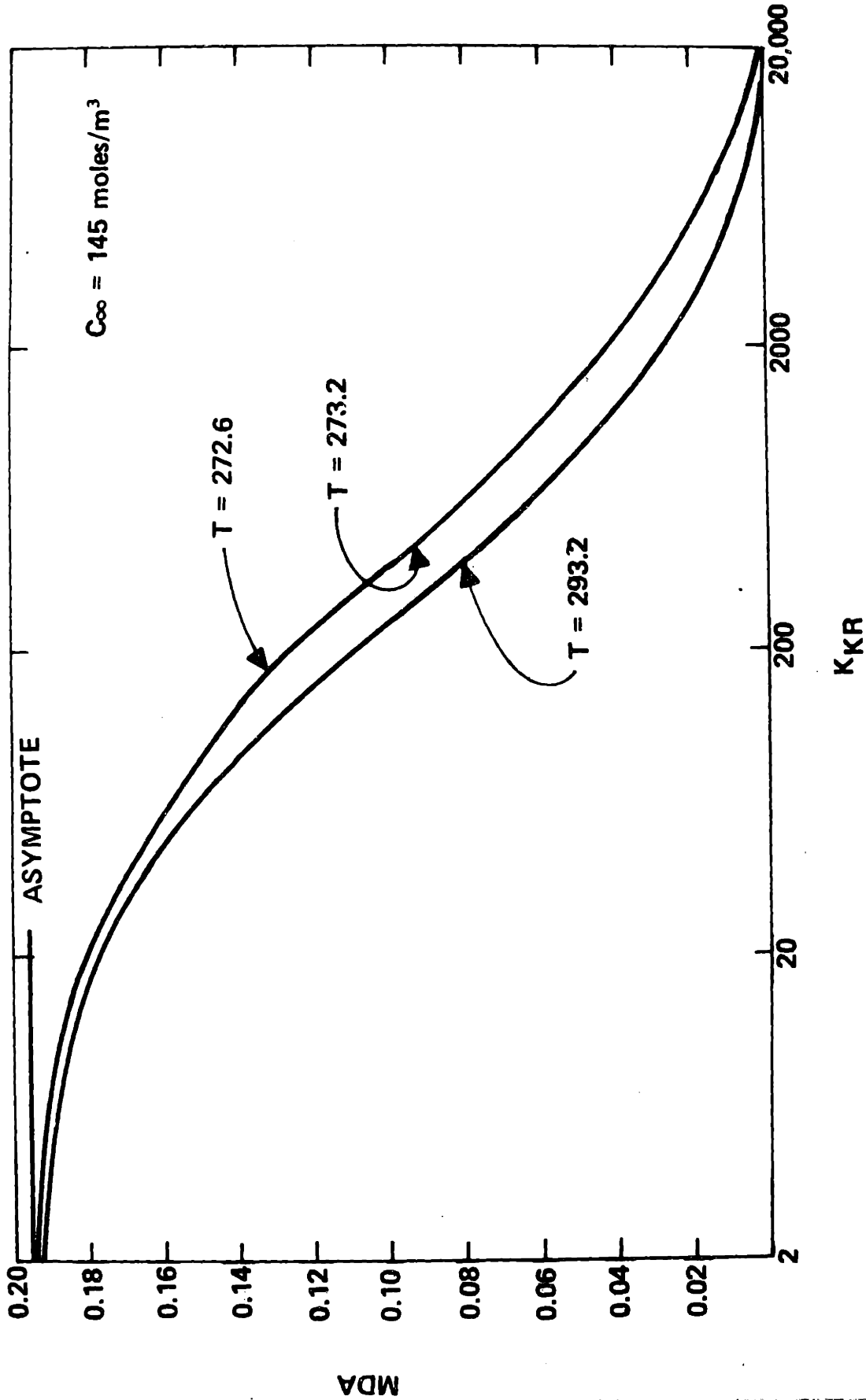


Figure (V-4a) Maximum Difference in the Activity of Water Versus Ratio of Water Permeability to (Interface Speed)<sup>2</sup>, C<sub>∞</sub> = 145 moles/m<sup>3</sup>.



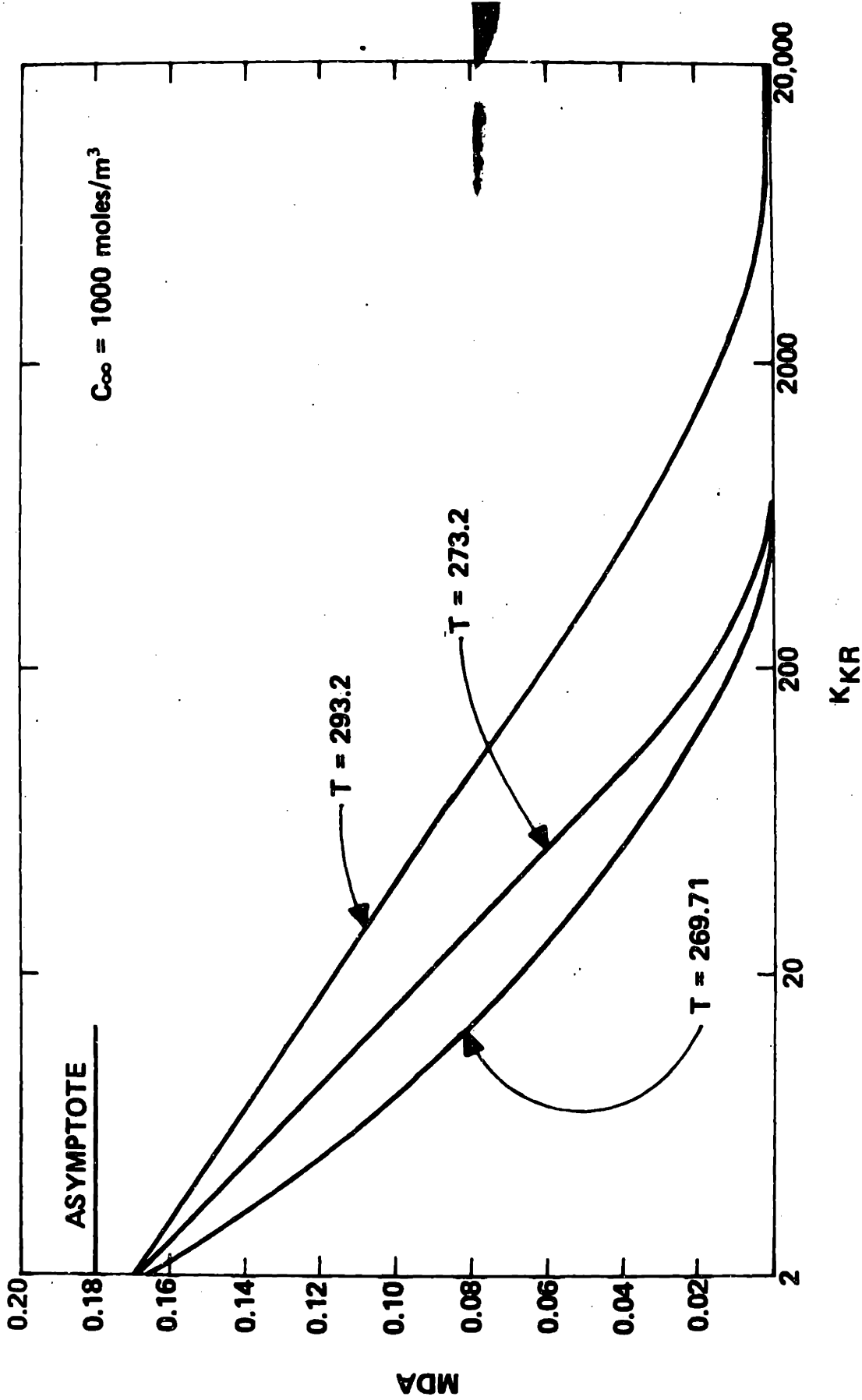


Figure (V-4b) Maximum Difference in the Activity of Water Versus Ratio of Water Permeability to (Interface Speed)<sup>2</sup>, C<sub>∞</sub> = 1000 moles/m<sup>3</sup>.

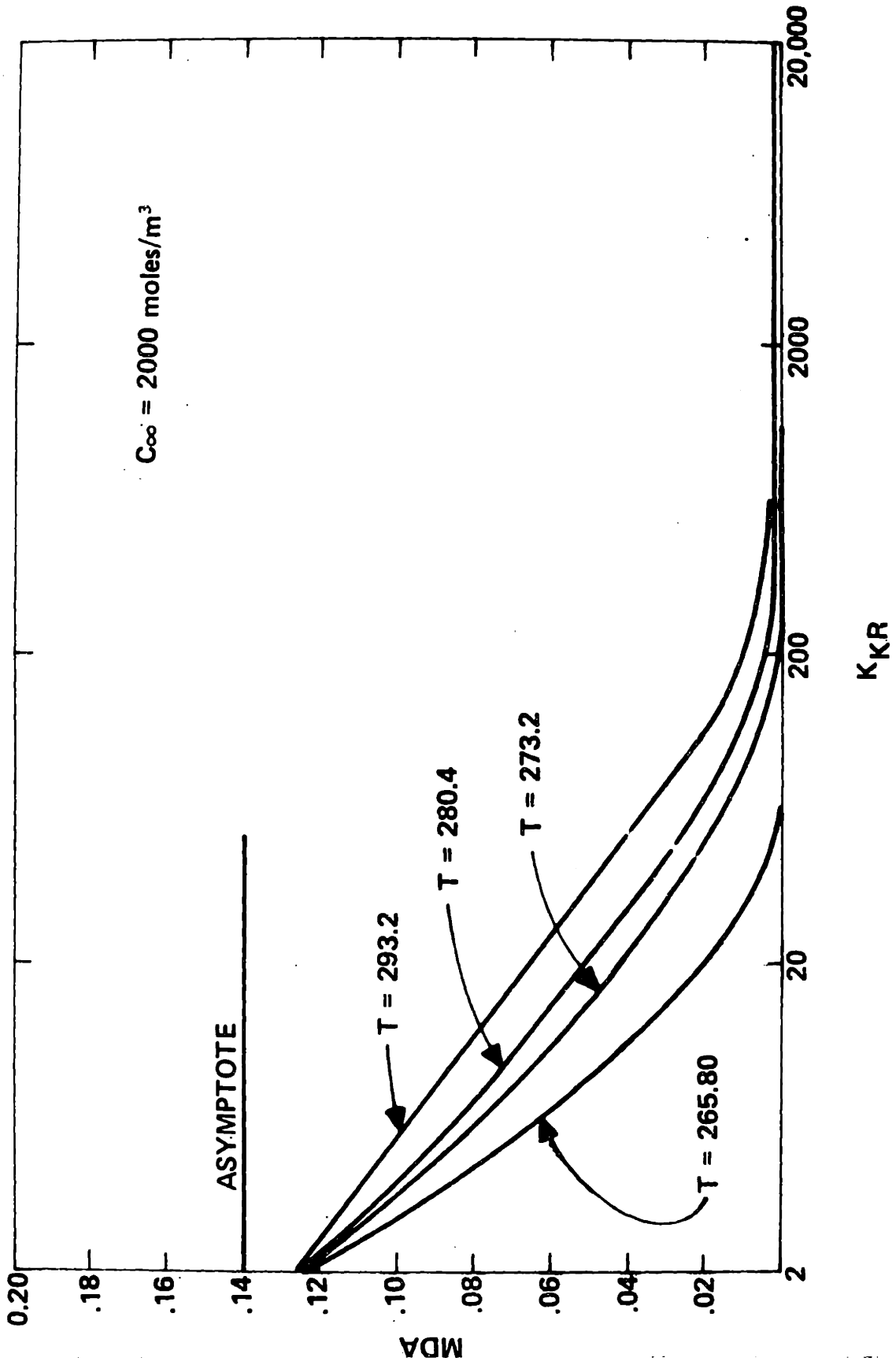


Figure (V-4c) Maximum Difference in the Activity of Water Versus Ratio of Water Permeability to (Interface Speed)<sup>2</sup>, C<sub>∞</sub> = 2000 moles/m<sup>3</sup>.

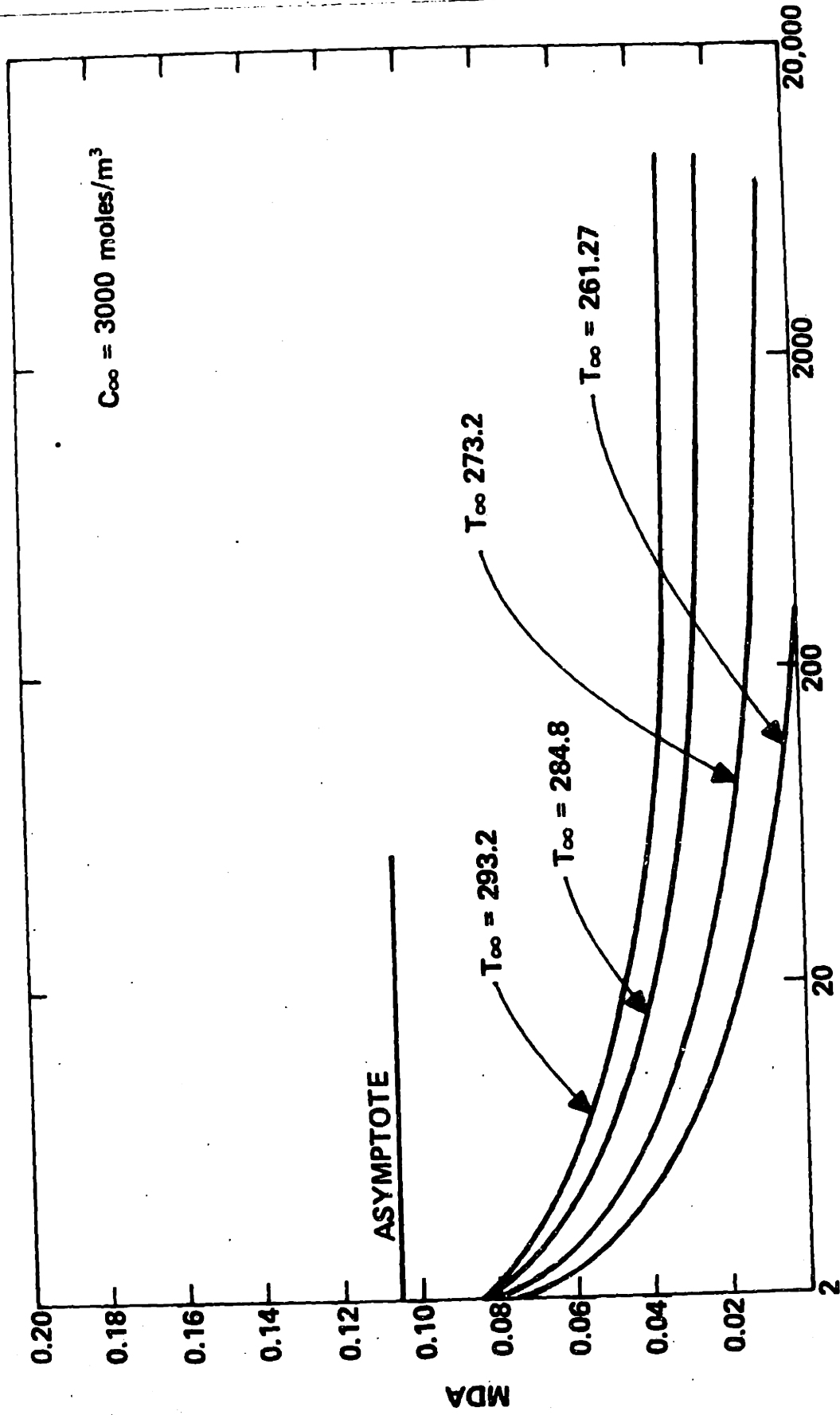


Figure (V-4d) Maximum Difference in the Activity of Water Versus Ratio of Water Permeability to (Interface Speed)<sup>2</sup>,  $C_\infty = 3000 \text{ moles/m}^3$ .

KKR

MDA (asymptote at low  $K_{KR}$ ) =

$$a_w (\text{at } C_\infty) - a_w (\text{eutectic}) \quad (V-16)$$

and is shown for each case in Fig. (V-4). When the permeability is high, the driving force necessary for mass transfer (represented by the MDA) approaches zero. The asymptotic behavior at low and high values of  $K_{KR}$  suggests the S-shaped behavior as shown in Fig. (V-4a) for  $C_\infty = 145 \text{ moles/m}^3$ . The curves in Fig. (V-4b) - (V-4d) are restricted to the high permeability end of this hypothetical S-shaped curve, since the lower permeability at these concentrations are not physically realistic.

Fig. (V-4) together with Fig. (IV-18) may be used as a "design" aid for optimizing thermal protocols. For example, if we choose a particular tissue at temperature  $T_\infty$  and an equivalent CPA level of  $C_\infty$ , we may use Fig. (V-4) to determine the trade-off between a larger MDA (and, therefore, higher probability of intracellular freezing) and lower  $K_{KR}$ . Setting an arbitrary maximum level for the activity difference allows determination of  $K_{KR}$ . If the membrane permeability of the tissue is known, this value of  $K_{KR}$  will give the appropriate interface speed  $R$  (from Eq. (V-13)). Finally, from Fig. (IV-18), the necessary heat flux to produce this interface speed is specified.

Parameter	Numerical Value	Units
$E_K$	16.32	N-m/gm-mole
$R_{GC}$	8.314	N-m/gm-mole-K)
$V_w$	$18.0 \times 10^{-6}$	$m^3$ /gm-mole
$N_m^H$	$2.21 \times 10^{-14}$	gm-moles
$A_C$	$1.35 \times 10^{-10}$	$m^2$
$N_{wO}^I$	$4.0 \times 10^{-12}$	gm-moles ( $C_\infty = 145 \text{ moles/m}^3$ )
	$0.503 \times 10^{-12}$	gm(moles) ( $C_\infty = 1000 \text{ moles/m}^3$ )
	$0.251 \times 10^{-12}$	gm(moles) ( $C_\infty = 2000 \text{ moles/m}^3$ )
	$0.159 \times 10^{-12}$	gm(moles) ( $C_\infty = 3000 \text{ moles/m}^3$ )

TABLE V-1: Numerical Data for Cell Dehydration Simulation

CHAPTER VI SUMMARY AND SUGGESTIONS  
FOR FURTHER RESEARCH

As an approximation to the freezing of tissue, the solidification of a body of NaCl-H<sub>2</sub>O solution was analyzed. The solid-liquid interface was found to be planar initially but quickly breaks down to the dendritic interface morphology. The analysis determines the heat flux that must be imposed on the system to produce solidification at various rates and free-field conditions. It also predicts the interface shape and complete concentration and temperature fields for these imposed conditions.

The dehydration kinetics were determined for erythrocyte -- like cells which were exposed to the temperature and concentration fields determined previously. The results are expressed in terms of thermodynamic trajectories, water flux rate curves and the maximum difference in the activity of water (MDA) between the intracellular and extracellular media. Using the MDA as an indicator of intracellular ice probability, a thermal optimization algorithm was devised, which allows researchers to evaluate thermal protocols as a function of free-field condition, membrane permeability and rate of freezing.

On the basis of this work, the following suggestions for further research are made:

- (1) Further refinement of the freezing model. For purposes of determining the kinetics of cellular dehydration per se, the model of dendritic freezing developed in Chapter IV is accurate. However, the analysis of the freezing of saline was done independently from the cellular dehydration model. The effect of this uncoupling of the two processes should be determined.
  
- (2) Experimental verification of the saline freezing model. The most important experimental aspects of this model are:
  - (a) Measurement of temperature and concentration profiles under various freezing rates and boundary conditions.
  - (b) Qualitative determination of interface morphology including dendrite length and tip geometry.
  - (c) Measurement of required heat flux for various freezing rates and free-field conditions, and
  - (d) Verification of the similarity model.

(3) Measurement of cellular dehydration kinetics for the freezing of a simple tissue. This would entail the measurement of the relative cell volume as a function of position when the cells are near the advancing ice crystals. Liquid nitrogen quenching followed by freeze substitution is a possible technique.

(4) Further development of CPA addition protocols.

The algorithm for optimizing thermal protocols stated in Chapter 5 was based on the restriction of the maximum difference in the activity of water to certain levels. The determination of these levels is outside the scope of this work but depends on the maximum osmotic stress that the membranes can withstand and on the kinetics of intracellular ice nucleation. The general trend illustrated in Figure (V-4) is that higher concentrations of cryoprotective agent (represented by concentrated saline) produce lower MDA's. This conclusion is in keeping with the observation of Huggins\* that the solution to the organ freezing problem will be by the use of higher concentrations of CPA, "the higher the better".

---

\*Personal Communication



APPENDIX I: NUMERICAL METHODS

AI-A Runge-Kutta Integration Routine

The differential equations describing the planar freezing case (III-37 - III-39) and those describing the equilibrium freezing zone (IV-31 and IV-32) were solved numerically using a fourth-order Runge-Kutta integration routine. The form of the equations which were solved is:

$$\begin{aligned} \frac{d}{dt} y_1 &= f_1(t, y_1, y_2, \dots, y_n) \\ \frac{d}{dt} y_2 &= f_2(t, y_1, y_2, \dots, y_n) \\ &\cdot \\ &\cdot \\ &\cdot \\ \frac{d}{dt} y_n &= f_n(t, y_1, y_2, \dots, y_n) \end{aligned} \quad (\text{AI-1})$$

This may be compactly written as

$$\frac{d}{dt} \vec{Y} = \vec{F}(t, \vec{Y}) \quad (\text{AI-2})$$

where  $\vec{Y}$  is an n-dimensional vector made up of the current values of  $y_1, \dots, y_n$  and  $\vec{F}$  is current values of  $f_1, \dots, f_n$ .

Given  $\vec{Y}_0$ , the value of the  $\vec{Y}$  vector at some value of  $t$ , say  $t_0$ , then the approximate value of the  $\vec{Y}$  vector at  $t_0 + \Delta t$  is:

$$\vec{Y}(t + \Delta t) = \vec{Y}_0 + \frac{1}{6} [K_0 + 2K_1 + 2K_2 + K_3] \quad (\text{AI-3})$$

where the  $K$ 's are defined as:

$$\begin{aligned} K_0 &= \vec{F}(t_0, \vec{Y}_0) \cdot \Delta t \\ K_1 &= \vec{F}\left(t_0 + \frac{\Delta t}{2}, \vec{Y}_0 + \frac{1}{2}K_0\right) \cdot \Delta t \\ K_2 &= \vec{F}\left(t_0 + \frac{\Delta t}{2}, \vec{Y}_0 + \frac{1}{2}K_1\right) \cdot \Delta t \\ K_3 &= \vec{F}(t_0 + \Delta t, \vec{Y}_0 + K_2) \cdot \Delta t \end{aligned} \quad (\text{AI-4})$$

Knowing the value of  $\vec{Y}_0$  at some time  $t_0$  (i.e., the initial conditions at  $t = 0$ ), the solution may be calculated at  $k\Delta t$  when  $K$  is the number of iterations.

The Runge-Kutta method will converge to the true solution at  $\Delta t \rightarrow 0$ , is self starting, and does not exhibit the weak instabilities which may be present in linear multistep methods. On the other hand, the method requires that the function  $F$  be evaluated four times for each time step.

Since the Runge-Kutta method is self starting, each time step calculation is independent of the preceding and following

calculation. Consequently, the value of  $\Delta t$  may be altered during the course of the solution in order to maintain a sufficiently accurate solution.

Single differential equations that are  $n^{\text{th}}$  order may be converted into  $n$  first order equations. The arbitrary  $n^{\text{th}}$  order differential equation:

$$\frac{d^n y}{dt^n} = F\left(t, y, \frac{dy}{dt}, \frac{d^2 y}{dt^2}, \dots, \frac{d^{n-1} y}{dt^{n-1}}\right) \quad (\text{AI-5})$$

may be reduced by introducing the variables

$$x_1, x_2, x_3, \dots, x_n$$

defined by

$$\begin{aligned} \frac{dx_1}{dt} &= x_2 \\ \frac{dx_2}{dt} &= x_3 \\ \frac{dx_3}{dt} &= x_4 \\ &\vdots \\ \frac{dx_{n-1}}{dt} &= x_n \end{aligned} \quad (\text{AI-6})$$

It then follows immediately that

$$\frac{dx_n}{dt} = F(t, y, \frac{dy}{dt}, \dots) \quad . \quad (AI-7)$$

APPENDIX II DENDRITE SPACING

Very little quantitative theoretical work has been done on predicting dendrite spacing as a function of free-field conditions. Several workers have conducted experimental studies on dendrite spacing in Al-Cu alloys as a function of solidification variables. In most cases, dendrite spacing has been found to increase linearly with the square root of a characteristic freezing time  $t_f$ , although the effect of free-field temperature and concentration is not clear.

The most recent quantitative work on dendrite spacing was done by Rohatgi and Adams [50]. They analyzed the lateral mass transport in the interdendritic liquid, and by assuming that the constitutional supercooling in this region is small, derived a relationship between the dendrite spacing and solidification parameters as follows:

$$L_D \sqrt{\frac{1}{t_f}} = A_1 + A_2 C_\infty \quad (\text{AII-1})$$

where  $L_D$  is the dendrite spacing and  $A_1, A_2$  are constants. The characteristic freezing time,  $t_f$ , is defined by

$$t_f = 0.25 \frac{L^*}{R} \quad (\text{AII-2})$$

where  $0.25L^*$  is a characteristic dendrite length. Physically,  $t_f$  is the time required for a material particle to move from the dendrite tips to the basal plane. Using the definition of  $L^*$ , equation (AII-2) transforms to

$$t_f = \frac{0.25}{R^2} \frac{(K_s - K_l)}{(\rho_l C_l - \rho_s C_s)} \quad (\text{AII-3})$$

and the final dendrite spacing equation becomes

$$L_D = \frac{1}{R} \sqrt{\frac{0.25 (K_s - K_l)}{(\rho_l C_l - \rho_s C_s)}} (A_1 + A_2 C_\infty) \quad (\text{AII-4})$$

Some experimental data relating dendrite spacing to freezing time has been obtained by Rohatgi [ 50] for aqueous systems. The data is replotted in Figure (AII-1) for the case of an aqueous potassium-chloride (KCl) solution. The osmotic behavior, ionic radius, and melting point of KCl solutions are sufficiently close to that of NaCl, so that the results may be assumed interchangeable.

The linear relationship between dendrite spacing and concentration is apparent from figure (AII-1) . Using a least-squares curve fit, we may obtain estimates of the constants  $A_1$  and  $A_2$ . Substituting these estimates into equation (AII-4), we have

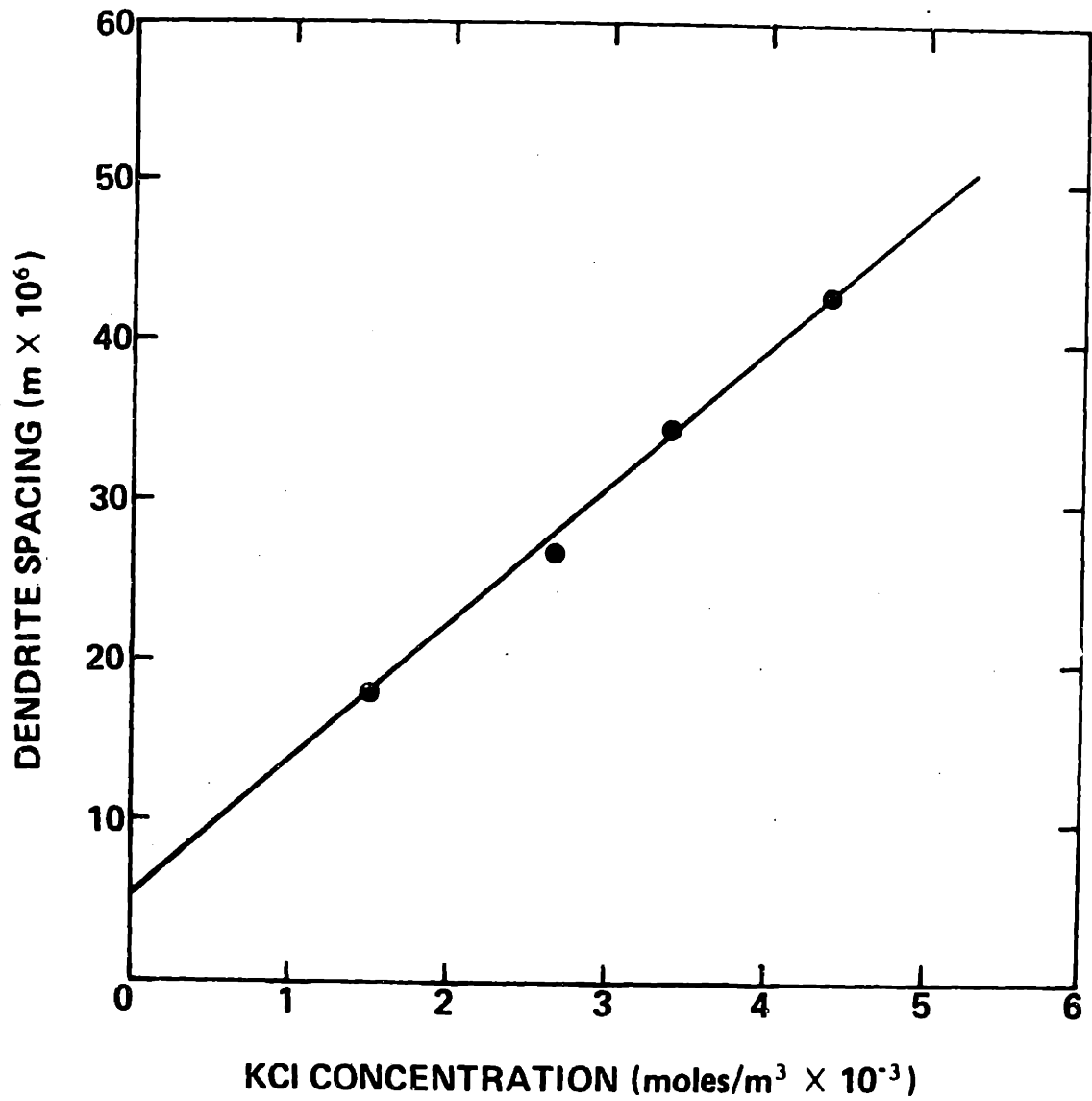


Figure (AII-1) Experimental Results for Dendrite Spacing Versus KCl concentration (ref. Rohatgi [50]).

$$L_D = \frac{1}{R} \sqrt{\frac{0.25 (K_S - K_L)}{(\rho_L C_L - \rho_S C_S)}} (6.41 \times 10^{-7} + 1.09 \times 10^{-6} C_\infty) (\text{meters}) \quad (\text{AII-5})$$



REFERENCES

1. Childs, J. W. and Lower, R. R., "Preservation of the Heart", Progress in Cardiovascular Disease 12:149 (1969).
2. Slapak, M., Wigmore, R.H., and McLean, L.D., "Twenty-four hour Liver Preservation by the Use of Continuous Pulsatile Perfusion and Hyperbaric Oxygenation", Transplantation 5:1154 (1967).
3. Belzer, F.O., Ashlan, B.S., May, R.E. and Dunphy, J.E., "Isolated Perfusion of Whole Organs", in Organ Perfusion and Preservation, ed. by J.C. Norman, Appleton-Century-Crofts, New York (1968), pp 3-26.
4. Damjanovic, V., Edwards, D. C. and Thomas D., "Recovery of Haemolytic Plague-Forming Cells After Freeze-drying", Nature 253:116 (1975).
5. Mazur, P., "Cryobiology: The Freezing of Biological Systems", Nature 168:939 (1970).
6. Meryman, H.T, Ed., Cryobiology, Academic Press, New York (1966).
7. Luyet, B., "A Review of Research on the Preservation of Hearts in the Frozen State", Cryobiology 8:190 (1971).
8. Mazur, P., "Causes of Injury in Frozen and Thawed Cells", Fed. Proc. Amer. Soc. Exp. Biol. 24, pp 5175-5182 (1965).
9. Polge, C., Smith, A.U. and Parkes, A., "Revival of Spermatozoa after Vitrification and Dehydration at Low Temperatures", Nature pp 164-666 (1949).
10. Levin, R. L., "Kinetics of Water Transport in Biomaterials During Freezing", ScD Thesis, Dept. of Mech. Eng., MIT, June, 1976.
11. Stein, W.D., The Movement of Molecules Across Cell Membranes, Academic Press, New York and London, 1967.
12. O'Callaghan, M. G., "Photomicrographs of Frozen Rat Myocardium" Dept. of Mech. Eng., MIT, 1975 (Unpublished Research).
13. Flemings, M.C., "Solidification Processing", McGraw-Hill, New York (1974).

REFERENCES (CONTINUED)

14. Kramer, J. J. and Tiller, W.A., "Breakdown of the Planar Solid-Liquid Interface", J. Chem. Phys. 42:257 (1965).
15. Rigney, D.A. and Blakely, J. N., "Stability of Planar Freezing", Acta. Met. 14:1375 (1966).
16. Chalmers, B., Principles of Solidification, John Wiley & Sons, New York, 1964.
17. Mullins, W.W. and Sekerka, R.F., "Morphological Stability of a Particle Growing by Diffusion or Heat Flow", JAP 31:323 (1963).
18. Rohsenow, W.R., Choi, H.Y., Heat, Mass and Momentum Transfer, Prentice-Hall, New Jersey 1961.
19. Carslaw, H.S. and Jaeger, J.C., Conduction of Heat in Solids, Second Edition, Oxford University Press, London, 1959.
20. Evans, G.W., Isaacson, E., and MacDonald J.K.L. "Stefan-like Problems", Quart. Appl. Math. 8:312 (1950).
21. Rubenstein, L. J. Investia Aka. Nank. SSSR, Geograph. Geophysical Series, Vol. II, No. 6, p. 489, 1947. (no title available).
22. Weiner, J. H., "Transient Heat Conduction in Multi-Phase Media", British Journal of Appl. Physics, 6:361 (1955).
23. Landau, H.G., "Heat Conduction in a Melting Solid", Quart. Appl. Math. 8:81 (1950).
24. Forster, G.A., "Finite Difference Approach to Some Heat Conduction Problems Involving Changes of State", English Electric Company, Ltd., Report LA.t.059, (1954).
25. Pohlhausen, K., "Zur naherungsweise Integration der Differentialgleichung der laminaren", ZAMM 1:252 (1921).
26. von Karman, T., "Uber laminare und turbulente Reibung", ZAMM 1:233 (1921).
27. Goodman, T.R., "The Heat Balance Integral and Its Application to Problems Involving Change of Phase", J. Heat Transfer, Trans. ASME 80:335 (1958).

REFERENCES (CONTINUED)

28. Goodman, T.R., "Application of Integral Methods to Transient Non-Linear Heat Transfer", Advances in Heat Transfer, Vol. 1 Irvine, T. F. and Hartnett, J.P., eds. 1964, p. 51.
29. Goodman, T.R., "The Heat Balance Integral-Further Considerations and Refinements", J. Heat Transfer, Trans. ASME, Series C., 83:83 (1961).
30. Smith, V.G., Tiller, W.A. and Rutter, J.W., "A Mathematical Analysis of Solute Redistribution During Freezing", Canadian J. of Physics, 33:723 (1956).
31. Rutter, J.W. and Chalmers, B., "Solute Redistribution during Planar Solidification", Canadian J. of Physics 31, 15, (1953).
32. Tiller, W.A., Rutter, J.W., Jackson, K.A. and Chalmers, B., "The Redistribution of Solute Atoms During the Solidification of Metals", Acta Met 1:428 (1953).
33. Mullins, W.W. and Sekerka, R.F., "Stability of a Planar Interface During Solidification of a Dilute Binary Alloy", JAP 35:126 (1963).
34. Sekerka, R.F., "A Stability Function for Explicit Evaluation of the Mullins-Sekerka Interface Stability Criterion", JAP 36:461 (1965).
35. Chambre, P.L., "Planar, Cylindrical and Spherical Particle Growth and Stability", Quart. J. Mech. and Appl. Math. IX-2:224 (1956).
36. Bolling, G. F. and Tiller, W. A., "Growth from the Melt. III Dendritic Growth", JAP 32:2587 (1961).
37. Kirkaldy, J.S., "Growth of Needle-Shaped Dendrites", Canadian J. of Physics, 37:739 (1959).
38. Zener, C., "An Analysis of Dendritic Solidification", Trans. Am. Inst. Mining, Met. Petrol. Engrs., 167:550 (1946).
39. Temkin, D.E., Soviet Phys.-Doklady 5:609 (1960). (no title available).

REFERENCES (CONTINUED)

40. Billing, E., "Normal Growth of Crystals", Proc. Royal Soc. A229:346 (1955).
41. Ivartsov, G.P., Doklady Akad. Nauk. SSR 58:567 (1947) (no title available); translation, "Growth of Crystals", Consultants Bureau Inc. New York, 1958.
42. Yovanovich, M. M. "Advanced Heat Conduction", Pre-Publication Issue, 1969.
43. Levin, R.L., Cravalho, E.G. and Huggins, C.E., "Effect of Hydration on the Water Content of Human Erythrocytes" Biophysical Journal 16:1411 (1976).
44. Levin, R.L., Cravalho, E.G. and Huggins, C.E. "A Membrane Model Describing the Effect of Temperature on Water Conductivity of Erythrocyte Membranes at Surface Temperatures", Cryobiology 13:415 (1976).
45. Blum, R. L. and Forster, R. E., "The Water Permeability of the Erythrocyte", Biochem. Biophys. Acta 203:410 (1970).
46. Rich, G.T., Sha'afi, R.I., Ronaldez, A., and Solomon, A.K., "Effect of Osmolarity on the Hydraulic Permeability Coefficient of Red Cells", J. Gen Physiology 52:914 (1968).
47. Zwolinski, B.J., Eyring, H. and Reese, C.E., "Diffusion and Membrane Permeability", J. Phys. Chem. 53:1426 (1949).
48. Modell, M., and Reid, R.C., Thermodynamics and Its Applications Prentice-Hall, New Jersey (1974).
49. van-Laar, J. J., "Uber Dampfspannungen von binaren Gemischen", Z Physik. Chem., 72:723 (1910).
50. Rohatgi, P.K., Adams, C.M., "Dendritic Solidification of Aluminum-Copper Alloys", Trans. Met. Soc. AIME 239:1967 (1967).

BIOGRAPHICAL SKETCH

Michael Gregory O'Callaghan was born on November 30, 1951 in West Palm Beach, Florida. He received his undergraduate education at Rensselaer Polytechnic Institute and his SM degree from MIT. His Master's Thesis was entitled, "An Apparatus for the Cryogenic Preservation of the Isolated Perfused Rat Heart".

The author has been a member of the Cryogenic Engineering Laboratory while at MIT, and has held fellowships from the National Institute of General Medical Sciences, and the Whitaker Health Sciences Fund. He was also the Departmental Instructor for the 1976-7 academic year.

The authors publications include

- 1) O'Callaghan, M. G., Cravalho, E.G., and Huggins, C.E., "An Apparatus for the Cryogenic Preservation of the Isolated Perfused Rat Heart", Cryobiology 12, 587, 1975 (abstract).
- 2) O'Callaghan, M. G., Cravalho, E. G., and Huggins, C. E., "A Planar Interface Model of the Freezing of Biomaterials," Cryobiology 13, 664, 1976 (abstract).
- 3) O'Callaghan, M. G., Cravalho, E. G., and Huggins, C. E., "An Organ Cryopreservation Apparatus," IEEE Transactions on Biomedical Engineering, vol. BME-24, no. 4, 1977, pp. 111-115.
- 4) O'Callaghan, M. G., Cravalho, E. G., and Huggins, C.E., "An Analysis of the Heat and Mass Transport During the Freezing of Biomaterials", Presented at the Fifteenth Annual Meeting of the Society for Cryo-

biology, Tokyo, Japan, August 5-10, 1978.

- 5) O'Callaghan, M. G., Cravalho, E. G., and Huggins, C. E., "Instability of the Planar Interface During the Freezing of Biomaterials," Presented at the Fifteenth Annual Meeting of the Society for Cryobiology, Tokyo, Japan, August 5-10, 1978.